

Università degli studi di Napoli "Federico II"  
Facoltà di Scienze MM FF NN  
Dipartimento di Scienze Fisiche

Corso di Dottorato di Ricerca in Fisica Fondamentale ed  
Applicata XIX ciclo



*Tesi di Dottorato*

***In vivo* HematoPorphyrin mediated  
Fluorescence Reflectance Imaging:  
early tumor detection on small animals**

Candidata

*Dott. <sup>essa</sup> Maddalena Autiero*

*Tutore*

*Chiar.mo Prof. Giuseppe Roberti*

*Coordinatore*

*Chiar.mo Prof. Gennaro Miele*

Anno Accademico 2005/2006

University of studies of Naples "Federico II"  
Sciences MM FF NN Faculty  
Physical Sciences Department

Philosophiae Doctor Course in Fundamental and Applied Physics  
XIX cycle



*PhD Thesis*

***In vivo* HematoPorphyrin mediated  
Fluorescence Reflectance Imaging:  
early tumor detection on small animals**

presented by  
***Maddalena Autiero***

*Supervisor*

***Prof. Giuseppe Roberti***

*PhD Course Coordinator*

***Prof. Gennaro Miele***

## Table of contents

Acknowledgements .....	5
<b>Introduction.....</b>	<b>9</b>
<b>Chapter 1.....</b>	<b>12</b>
<b>Interaction radiation - biological tissues.....</b>	<b>12</b>
1.1 Introduction.....	12
1.2 Property of light .....	12
1.2.1 Energy levels in molecules .....	12
1.2.2 Transitions between levels.....	14
1.3 Fundamentals of tissue optics.....	16
1.3.1 Absorption .....	17
1.3.2 Absorption coefficient.....	18
1.3.3 Absorption in biological tissues .....	19
1.3.4 Scattering.....	23
1.3.5 Scattering coefficient.....	25
1.3.6 Phase function and anisotropy parameter .....	27
1.3.7 Reduced scattering coefficient.....	29
1.3.8 Scattering in biological tissues.....	30
1.4 Conclusions .....	33
<b>Chapter 2.....</b>	<b>34</b>
<b>Planar Fluorescence Imaging.....</b>	<b>34</b>
2.1 Introduction.....	34
2.2 Biomolecules fluorescence .....	34
2.2.1 A brief history .....	34
2.2.2 Fluorescence.....	35
2.2.3 Biomolecules fluorescence features.....	36
2.2.4 Autofluorescence .....	38
2.3 Optical imaging in vivo on small animals.....	40
2.4 Fluorescence Reflectance Imaging: FRI.....	41
2.4.1 Technology .....	41
2.4.2 Targeting strategies.....	43
2.4.2.a Non specific fluorochromes.....	45
2.4.2.b Targeted fluorochromes.....	48

2.4.2.c	Activatable fluorochromes .....	52
2.4.2.d	Fluorescent protein .....	56
2.4.2.e	Bioluminescence.....	58
2.4.3	Advantages and drawbacks .....	60
2.5	Conclusions .....	61
<b>Chapter 3.....</b>		<b>62</b>
<b><i>HP-FRI in vivo on small animals: preliminary measurements.....</i></b>		<b>62</b>
3.1	Introduction.....	62
3.2	Experimental set-up. ....	62
3.3	Materials and methods.....	65
3.4	Results and their discussion.....	67
a.	Preliminary tests .....	67
b.	HP_FRI in vivo.....	72
c.	Combined imaging .....	75
3.5	Conclusions .....	78
3.6	Appendix: an overview on CCD technology(27) .....	79
<b>Chapter 4.....</b>		<b>97</b>
<b><i>HP-FRI in vivo on small animals: early tumor detection .....</i></b>		<b>97</b>
4.1	Introduction.....	97
4.2	Experimental set-up .....	97
4.3	Materials and methods.....	99
a.	Spatial resolution measurements .....	99
b.	The new in vivo HP-FRI modality .....	100
c.	Early tumor detection.....	101
4.4	Results and their discussion.....	101
a.	Spatial resolution measurements .....	101
b.	The new in vivo HP-FRI modality .....	102
c.	Early tumor detection.....	106
4.5	Improvements and future project .....	111
4.6	Conclusions .....	112
<b>Conclusions .....</b>		<b>113</b>

### *Acknowledgements*

Many are those whom I must thank for their help and support during the progress of this thesis. You will permit me to thank you all in general, and acknowledge in particular those who played a direct role in this work.

First of all, I would like to thank the supervisor of this thesis, Prof. Giuseppe Roberti, for all I learned from his knowledge and interest in the new technics and advances in the field of biomedical optics. In this context, I also owe special gratitude to my "tutors", Doct. Patrizia Riccio and Doct. Maria Quarto, since their interest and vitality are contagious. In a similar manner, I would like to extend this gratitude to Prof. Paolo Russo for his support: a part of the work presented in this thesis was developed with his collaboration. I also owe special gratitude to the PhD course coordinator, Prof. Gennaro Miele, for his guide during the PhD course studies. I would like to thank Prof. Salvatore Solimeno, since he was who introduced me into research in the last stages of my undergraduate studies.

Above all, my most sincere gratitude to my father, mother, brothers and husband for the support I have always recieved from them. To them I dedicate this thesis.

## *List of papers*

This thesis is based on the following paper and related works:

- I. L. Celentano, P. Laccetti, R. Liuzzi, G. Mettivier, M. C. Montesi, **M. Autiero**, P. Riccio, G. Roberti, P. Russo, Member IEEE, M. Salvatore. "Preliminary tests of a prototype system for optical and radionuclide imaging in small animals", IEEE Transactions on Nuclear Science, 73,5: 1693-1701(2003).
- II. **M. Autiero**, L. Celentano, R. Cozzolino, P. Laccetti, M. Marotta, G. Mettivier, M. C. Montesi, P. Riccio, G. Roberti, P. Russo, Member IEEE. "Experimental study on in vivo Optical and Radionuclide Imaging in Small Animals", IEEE Transactions on Nuclear Science, 52, 1: 205-209 (2005).
- III. **M. Autiero**, L. Celentano, R. Cozzolino, P. Laccetti, M. Marotta, G. Mettivier, M. C. Montesi, P. Riccio, G. Roberti and P. Russo, "Hematoporphyrin Mediated Laser Induced Fluorescence In Vivo Imaging of Tumor in Small Animals", Transaction on Medical Imaging IEEE, submitted.
- IV. **M. Autiero**, L. Celentano, R. Cozzolino, P. Laccetti, M. Marotta, G. Mettivier, M. C. Montesi, M. Quarto, P. Riccio, G. Roberti, P. Russo, "Early Detection of Tumor Masses by In Vivo Hematoporphyrin mediated Fluorescence Imaging", NIM special issue, in press.
- V. P. Russo, **M. Autiero**, L. Celentano, M. Chemeissani, A. S. Curion, R. Cozzolino, P. Frallicciardi, P. Laccetti, A. Lauria, M. Maiorino, M. Marotta, G. Mettivier, M. C. Montesi, P. Riccio, G. Roberti, "MediSPECT: Single Photon Emission Computer Tomography System of Small Field of View Small Animal Imaging Based on CdTe Hybrid Pixel Detector", NIM special issue, in press.
- VI. **M. Autiero**, L. Celentano, P. Laccetti, M. Marotta, G. Mettivier, M. C. Montesi, P. Riccio, G. Roberti, P. Russo, "In vivo Macroscopic HP Fluorescence Reflectance Imaging on Small Animals bearing Surface ARO/NPA Tumor",

Proceeding SPIE-OSA Biomedical Optics Vol. 5859, 58590C, 40-49 (on line Oct. 7, 2005).

- VII. **M. Autiero**, L. Celentano, R. Cozzolino, P. Laccetti, M. Marotta, G. Mettievier, M. C. Montesi, P. Riccio, G. Roberti, P. Russo, "A multimodal system for in vivo tumor imaging in mice" Proceeding SPIE Vol. 6191-53,2006.

**Other related works:**

- Giornate scientifiche del polo delle scienze e delle tecnologie per la vita; 20/21 maggio 2004, Napoli, "Validazione di un sistema multimodale di imaging ottico e di radioimaging per la rivelazione di tumori in piccoli animali", M. Autiero, L. Celentano, R. Cozzolino, P. Laccetti, M. Marotta, G. Mettievier, M. C. Montesi, P. Riccio, G. Roberti, P. Russo; poster session.
- INFMeeting 2004, 8-10 giugno, Genova, Magazzini del cotone, "In vivo tumor imaging in small animals by dual HP mediated fluorescence/radionuclide planar system", M. Autiero, L. Celentano, R. Cozzolino, P. Laccetti, M. Marotta, G. Mettievier, M. C. Montesi, P. Riccio, G. Roberti, P. Russo; poster session.
- MIC 2004, 16-22 ottobre, Roma, Italia, poster session:
  1. "Hematoporphyrin Mediated Laser Induced Fluorescence In Vivo Imaging of Tumor and Organs Structure in Small Animals", M. Autiero, L. Celentano, R. Cozzolino, P. Laccetti, M. Marotta, G. Mettievier, M. C. Montesi, P. Riccio, G. Roberti, P. Russo.
  2. "Toward a Medipix2 Coded Aperture Gamma Microscope", R. Accorsi, M. Autiero, L. Celentano, P. Laccetti, R. D. Lanza, M. Marotta, G. Mettievier, M. C. Montesi, P. Riccio, G. Roberti, P. Russo.
- Giornate scientifiche del polo delle scienze e delle tecnologie per la vita; 26/27 maggio 2005, Napoli, Invited paper: "Rivelazione precoce in vivo di tumori su piccoli animali attraverso l'imaging di fluorescenza mediato da ematoporfirina", M. Autiero, L. Celentano, R. Cozzolino, P. Laccetti, M. Marotta, G. Mettievier, M. C. Montesi, P. Riccio, G. Roberti, P. Russo; poster session and oral presentation.
- ECBO 2005, 12-16 giugno 2005, Neue Messe, Munich, Germany, "In vivo macroscopic HPD fluorescence reflectance imaging on small animals bearing surface ARO/NPA tumor", M. Autiero, L. Celentano, P. Laccetti, M. Marotta, G. Mettievier, M. C. Montesi, P. Riccio, G. Roberti, P. Russo; poster session.
- MMD-Meeting 2005, 22-25/06/2005, Genova, Italia: "Hematoporphyrin mediated Fluorescence Reflectance Imaging in vivo on small animals: tumors and organs structure detection", M. Autiero, L. Celentano, R. Cozzolino, P. Laccetti, M. Marotta, G. Mettievier, M. C. Montesi, P. Riccio, G. Roberti, P. Russo; poster session.
- Photonics Europe 2006, 3-7 aprile 2006, Palais de la Musique et des Congrès Strasbourg, France, "A multimodal system for in vivo tumor imaging in mice", M. Autiero, L. Celentano, R. Cozzolino, P. Laccetti, M. Marotta, G. Mettievier, M. C. Montesi, P. Riccio, G. Roberti, P. Russo; poster session.
- EuroMedIm 2006, 9-12 maggio 2006, Palais du Pharo, Marseille, France, "Early Detection of Tumor Masses by In Vivo Hematoporphyrin mediated Fluorescence Imaging", M. Autiero, L. Celentano, R. Cozzolino, P. Laccetti, M.

Marotta, G. Mettivier, M. C. Montesi, , P. Riccio, G. Roberti, P. Russo; poster session.

- EuroMedIm 2006, 9-12 maggio 2006, Palais du Pharo, Marseille, France, "MediSPECT: Single Photon Emission Computer Tomography System of Small Field of View Small Animal Imaging Based on CdTe Hybrid Pixel Detector", P. Russo, M. Autiero, L. Celentano, M. Chemeissani, A. S. Curion, R. Cozzolino, P. Frallicciardi, P. Laccetti, A. Lauria, M. Maiorino, M. Marotta, G. Mettivier, M. C. Montesi, P. Riccio, G. Roberti; poster session and oral presentation.
- Giornate scientifiche del polo delle scienze e delle tecnologie per la vita; 15-16 giugno 2006, Napoli, "Sistema multimodale di imaging per la diagnostica tumorale in vivo su piccoli animali", M. Autiero, L. Celentano, R. Cozzolino, P. Laccetti, M. Marotta, G. Mettivier, M. C. Montesi, P. Riccio, G. Roberti, P. Russo; poster session.

## *Introduction*

The present work is included in the research field of the optical biomedical imaging on small animals that, in the last years, has reached a prodigious growth due to various factors of different kind. We will remember, on the one hand, the quick and easy implementation of the optical techniques supported by the technological development of the instrumentation, with the availability of highly sensitive PC controlled sensors (typically CCD camera), in parallel with the development of sophisticated software for the images acquisition and analysis. On the other hand, the genetic and biomolecular revolution has allowed approaching the biological phenomena by a completely new point of view: let think to the sequencing of the human genoma, and then of the mouse genoma, in combination with animal models of human diseases, as a link between in vitro and clinical studies. Finally, the birth of the combinatorial chemistry has produced a large amount of molecules that can interact with a particular biological target of interest. The integration of these factors has been fostered by the erosion of traditional boundaries that separated the different scientific fields and by the consequent establishment of interdisciplinary teams and programmes, where are involved physicians, pathologists, histologists, physicists, chemists, biologists, engineers, mathematicians, etc, each bearing its own competences, but working in synergy.

The imaging process allows a spatial and/or temporal distribution of a physical quantity be registered in an image. In the optical imaging the image acquired by a detector visualizes the spatial distribution of the radiation intensity emitted by an (eventually irradiated) object. Particular success has obtained in the last years the application of the fluorescence reflectance imaging (FRI) technique in biomedical in vivo imaging on small animals. It is a very simple technique where a CCD camera, with entrance filtered to the fluorescence emission wavelength, collects the spatial distribution of the fluorescence radiation emitted by the object irradiated by light at the fluorescence excitation wavelength. What is the object? As it was specified above, it is a small animal, typically a mouse of 20 g body weight, where the biomolecular or genetic target of interest has been labeled with a fluorescent marker. Depending on the biomedical target of interest, the more suitable fluorescence targeting strategy will be selected by using a non specific, specific, or targeted, or “smart” fluorescent contrast agent, called also fluorochrome, or fluorescent or bioluminescent protein.

The scope of imaging studies can be of various kind: the understanding the biomolecular mechanisms that control the functions of the healthy and diseased cells and tissues; or the (possibly) early, diagnosis of oncologic (and some non tumoral) diseases, the subsequent analysis of the disease evolution up to the identification of metastases formation and dissemination; or efficacy tests of new anticancer drug, by monitoring the possible disease regression and/or drug side effects.

Different reasons justify the choice of the optical modality of imaging: optics is a branch of the physics that developed technologically advanced imaging instrumentation and techniques, that are much safer than other imaging modalities, as, for example, radionuclide imaging. Indeed, the optical markers are generally non toxic and the optical radiation, being non-ionizing, doesn't damage the biological tissues, so that the optical methods are intrinsically non invasive. Finally imaging optical systems can be designed having: i) high sensitivity, so allowing for the use of very low dose of fluorescent marker;. ii) high spatial resolution, so they are suitable for the human disease model studies on

small animals; iii) structural features, allowing the integration with other imaging systems to form a multimodal system, where one technique is complementary to the other.

As a counterbalance, optical imaging has intrinsic drawbacks that prevent from its clinical use. Indeed the interaction optical radiation-tissue is characterized by the absorption and the strong scattering by tissues with the consequent loss of the information carried by the light. The penetration depth of the light in the tissues depends on the wavelength and on the irradiation geometry, besides on tissues optical properties and it has a maximum (<10 cm) in the so called optical window, the spectral interval between the 600 nm and 900 nm, where the absorption and the scattering effects are strongly reduced. Here also the fluorescence of biological tissue components, called autofluorescence or endogenous fluorescence has a minimum. This limit in the penetration depth affects optical planar imaging and it can be exceeded only by the tomographic imaging techniques that however we don't discuss in this thesis. Moreover, in the fluorescence imaging, the detected signal is a diffuse light signal whose intensity shows a strong dependence on the depth of the investigated target in the tissue, so the quantitative determinations are difficult to infer. It is also noteworthy to remark that, since any exogenous fluorochrome doesn't have a 100% affinity with the target, some quantity of fluorochrome will be present also in the non-target tissue generating the so called background fluorescence. The autofluorescence and fluorescence background signals lower the optical contrast of the fluorescence labelled target with respect to the surrounding region. Hence, some instrumental and/or data processing procedures are required to cancel these contributions and to improve the optical contrast.

This thesis is an experimental study on the *in vivo* detection of subcutaneous human tumors implanted on small animals by a laser induced FRI technique using a hematoporphyrin (HP) compound as an exogenous optical contrast agent. It is widely reported in literature that the HP compounds accumulate preferentially in tumor tissues, although the uptake mechanisms of HP compounds in tumors are not completely understood. The absence of specificity in the targeting is a limit of HP labeling with respect to other fluorescent tumor markers with high specificity, since doesn't allow for the monitoring of the molecular and/or genetic pathways of the disease. On the other hand, the HP tumor unspecific uptake is an advantage, since it makes HP suitable to target efficiently different type of tumors to the diagnostic purposes. In particular, the early diagnosis is a basic medical requirement to increase the patient survival probability, especially if the tumor has a high degree of malignancy. Indeed, the final aim of our investigation is to test the capability of our HP-FRI system to detect tumor in the early stage of its growth.

In the first chapter the principal features of the interaction of the optical radiation with biological tissue, which constitutes the basis to understand the physical background of the FRI technique, is illustrated. In the second chapter an overview of the FRI techniques is presented, so defining the framework where is collocated this work. In the third and fourth chapter the experimental apparatus and procedures are described and the obtained results are discussed. In particular, in the third chapter, we report on the preliminary tests on the HP-FRI system and on the first HP-FRI measurements, concerning the *in vivo* detection in mice of subcutaneous human thyroid carcinomas of different malignancy degree and on the combination of our optical imaging system with a radionuclide imaging system in order to exploit the complementarity of the two different modality imaging. In the fourth chapter, the HP-FRI measurements acquired with a high

sensitivity CCD camera in the spectral region of interest that allowed for *in vivo* early detection in mice of tumors with a high degree of malignancy are described. Finally, the appendix at the end of the Chapter 3 is devoted to the CCD technology and characteristics, since they are relevant for the performed FRI measurements.

# Chapter 1

## *Interaction radiation - biological tissues*

### *1.1 Introduction*

In this first chapter of the thesis will be recalled the fundamentals of tissue optics as theoretical background of our experimental work in optical imaging *in vivo* on small animals. Here we will just run over the definition of the optical parameters that characterize the interaction between the radiation and the biological medium and their feature versus wavelength of the radiation that travels in the tissue. We are not interested to illustrate the models of light propagation in tissue, because this is beyond the scopes of our thesis, although the study of these models constitutes the prerequisite for quantitative determinations in the optical imaging, that are one of the challenge in this research field. We want especially outline that the strong scattering and absorption, features that dominate the interaction light-tissue, determine the limit of optical imaging *in vivo*, as will be well showed in the next chapter.

### *1.2 Property of light*

Let us recall briefly the general properties of light and molecules before the specific tissue-light interactions are described (7).

Light is dualistic in nature. It can be described as an electromagnetic wave or as a package or quantum of energy - a photon. The aspects are equally valid and often one or the other is chosen to describe a specific phenomenon. The electromagnetic spectrum ranges from radio waves through infrared and visible light to X-rays and gamma radiation. The wavelength,  $\lambda$ , or the frequency,  $\nu$ , are used to describe the radiation when the wave nature is considered, and the energy,  $E$ , is used when light is regarded as a stream of photons. These quantities are easily connected by the speed of light,  $c$ , and the Planck constant,  $h$ .

$$E = h \cdot \nu = h \cdot c / \lambda \text{ [ J ]}$$

$$c = \lambda \cdot \nu \text{ [m/s]}$$

In the experiments described in this thesis, light in the visible and near infrared range has been used. In this region, the wavelength,  $\lambda$ , is the most common quantity used to represent the light energy.

The light fluence rate,  $\phi$  (mW/cm<sup>2</sup>), the light energy per second passing through the unit cross section area, is another important parameter.

#### *1.2.1 Energy levels in molecules*

When atoms bond together to form a molecule, the total energy is lower than the sum of energy of the constituents. The description of energy levels becomes more complicated than for atoms, since energy states due to vibration and rotation motion are added to the electronic levels. In Figure 1.1 (7), the schematic picture of electronic levels and the addition of vibration and rotation levels is shown. The electronic levels are determined by the atomic and electronic configurations of the molecule, whereas the vibrational and rotational levels are determined by the three-dimensional positions of its atomic assembly, and the molecule's quantized vibrational/rotational characteristics generated by the movements of the atomic nuclei of the molecules.

The simplest calculation of vibrational energy levels for a diatomic molecule involves the approximation of the potential by a parabola as in a harmonic oscillator. This results in a simple expression of vibration frequency and energy

$$E = (v + 1/2) \hbar \nu$$

with  $\nu = \sqrt{k/\mu}$ , where  $\mu$  is the reduced mass and  $k$  is a force constant. Thus, the vibrational levels are equidistant and there will always be a non-zero lowest vibrational energy.

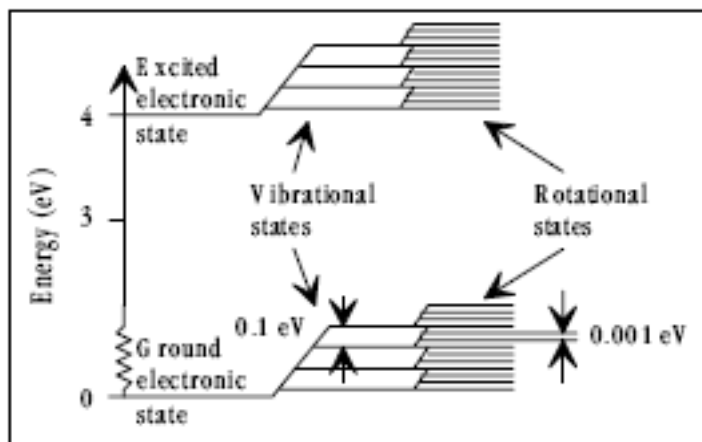


Figure 1.1. Energy states in a molecule.

The degree of complexity increases for polyatomic molecules and there can be numerous modes of vibration. There are two types of vibrational modes: stretching modes, where the distances between the atoms or groups of atoms are altered; and bending modes, where the angles between atoms or groups of atoms are altered.

Molecules in general can rotate around three different axes. For the simple case of a diatomic molecule, it rotates around the mass centre and the rotation energy can be calculated as

$$E = \hbar^2 J(J + 1) / 2I$$

with  $J = 0, 1, 2, \dots$  and  $I$  is the moment of inertia with respect to the rotation axis. If the bond between the atoms is not completely rigid, the molecular bond will be stretched out in higher rotational states and  $I$  will increase, leading to a downshift of higher levels. In polyatomic molecules the theory becomes much more complex, and also here symmetry

aspects are important. In large biomolecules, the rotational structure, in the energy level diagram, is often lost and the energy levels are smeared out into a band.

The configuration of the energy levels of a molecule determines many of the properties of that molecule. For instance, the energy separation between the electronic states determines the visible wavelengths that can be absorbed and thus the colour of the molecule. The transitions between the levels are the origin of many interesting phenomena like laser action, phosphorescence and fluorescence.

The energy separations between close-lying electronic levels often correspond to visible wavelengths. Vibration transitions occur in the infrared range, while transitions between rotational levels in the same vibrational mode fall in the far infrared range.

### 1.2.2 Transitions between levels

Light impinging on a molecule can, if the energy corresponds to the energy separation between two levels, be absorbed and an electron is transferred to a higher level. The excited state of a molecule can be an electronic, a vibrational or a rotational level, where a multitude of vibrational and rotational levels are associated with each electronic level. The molecule only remains in this state for a short period of time given by the lifetime of that state. There are selection rules set by quantum mechanics for radiative transition within vibration and rotational levels. For vibration,  $\Delta v = \pm 1$  must be fulfilled and for rotation  $\Delta J = \pm 1$ . On the way back to the ground state, none or several intermediate levels may be involved.

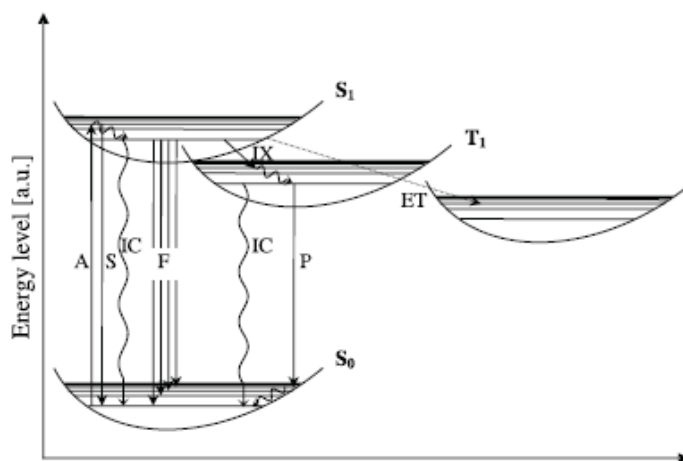


**Figure 1.2:** Jablonski diagram of a fluorescent molecule. Electronic levels are S singlet states, and T triplet states. Vibrational levels are represented by the nonlabeled horizontal bar, contained within the electronic levels. Rotational levels are not shown. A denotes the resonant absorption of a photon, S is the resonant scattering, and IC internal conversion. All “wavy” arrows denote internal conversion. F is fluorescence and P phosphorescence. IX represents intersystem crossing and ET energy transfer to another molecule.

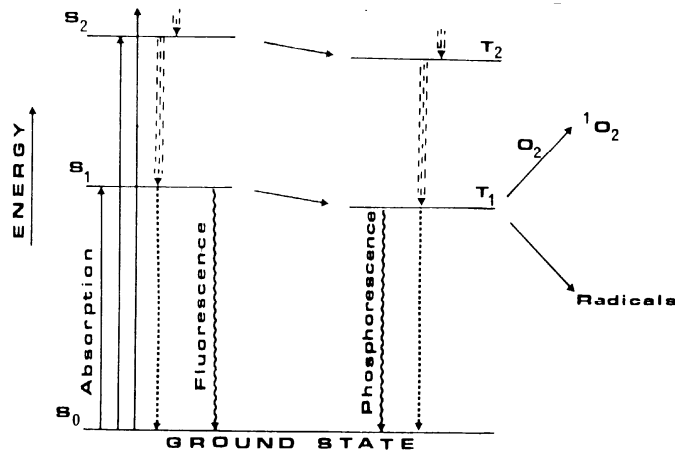


**Figure 1.3.** Schematic of energy transfer from photosensitive substance (hematoporphyrin) to oxygen molecules. The molecule absorbs a photon with a electron jump up excited states empty ( $S_1$  e  $S_2$ ). After about 20 nsec three phenomena can be occur: the first is the radiative decay with fluorescence emission, the second is energy conversion in heat; the third is state change of the electron which modifies only the state spin ( $T_1$  e  $T_2$  triplet states). This later event is statistically dominant and produces other events: radiative decay with phosphorescence emission and energy transfer to oxygen molecules, that so they produce radicals.

On the one hand, elastic resonant radiation can occur, resulting in a photon being emitted at the same wavelength as the incoming one. On the other hand, one of several inelastic scattering processes may ensue. In brief, the molecule can return to its ground state through one of the following pathways (Figure 1.2)<sup>1(7)</sup>:

- **resonant radiation** of identical wavelength, compared to the incoming photon.
- **internal conversion (IC)** Due to interaction with other molecules, the electron is transferred to the lowest lying vibrational and rotational state within the excited state furnishing energy to molecular motion generating heat.
- **intersystem crossing:** Because the transition between a singlet and a triplet state including emission of light is forbidden, if an atom, with a singlet ground state, is in its lowest lying triplet state, it can only release the excess energy due to other interactions, for instance collisions. Such a transition is called inter-system crossing. Thus the triplet state is a metastable state with a long lifetime. In a so-called Jablonski diagram (Figure 1.2), the transition from state  $S_1$  to  $T_1$  is shown. In this state, the molecule can stay for long times since the transition to the ground state  $S_0$  is forbidden. If it returns to the ground state, the emission is called **phosphorescence**.
- **fluorescence**, When the molecule returns to any of the levels in the ground state, fluorescence light can be emitted. The wavelength of the fluorescence will always be longer than the excitation light. Fluorescence light in solids and liquids is broadbanded due to the strong interaction between molecules and due to the large number of vibration and rotation levels which involves the re-emission of a photon of lower energy, i.e. greater wavelength.

<sup>1</sup> Finally, another inelastic process can occur, if the photon excites the molecule to a virtual state, followed by a rapid radiative de-excitation to the molecule's electronic ground state, where a slight shift in the vibrational level of the molecule is possible. Hence, the emitted photon may be of longer, equal or shorter wavelength, referred to as Stokes, Rayleigh and anti-Stokes scattering, respectively. The process itself is denoted Raman scattering.

- **energy transfer** to a neighboring molecules, causing a chemical reaction. A clinically relevant example is the transfer of energy to oxygen, potentially resulting in cytotoxic oxygen species, such as singlet oxygen ( $^1\text{O}_2$ ), which can react with and destroy e.g. lipid bilayer membranes (Figure 1.3).(8) This phenomenon can be utilized in selectively destroying tissue, e.g. neoplastic lesions in a process called photodynamic therapy (PDT). In PDT, a photosensitizing substance is either applied topically, i.v. or i.p. injected or administered orally, followed by illumination of the treatment area, using an appropriate wavelength. The desired result is tumor necrosis.(9)
- **molecular dissociation** after excitation to repulsive states.

In conclusion, the deexcitation modes non-radiative, collision, internal conversion and inter-system crossing, compete with fluorescence emission.

### 1.3 Fundamentals of tissue optics

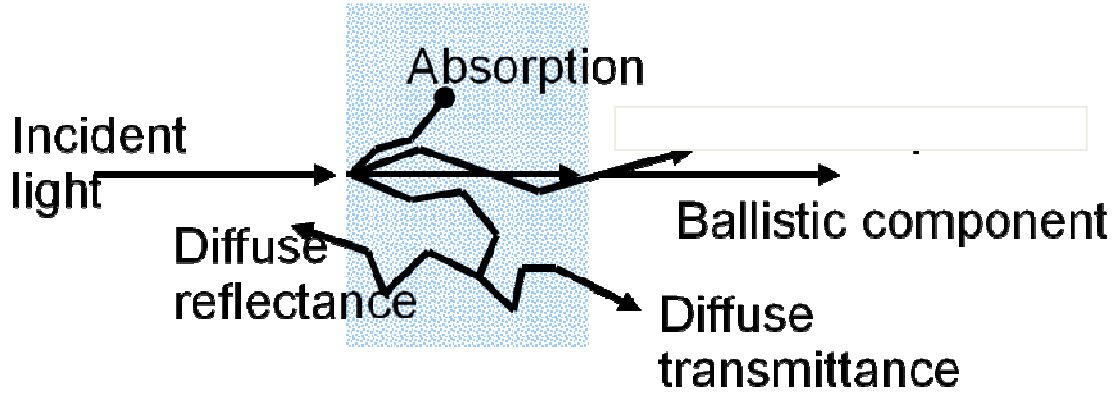
The term tissue optics encompasses modelling of the light transport in tissues, measurement of tissue optical transport parameters, and development of models which can explain the optical properties of tissue and their dependence on the number, size and arrangement of the tissue elements. An exact modelling of the inhomogeneous and turbid tissue is not presently feasible. The tissue is therefore generally represented as an absorbing bulk material with scatterers randomly distributed over the volume. Further, it is usually assumed to be homogenous, even though this is not a true representation. Hence, absorption and scattering are the two physical phenomena affecting light propagation in biological tissue (Figure 1.3). Although both are important, scattering is the dominant mechanism (10). Even for sub-millimetre, sections of tissue, injected photons are likely to be scattered several times before they reach the boundary. As a consequence a coherent, collimated input laser beam will be effectively incoherent and isotropic after traversing a few millimetres of tissue.

Figure 1.3 shows schematically what happens to a light photons beam when they incide on the interface between air and biological medium. If the incidence angle is not normal, a fraction will be reflected (specular reflectance, see Figure 1.9); a remaining fraction will be refracted in the biological medium, where they can be or absorbed by molecules when the light photon energy equals the energy difference between levels of molecular electronic states; or backscattered, after they have expedited multiple scattering events that them report on the interface (diffuse reflectance); or forward scattered remerging on the opposite interface after multiple scattering events that have altered their motion direction (diffuse transmittance); or unaltered transmitted without scattering events on their walk (ballistic component).

Therefore, the parameters used to characterize the optical properties of the tissue are:

- the absorption coefficient  $\mu_a$ ,
- single scattering coefficient  $\mu_s$ ,
- transport coefficient  $\mu_t = \mu_a + \mu_s$
- phase function  $p(\mathbf{e}_s, \mathbf{e}_s')$ , from which derive the anisotropy parameter  $g$  and the reduced scattering coefficient  $\mu_s' = \mu_s(1 - g)$ .

In the next paragraphs we will illustrate in major detail these two fundamentals phenomena in the light propagation in tissue, introduce the corresponding parameters and discuss the principal characteristic of biological tissue components.



**Figure 1.3:** Scattering and absorption of light photon in biological medium. The incident photons reflected or refracted on the interface between air and biological medium; the photons refracted are or absorbed by molecules, or backscattered returning on the interface (diffuse reflectance) or forward scattered remerging on the opposite interface (diffuse transmittance) or unaltered transmitted (ballistic component).

### 1.3.1 Absorption

The condition when the photon energy of the incident radiation field exactly matches the energy difference between the final (excited) and initial state of a molecule is called *resonance*. The photon can be then absorbed by the molecule which changes from the initial state to the excited state through a transition. Hence, the probability of absorption is strongly wavelength dependent. Molecules that absorb light are called chromophores.

There are two major types of transition: electronic transitions and vibrational transitions (5).

The former are relatively energetic and hence are associated with absorption of ultraviolet, visible and near-infrared wavelengths. Many biological molecules can absorb light via electronic transitions. In early biological evolution, the pyrrole molecule was a chromophore which could absorb sunlight which enabled subsequent synthetic reactions that produced biological polymers and other proto-metabolic products. Combining four pyrroles into a tetrapyrrole ring yielded an efficient chromophore for collecting solar photons: porphyrin. Chlorophyll is such a porphyrin. Hemoglobin, vitamin B12, cytochrome C are also examples of porphyrins in biology. We outline that the optical contrast agent used in optical imaging in our work belongs to the porphyrin family, as we will see in the next chapter.

The latter interests the field of infrared spectroscopy that studies the variety of bonds which can resonantly vibrate or twist in response to infrared wavelengths and thereby absorb such photons. Perhaps the most dominant chromophore in biology which absorbs via vibrational transitions is water (Figure 1.4). In the infrared, the absorption of water is the strongest contributor to tissue absorption.

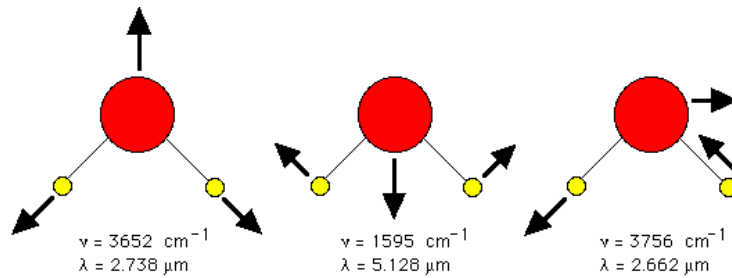


**Figure 1.4:** Schematic of vibrational modes of water molecule and the corresponding frequency and wavelength of the transition.

### 1.3.2 Absorption coefficient

The absorption coefficient is the parameter used to describe the effectiveness of absorption. To intuitively understand the significance of this parameter, we can recur to a schematic, hence incorrect description of the real situation. Idealize a chromophore as a sphere with a particular geometrical size; consider that this sphere, absorbing incident light, blocks and casts a shadow (Figure 1.5). The size of the absorption shadow is called the effective cross-section ( $\sigma_a$  [ $\text{cm}^2$ ]) and can be smaller or larger than the geometrical size of the chromophore ( $A$  [ $\text{cm}^2$ ]), related by the proportionality constant called the absorption efficiency  $Q_a$  [dimensionless]:

$$\sigma_a = Q_a A$$

If a medium containing many chromophores at a concentration described as a volume density  $\rho_a$  [ $\text{cm}^3$ ] is considered, the absorption coefficient  $\mu_a$  [ $\text{cm}^{-1}$ ] is the cross-sectional area per unit volume of medium.

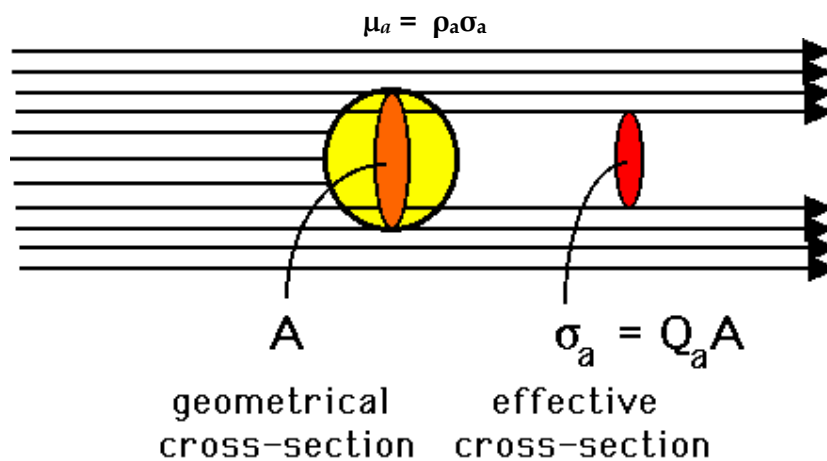


**Figure 1.5:** Schematic description of absorption of light by a chromophore sphere.

Experimentally, the units [ $\text{cm}^{-1}$ ] for  $\mu_a$  are inverse length, such that the product  $\mu_a L$  is dimensionless, where  $L$  [ $\text{cm}$ ] is a photon's pathlength of travel through the medium. So, the absorption coefficient,  $\mu_a$  can be defined as

$$dI = -I dx \mu_a$$

where  $dI$  is the differential change of the intensity  $I$  of a collimated light beam traversing an infinitesimal path  $dx$  through a homogeneous medium with absorption coefficient  $\mu_a$ . Integration over a thickness  $x$  yields

$$I = I_0 e^{-\mu_a x}$$

Expressing the absorption coefficient  $\mu_a$  in terms of particle density  $\rho$  and absorption cross section  $\sigma_a$  we obtain the Beer-Lambert law

$$I = I_0 e^{-\rho \sigma_a x}$$

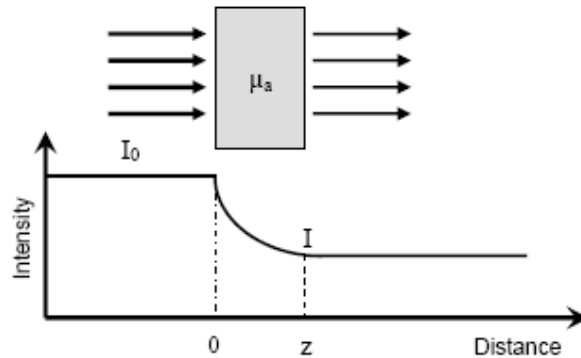


**Figure 1.6.** The Lambert-Beer law of exponential decay of light intensity when travel in tissue of absorption coefficient  $\mu_a$ (11)

The reciprocal,  $1/\mu_a$ , is called the absorption pathlength and equals the mean free path a photon travels between consecutive absorption events. The probability of survival (or transmission  $T$ ) of the photon after a pathlength  $L$  is:

$$T = e^{-\mu_a L}$$

This expression for survival holds true regardless of whether the photon path is a straight line or a highly tortuous path due to multiple scattering in an optically turbid medium. We recall also the definition of the attenuation, or optical density (OD) of an attenuating medium given by

$$OD = \log_{10}(1/T) = -\log_{10}(I/I_0)$$

### 1.3.3 Absorption in biological tissues

In biomedical optics, absorption of photons is a very important event. Without absorption, there is no energy transfer to the tissue. It is the primary event that allows a laser or other light source to cause a potentially therapeutic (or damaging) effect on a

tissue. Absorption is used for both spectroscopic and imaging applications: provides a diagnostic role such as the spectroscopy of a tissue and a clue as to the chemical composition of a tissue, and serve as a mechanism of optical contrast during imaging.

The absorption coefficient of biological tissues is wavelength dependent. However, the overall absorption coefficient of tissue does not display a simple relation to wavelength, since multiple tissue components absorb light, each with a unique wavelength profile. The most important chromophores in human biological tissue are DNA, melanin, water, fat, proteins such as organometallic molecules, e.g. cytochromes, myoglobin, and oxygenated ( $\text{HbO}_2$ ) and deoxygenated hemoglobin (Hb).

Let us analyze in major details the absorption spectrum of water, fat and hemoglobin. The first (12) is shown in Figure 1.7. Significant transmission through tissue is only possible from the UV (about 200 nm) to the near infrared (about 935 nm). The absorption drops again beyond 1000 nm, but there are currently no efficient detectors available at such long wavelengths.

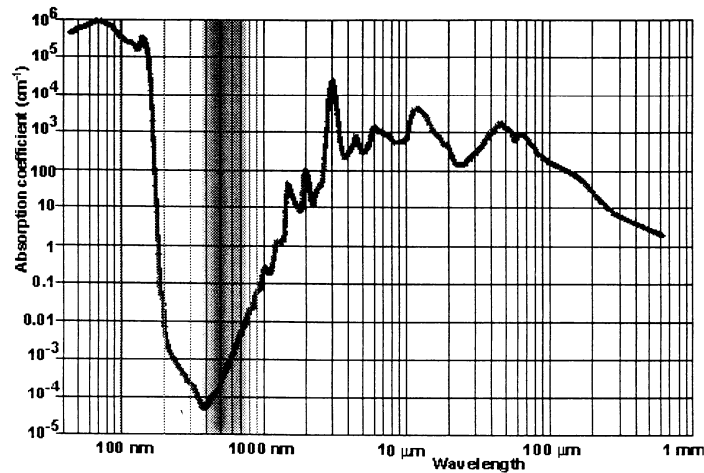
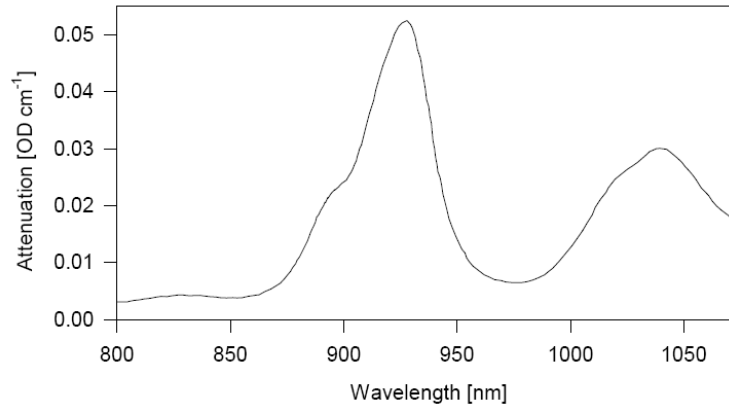


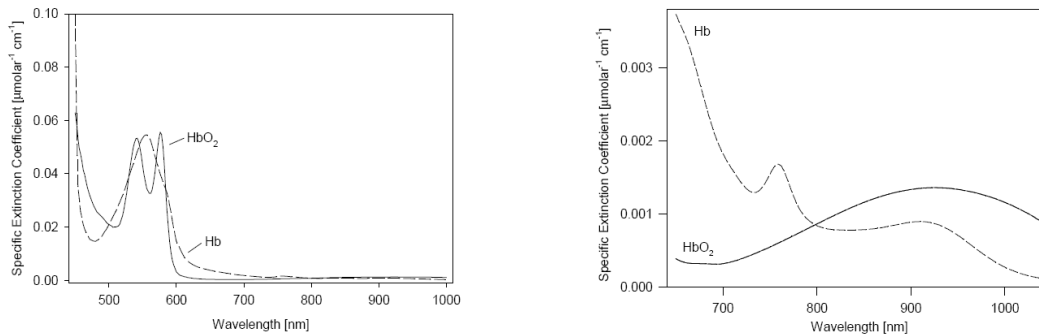
Figure 1.7: Absorption spectrum of water.

Figure 1.8 represents the absorption spectrum of pork fat (13), which is thought to be largely identical to that of human lipids. The absorption coefficient, which is of the same order of magnitude as for water, is low at shorter wavelengths (down to about 600 nm, not shown in spectrum), with a strong peak at about 930 nm.



**Figure 1.8:** Attenuation of pork fat

The spectra of oxy- and deoxyhemoglobin, expressed in terms of the specific extinction coefficient, can be seen in Figure 1.9 (14). Hemoglobin molecules within the red blood cells (Erythrocytes) carry 97% of the oxygen in the blood, while the remaining 3% is dissolved in the plasma. Each hemoglobin molecule consists of four iron-containing heme groups as well as the protein globin. It is the iron to which the oxygen atoms easily bind, causing the hemoglobin molecule to assume a new three-dimensional shape. In the oxygenated state hemoglobin is referred to as oxyhemoglobin ( $\text{HbO}_2$ ), and in the reduced state it is called deoxyhemoglobin (Hb). Oxyhemoglobin has its main absorption peak, the *Soret band*, at 418 nm, and two smaller absorption peaks, *Q bands*, at 542 and 577 nm, respectively. Upon deoxygenation, the Soret band is shifted slightly up in wavelength, whereas the two Q bands of  $\text{HbO}_2$  instead form a single absorption peak at approximately 560 nm for Hb, and a new absorption peak appears at about 758 nm. While both absorb strongly in the blue and green regions of the visible spectrum, the absorption of deoxyhemoglobin is slightly stronger beyond about 690 nm. Hence venous blood appears in a darker red than the arterial blood. The concentrations of oxygenated and deoxygenated hemoglobin change according to the function and metabolism of the tissue. Thus the corresponding changes in absorption can provide clinically useful physiological information.



**Figure 1.9** Absorption spectra of oxy- and deoxyhaemoglobin in the ranges 450-1000 nm (left), and 650-1050 nm (right)

The Figure 1.10 summarize the primary absorption spectra of biological tissues. Also shown are the absorption coefficients at some typical laser wavelengths.

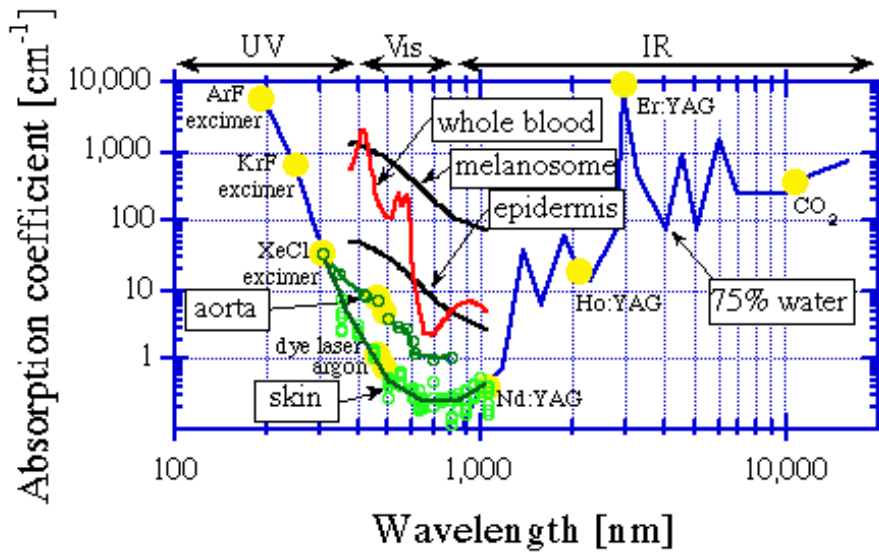


**Figure 1.10:** Absorption spectra of biological tissues. Also shown are the absorption coefficients at some typical laser wavelengths.

In the ultraviolet (UV) spectral region ( $\lambda < 400\text{ nm}$ ), the main chromophores responsible for light absorption are DNA, proteins and water. Because of the high tissue concentration of these molecules, light absorption is strong. The key absorbers are the organometallic molecules, as well as epidermal melanin, bilirubin, hemosiderin and carotenes in fatty tissue (15,16). A ten per cent volume fraction of melanosomes are assumed in the epidermis, and a five per cent volume fraction of blood in the dermis (45 % hematocrit). The water content is set to 75 % (17). The key features to observe are the decrease in melanin absorption and increase in water absorption with increasing wavelength. Tissue absorption continues to decrease up to about 1300 nm in the near infrared (NIR) region (700-2500 nm), and then it rapidly increases again, mainly as a result of light absorption by water. The main constituents of biological tissue which contribute towards absorption in the near infrared are water, fat and hemoglobin. The wavelength region 650-900 nm is called the tissue optical window, since the absorption generally is lower, and, hence, light penetration will be deeper.

It is not only the chemical composition of the different chromophores that determine tissue absorption, but also their concentrations and chemical structural configuration (18). Water is the overall dominant absorber in tissue, because, although the absorption coefficient of water is rather low in this 'water transmission window', its concentration is very high in biological tissue, a fact easily understood since cells can consist of up to 85 % water.<sup>43</sup> Blood is the main absorber in the visible spectrum, but its dominance is reduced by the fact that the tissue volume fraction of blood only is about two to five per cent.<sup>40</sup> Further, in highly absorbing chromophores, such as blood in the UV to green/yellow region, a phenomenon called shielding can be observed. Since blood is contained in vessels, only the outermost chromophores are apparent to the light. The central core of absorbers is, in effect, shielded by the surrounding blood. Thus, a homogenous distribution of blood of a certain hematocrit will result in a greater effective

light absorption, in the UV to green/yellow spectral region, compared to the case when blood is enclosed in vessels (19). The difference is negligible if the absorption length in blood ( $[\mu_{a,\text{blood}}]^{-1}$ ) is large compared to the individual blood vessel radius (19), which is more likely to be the case in the red wavelength region, where the light absorption by blood is a factor 100 smaller compared to at green/yellow wavelengths, and 1000 times smaller than in the UV range. Finally, changes in the molecular configuration of a chromophore also have an impact on the absorption coefficient (16). These configurational alterations can be induced by temperature and tissue osmotic changes, as well as oxygenation of a molecule, which is apparent in the case of hemoglobin.

### 1.3.4 Scattering

Scattering of light occurs in media which contains fluctuations in the refractive index  $n$ , whether such fluctuations are discrete particles or more continuous variations in  $n$ . Refractive index mismatches on a macroscopic scale, e.g. between skin and skull, give rise to refraction, but are usually so small that they are ignored in most photon transport models. The refractive index varies very little on a macroscopic scale and is typically around 1.40 for most tissue types (20). The refractive indices of the individual tissue constituents vary from 1.33 for water to approximately 1.55 for fat and concentrated protein solution (21). However, scattering of light in biological tissue is caused by refractive index mismatches at microscopic boundaries such as cell membranes, organelles, cell nuclei etc. So, the scattering properties of tissue are related to its morphology. Probably, the most appropriate model is to describe a biological scattering medium as a continuum of refractive index fluctuations. The main drawback of this approach, is its mathematical complexity (15). For this reason, a scattering medium is instead often perceived as an ensemble of discrete, randomly distributed scattering particles with a refractive index different from that of the surrounding medium. Light scattering can occur by non resonant elastic scattering or quasi-elastic scattering. Non resonant elastic scattering (Rayleigh scattering) is weak, and is the result of a photon coming within interaction distance of an atom (or a molecule) in its ground state, where the energy of the incoming photon does not correspond to any of the atom's stable energy levels. The electromagnetic field of the incoming photon may still drive the electron cloud of the atom into oscillation, but there is no resulting atomic transition. In effect, an oscillating dipole has been created by the vibration of the electron cloud with respect to the positive nucleus, thus emitting light at the same frequency as the incoming photon (22). After a minimal time delay, about 10-15 seconds, the photon may have changed its direction of motion, and polarization, but still has the same energy, i.e. frequency, and the atom or molecule remains in its ground state. Quasi-elastic scattering involves a minute frequency shift of the incoming light, as a result of interaction with a moving scatterer.

The elastic scattering process can be further subdivided, based on if the photon is refracted/reflected at a boundary between media with different refractive indices, or if it interacts with an object. In the former process, the scattering behavior is determined by the angle between the incident light and a normal to the boundary/surface, the magnitude of the refractive index mismatch, the polarization of the light, and the structure and shape of the surface. Snell's law describes the angle of the refracted light at a boundary:

$$n_1 \sin \vartheta_1 = n_2 \sin \vartheta_2$$

where  $n_1$  and  $n_2$  are the refractive indices of the two respective media, and  $\vartheta_1$  and  $\vartheta_2$  are the angles between a normal to the boundary and the incident and transmitted light, respectively. The fraction of reflected power, or specular reflectance,  $R$ , at a boundary, is given by Fresnel's law, (Figure 1.11) assuming unpolarized light (15):

$$R = \frac{1}{2} \left[ \frac{\sin^2(\vartheta_1 - \vartheta_2)}{\sin^2(\vartheta_1 + \vartheta_2)} + \frac{\tan^2(\vartheta_1 - \vartheta_2)}{\tan^2(\vartheta_1 + \vartheta_2)} \right]$$

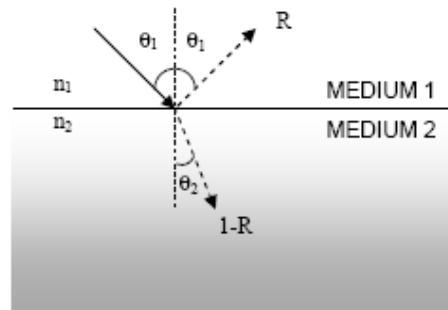


**Figure 1.11:** A ray of light hitting an interface between two media with different refractive index is partially reflected into the new medium.  $\vartheta_1$  is the angle between the incoming or reflected light beam, and a normal to the interface, while  $\vartheta_2$  is the angle between the refracted ray and a normal to the interface.  $R$  is the fraction of reflected power, assuming unpolarized light.

In the latter process, Mie theory rigorously describes the scattering behavior of spherical particles as a function of the parameters  $x$  and  $m$ , where

$$x = 2\pi\alpha/\lambda$$

$$m = n_s/n_m$$

$x$  is a dimensionless size parameter,  $\alpha$  is the radius of the spheres and  $\lambda$  is the wavelength of the radiation outside the sphere (23).  $m$  is the relative refractive index, defined as the ratio of the refractive index of the sphere,  $n_s$ , and the surrounding medium,  $n_m$ ; thus, in a sense, coupling Mie theory to specular reflectance.

It has been shown by Graaf et al (24) that the scattering efficiency is proportional to  $\lambda^{-0.37}$ , for  $1 < m < 1.1$  and  $5 < x < 50$ , where the range of  $m$  probably is relevant for human tissue, based on measurements of the refractive index of various tissue types (20). The highly anisotropic (i.e. not equal in all directions) character of light scattering in most tissue types (25) indicates that the range of  $x$  is relevant as well. However,  $x$  appears to be smaller in e.g. adipose tissue,16 which displays a more isotropic light scattering (25). The aforementioned range,  $5 < x < 50$ , would roughly correspond to  $0.8\lambda < \alpha < 8\lambda$ , or  $0.5 \mu\text{m} < \alpha < 5 \mu\text{m}$  at  $\lambda = 632.8 \text{ nm}$ , the wavelength of the commonly used helium-neon (He-Ne) laser.

The probability of Mie scattering is dependent on the size of the particle,  $r$ , that the incoming photon interacts with, and on the wavelength of the incoming photon,  $\lambda$ . In the case of a sphere,  $r$  corresponds to its diameter, i.e.  $2\alpha$ . If  $r \sim \lambda$ , or  $r > \lambda$ , the probability of

scattering is approximately proportional to  $\lambda^{-0.37}$ , as previously mentioned (24). The distribution of the scattered photons is highly forward peaked. On the other hand, if  $r \ll \lambda$ , the probability of this elastic scattering process is proportional to  $\lambda^{-4}$ , i.e. it is highly wavelength dependent (26). This special case is denoted Mie scattering in the Rayleigh limit, or, simply, Rayleigh scattering, which yields a nearly isotropic distribution of the scattered photons. In between these two extremes, there is a general trend that the wavelength dependence of the scattering probability changes from  $\lambda^{-4}$  to  $\lambda^{-0.37}$ , as the particle size,  $\alpha$ , increases from  $r \ll \lambda$  to  $r > \lambda$  (Figure 1.12).

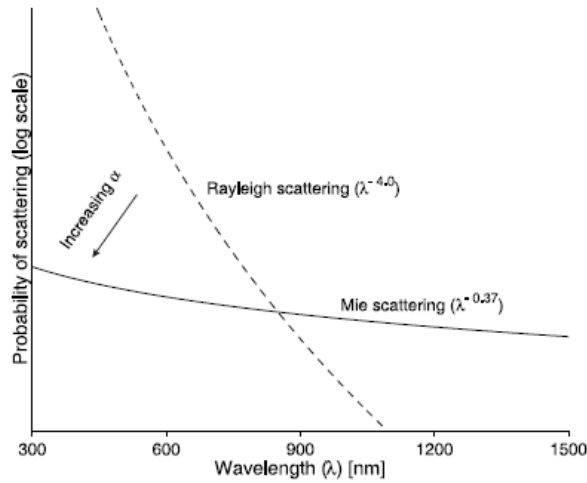


**Figure 1.12:** Wavelength dependence of light scattering in spherical particles. Note that the scattering probability is monotonously decreasing with increasing wavelength of the light. Increasing radius of the light scattering elements,  $\alpha$ , reduces the wavelength dependence of scattering, progressing from a  $\lambda^{-4.0}$  to a  $\lambda^{-0.37}$  relationship.

### 1.3.5 Scattering coefficient

Following an analogous schematics used to introduce the absorption coefficient, consider a scattering particle idealized as a sphere with a particular geometrical size. Assume that scattering is constituted by the process in which this sphere redirects incident photons into new directions, so preventing the forward on-axis transmission of photons and thereby casting a shadow (Figure 1.13). Again, this description, an oversimplified and schematicized version of the real situation, provides a simple concept which captures the essence of the scattering coefficient, a parameter analogous to the absorption coefficient discussed previously.

The size of the scattering shadow is called the effective cross-section ( $\sigma_s$  [ $\text{cm}^2$ ]) and can be smaller or larger than the geometrical size of the scattering particle ( $A$  [ $\text{cm}^2$ ]), related by the proportionality constant called the scattering efficiency  $Q_s$  [dimensionless]:

$$\sigma_s = Q_s A$$

For a medium containing many scattering particles at a concentration described as a volume density  $\rho_s$  [cm<sup>3</sup>], the scattering coefficient  $\mu_s$  [cm<sup>-1</sup>] is the cross-sectional area per unit volume of medium:

$$\mu_s = \rho_s \sigma_s$$

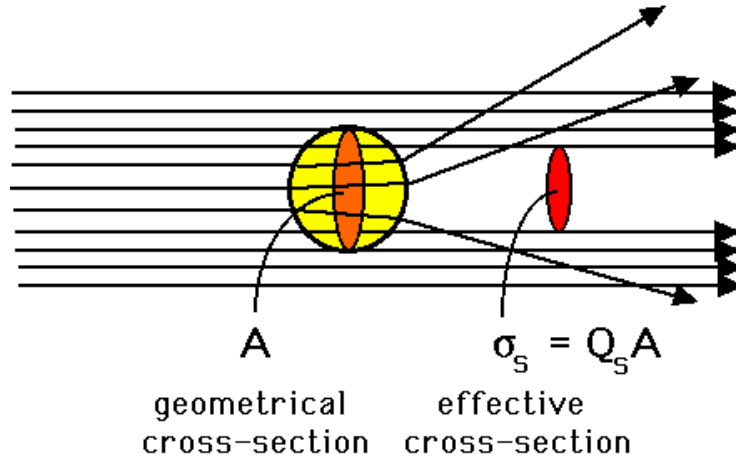


Figure 1.13: Schematic description of scattering of light by a sphere.

Experimentally, the units [cm<sup>-1</sup>] for  $\mu_s$  are inverse length, such that the product  $\mu_s L$  is dimensionless, where  $L$  [cm] is a photon's pathlength of travel through the medium. In the same manner as for absorption, one can define a scattering coefficient,  $\mu_s$ , for a collimated source, such that

$$I = I_0 e^{-\mu_s x}$$

where  $I$  is the non-scattered component of light after traversing a non-absorbing sample of thickness  $x$ .

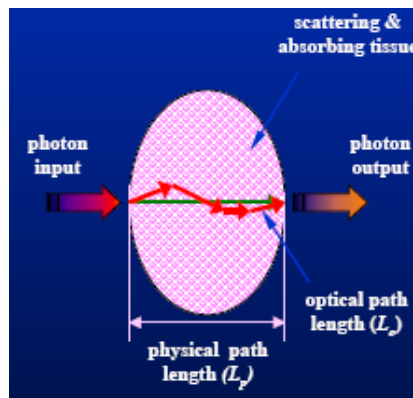


Figure 1.14: The optical path length, the path length done by light photon in traveling the tissue, is different by the physical path length, the thickness of the medium traveled, because of scattering or absorption events in the medium.

The probability of transmission  $T$  of the photon without redirection by scattering after a pathlength  $L$  is:

$$T = e^{-\mu_s L}$$

The scattering pathlength,  $1/\mu_s$ , is the average distance a photon travels between consecutive scattering events and the quantity  $\mu_s x$  is the (dimensionless) optical thickness of a sample expressed in terms of scattering pathlengths (Figure 1.14).

### 1.3.6 Phase function and anisotropy parameter

When a photon that is incident along a direction described by the unit vector  $\mathbf{e}_s$  experiences a scattering event, the angular probability of it being scattered into direction  $\mathbf{e}_s'$  is given by the normalised phase function  $p(\mathbf{e}_s, \mathbf{e}_s')$ . For random, soft tissues it can be assumed that the probability distribution is a function of the angle between the incident and scattered photon only, and does not depend on the angle of incidence relative to the scatterer. Hence the phase function can be conveniently expressed as a function of the cosine of the scattering angle  $\mathbf{e}_s \cdot \mathbf{e}_s' = \cos(\theta)$

$$p(\mathbf{e}_s, \mathbf{e}_s') = p(\cos\theta)$$

Consider an experiment in which a laser beam strikes a target such as a cylindrical cuvette containing a dilute solution of scattering particles. The scattering pattern  $p(\theta)$  is measured by a detector that is moved in a circle around the target while always facing the target. Hence the detector collects light scattered at various deflection angles  $\theta$  in a horizontal plane parallel to the table top on which the apparatus sits. The anisotropy,  $g$  [dimensionless], is a measure of the amount of forward direction retained after a single scattering event. Imagine that a photon is scattered by a particle so that its trajectory is deflected by a deflection angle  $\theta$ , as shown in the Figure 1.15. Then the component of the new trajectory which is aligned in the forward direction is shown in red as  $\cos(\theta)$ . On average, there is an average deflection angle and the mean value of  $\cos(\theta)$  is defined as the anisotropy. The proper definition of anisotropy is the expectation value for  $\cos(\theta)$ :

$$g = \int_0^\pi p(\theta) \cos\theta \, 2\pi \sin\theta \, d\theta = \langle \cos\theta \rangle, \text{ where } \int_0^\pi p(\theta) \, 2\pi \sin\theta \, d\theta = 1$$

It is common to express the definition of anisotropy in an equivalent way:

$$g = \int_{-1}^1 p(\cos\theta) \cos\theta \, d(\cos\theta), \text{ where } \int_{-1}^1 p(\cos\theta) \, d(\cos\theta) = 1$$

Note that the function depends on only the deflection angle  $\theta$  and not on the azimuthal angle  $\psi$ . Such azimuthally symmetric scattering is a special case, but is usually adopted when discussing scattering. However, it is possible to consider scattering which does not exhibit azimuthal symmetry. The  $p(\theta)$  has historically been also called the scattering phase function. A theory developed by (27) enables analytical solutions of the

phase function to be derived for the scattering of a plane electromagnetic wave by isotropic spherical particles of any size. Note that in the limit where the size of the scatterer is much less than the wavelength of the incident photon, Mie theory can be approximated by Rayleigh's theory of scattering (28). This, however, is of limited significance for scattering in biological tissues. The limiting cases are  $g=0$  for perfectly isotropic scattering, and  $g=1$  for complete forward scattering of the incident wave. Biological tissues in the NIR wavelength range are strongly forward scattering with anisotropy factors typically in the range  $0.69 < g < 0.99$  (10).

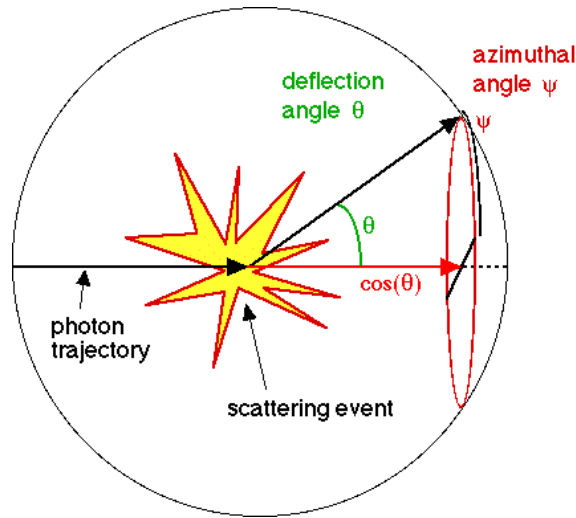


**Figure 1.15:** A scattering event causes a deflection at angle  $\theta$  from the original forward trajectory. There is also an azimuthal angle of scattering,  $\psi$ . But it is the deflection angle  $\theta$  which affects the amount of forward direction,  $\cos(\theta)$ , retained by the photon.

In terms of phase function, the scattering can be described in two ways (Figure 1.16): plotting  $p(\theta)$  or  $p(\theta)2\pi\sin\theta$ . In the first case, the plot indicates how photons will scatter as a function of  $\theta$  in a single plane of observation (source-scatterer-observer plane). This pattern is similar to the type of goniometric scattering experiments commonly conducted. In the second case, the plot indicates how photons will scatter as a function of the deflection angle  $\theta$  regardless of the azimuthal angle  $\psi$ , in other words integrating over all possible  $\psi$  in an azimuthal ring of width  $d\theta$  and perimeter  $2\pi\sin\theta$  at some given  $\theta$ . The  $p(\theta)2\pi\sin\theta$  goes to zero at  $0^\circ$  because the azimuthal ring becomes vanishingly small at  $0^\circ$ . This plot is related to the total energy scattered at a given deflection angle and hence is more pertinent to the value of anisotropy.

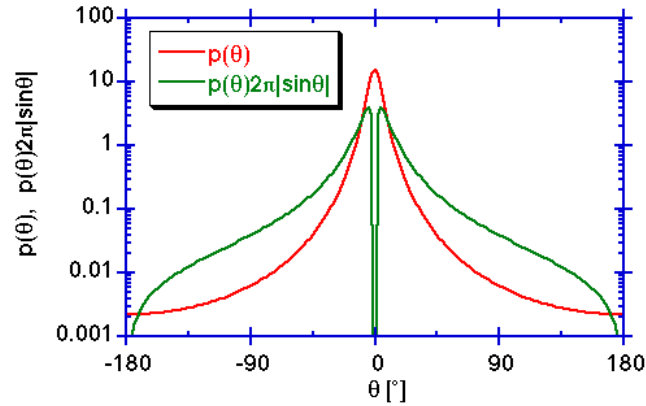


**Figure 1.16:** a typical forward-directed scattering pattern  $p(\theta)$  corresponding to an experimental goniometric measurement in a single source-scatterer-observer plane, and  $p(\theta)2\pi|\sin\theta|$  which integrates over all possible azimuthal angles  $\psi$ .

An isotropic scattering function would scatter light with equal efficiency into all possible directions. Such a scattering function would have the form:

$$p(\theta) = \frac{1}{4\pi} \quad , \quad \text{such that} \quad \int_0^\pi p(\theta) 2\pi \sin\theta \, d\theta = 1$$

### 1.3.7 Reduced scattering coefficient

The reduced scattering coefficient is a lumped property incorporating the scattering coefficient  $\mu_s$  and the anisotropy  $g$ :

$$\mu_s' = \mu_s(1 - g) \text{ [cm}^{-1}\text{]}$$

The purpose of  $\mu_s'$  is to describe the diffusion of photons in a random walk of step size of  $1/\mu_s'$  [cm] where each step involves isotropic scattering. Such a description is equivalent to description of photon movement using many small steps  $1/\mu_s$  that each involve only a partial deflection angle if there are many scattering events before an absorption event, i.e.,  $\mu_a \ll \mu_s'$ . This situation of scattering-dominated light transport is called the diffusion regime and  $\mu_s'$  is useful in the diffusion regime which is commonly encountered when treating how visible and near-infrared light propagates through biological tissues. This point is illustrated in Figures 1.17.

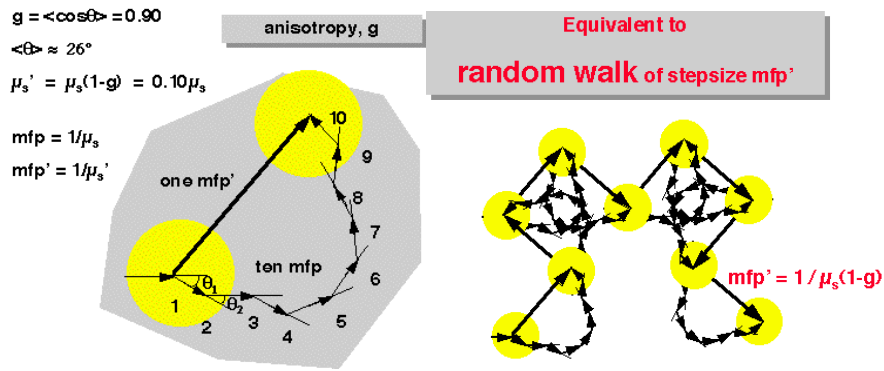


**Figure 1.17:** The figure shows the equivalence of taking 10 smaller steps of "mean free path"  $mfp = 1/\mu_s$  with anisotropic deflection angles and one big step with a "reduced mean free path"  $mfp' = 1/\mu_s'$  (left) and how many such big steps involving isotropic scattering are equivalent to many small anisotropic steps (right).

Combining absorption and scattering, one can define a transport attenuation coefficient  $\mu_{tr} = \mu_a + \mu_s'$  where  $\delta_{tr} = \mu_{tr}^{-1}$  is commonly referred to as the mean free path between either a scattering or absorption event or optical penetration depth, that is estimated to be less than 100  $\mu\text{m}$  in soft, noncolored tissue. In the visible range (400 - 700 nm), light penetration in terms of  $\delta_{tr}$  increases to about 200 to 1000  $\mu\text{m}$ . (Figure 1.18)

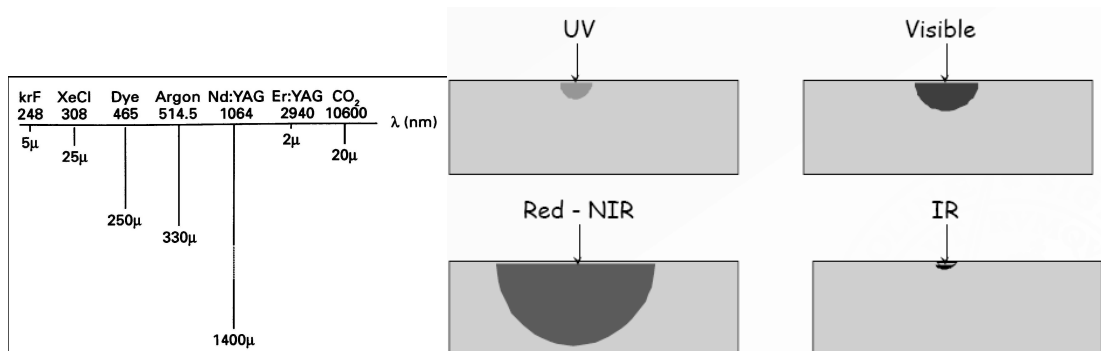


**Figure 1.18** Light penetration depth: (left) values in human skin at different laser wavelength; (right) schematic versus radiation wavelength where is increasing from UV range to visible range, decreasing correspondently absorption and scattering, maximum in red-NIR range, where both absorption and scattering are minimum, decreasing again in the IR range, principally for the increased absorption of water.

### 1.3.8 Scattering in biological tissues

In biomedical optics, scattering of photons is an important event. Scattering provides feedback during therapy. For example, during laser coagulation of tissues, the onset of scattering is an observable endpoint that correlates with a desired therapeutic goal. Scattering also strongly affects the dosimetry of light during therapeutic procedures that depend on absorption. The scattering affects "where" the absorption will occur. Scattering has diagnostic value. Scattering depends on the ultrastructure of a tissue, eg., the density of lipid membranes in the cells, the size of nuclei, the presence of collagen fibers, the status of hydration in the tissue, etc. Whether one measures the wavelength

dependence of scattering, the polarization dependence of scattering, the angular dependence of scattering, the scattering of coherent light, scattering measurements are an important diagnostic tool. Scattering is used for both spectroscopic and imaging applications.

The light scattered by a tissue has interacted with the ultrastructure of the tissue. Tissue ultrastructure extends from membranes to membrane aggregates to collagen fibers to nuclei to cells.

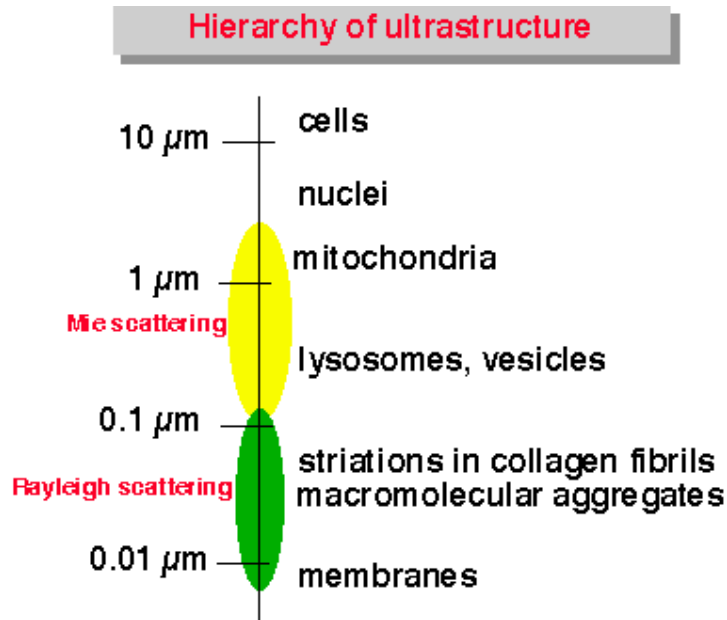


**Figure 1.19:** schematic of principal scatterers in the tissue: the scatterers linear dimensions are associated with the corresponding scattering events type for visible and infrared light.

Summarizing the precedent theoretical considerations, photons are most strongly scattered by those structures whose size matches the photon wavelength. Scattering of light by structures on the same size scale as the photon wavelength is described by Mie theory. Scattering of light by structures much smaller than the photon wavelength is called the Rayleigh limit of Mie scattering, or simply Rayleigh scattering.

The Figure 1.19 designates the size range of tissue ultrastructure which affects visible and infrared light by Mie and Rayleigh scattering. Mitochondria are intracellular organelles about 1  $\mu\text{m}$  in length (variable) which are composed of many folded internal lipid membranes called cristae. The basic lipid bilayer membrane is about 9 nm in width. The refractive index mismatch between lipid and the surrounding aqueous medium causes strong scattering of light. Folding of lipid membranes presents larger size lipid structures which affect longer wavelengths of light. The density of lipid/water interfaces within the mitochondria makes them especially strong scatterers of light. Collagen fibers (about 2-3  $\mu\text{m}$  in diameter) are composed of bundles of smaller collagen fibrils about 0.3  $\mu\text{m}$  in diameter (variable). Mie scattering from collagen fibers dominates scattering in the infrared wavelength range. On the ultrastructural level, fibrils are composed of entwined tropocollagen molecules. The fibrils present a banded pattern of striations with 70-nm periodicity due to the staggered alignment of the tropocollagen molecules which each have an electron-dense head group that appears dark in the electron micrograph. The periodic fluctuations in refractive index on this ultrastructural level appear to contribute

a Rayleigh scattering component that dominates the visible and ultraviolet wavelength ranges.

The extracellular fluid has an effective refractive index between 1.348 and 1.351, influenced by concentrations of e.g. electrolytes, alcohols, glucose and fructose (16, 29). Refractive indices of the cytoplasm have been determined to be 1.3703 to 1.38 (30, 31) and of the nucleus of Chinese hamster cells 1.392 (31). Components of higher index of refraction, such as lipids (1.46) and proteins (1.51), are also present in tissue (33, 34). Membranes in the cell, e.g., consist of phospholipid layers with proteins, and the refractive indices have been found to be in the range 1.43 - 1.51 (30). Since the fraction of components of higher refractive index is fairly low (about 5 %) (30), the effective cellular refractive index can be estimated to approximately 1.40. Scattering is thus expected to occur from cell membranes, organelles and proteins (30), or entire cells. For instance, the main scatterer in blood is the entire red blood cell (RBC) (16). Based on the numbers above, the relative refractive index,  $m$ , between cytoplasm or extracellular fluid and phospholipid bilayer membranes would be in the range 1.03 - 1.10. The size of the scattering centers is expected to range from proteins, with sizes measured in Angstroms, to cells with diameters of up to 20  $\mu\text{m}$ . A few examples of diameters include the hemoglobin molecule, 64  $\text{\AA}$ , nucleoli and chromatin, 1  $\mu\text{m}$ , mitochondria and nuclei, 1-5  $\mu\text{m}$ , and mammalian cells, 3 to 20  $\mu\text{m}$ . Corresponding size parameters,  $x$ , at  $\lambda = 632.8 \text{ nm}$ , if these scattering centers were spherical, would be between 0.06 and 198.6. Both the structural arrangement and configuration of cells, organelles and macromolecules, as well as the cellular content of various organelles, strongly influence the scattering properties. It has, for example, been seen that immature and thin (compared to the wavelength of the incident light) collagen fibers yield isotropic scattering, whereas enlargement of the fibers, as seen in the maturation process, increases the anisotropy (34). On a cellular level, both the cell membrane and the nucleus have high refractive indices, whereas the mitochondria have low refractive indices (30). However, parameters such as structure, size and concentration of the scattering objects must also be taken into account, in considering what part(s) of the cell or tissue will mainly contribute to their respective scattering properties. As an example, tissues of high mitochondrial content, e.g. liver, exhibit a high  $\mu_s'$  (35). This is most likely mainly because of the large volume fraction of mitochondria in hepatocytes (about 20 %) (35). On the other hand, a low correlation has been found between  $\mu_s'$  and the tissue DNA content (33), in spite of the high refractive index of the nucleus. A likely explanation for this, is the low volume fraction of nuclear membrane structures (0.2 - 0.7 %) (30). Finally, lipid droplets inside adipocytes have been shown to contribute strongly to cellular scattering, both because of their high index of refraction, and high volume fraction in the adipose tissue cells (35). The scattering coefficients of various tissue types are wavelength dependent, and decrease monotonically with increasing wavelength (15). As can be understood from the discussion above, the various tissue constituents causing light scattering have a wide size distribution, indicating that they have different scattering efficiencies, and cause different degrees of anisotropy. It has been shown, that the compound scattering coefficient of dermis, as a function of wavelength, can be described by combining the highly wavelength dependent, and nearly isotropic, Rayleigh scattering with the more forward peaked Mie scattering distribution, in this case cylindrical Mie theory with a  $\lambda^{-1.5}$  dependence.

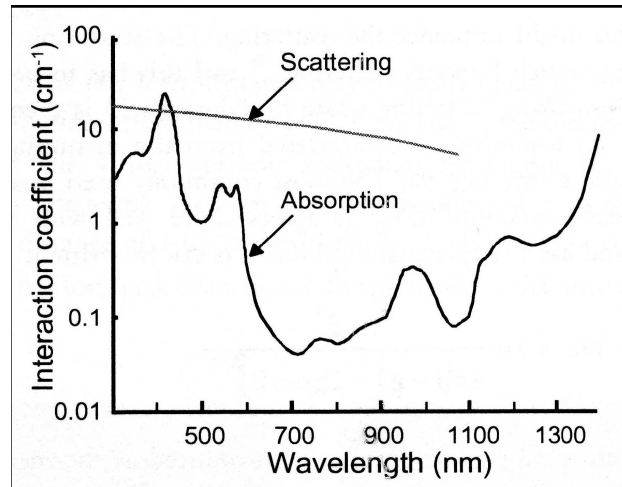


**Figure 1.20:** Scattering and absorption factors within the tissue optical window.

## 1.4 Conclusions

Up to this point, we have focalized two fundamentals features about the interaction light and biological tissue. First, the dominant phenomena in light propagation in tissue are scattering and absorption, being the scattering dominant with respect the absorption. Second, both are wavelength dependent: the scattering is decreasing with wavelength, while the absorption presents a dependence more complicated from wavelength, but such that it is possible identify a spectral range, called optical windows, comprised between 650 and 900 nm, in which the penetration depth in tissue is maximum, being there minimum both scattering and absorption (Figure 1.20).

Hence, the photons light travel in the biological medium doesn't impair the tissues, but yields a lock of information carried out by light photons. So, if the optical methods in biomedical applications (diagnosis and therapy) are ideal candidates as intrinsically non invasive, their analysis power is limited to superficial phenomena. We have so furnished the principal prerequisite to understand the drawbacks and the advantages of the optical imaging technique reported in the successive chapters.

# Chapter 2

## *Planar Fluorescence Imaging*

### 2.1 *Introduction*

In this chapter we will focalize on the fluorescence reflectance imaging (FRI) technique as research tool in the field of the biomedical optical imaging performed *in vivo* on small animals to study mice models of human, in particular oncological, diseases. First, we recall the principia of the fluorescence as physical event and we discuss how the tissue fluorescence emission depends by environmental factors, how the interaction tissue-fluorescent photons affect the fluorescence detected and how the tissue endogenous components fluorescence can be a diagnostic tool. After explaining the new role of *in vivo* on small animals optical imaging for the diseases studies in proteomic and genetic terms, the fundamentals of FRI technique relatively to the experimental apparatus and methods will be considered. Then, we will offer an overview of the different FRI techniques relatively to the fluorescence labelling strategy of the biological target of interest, distinguishing non specific, targeted and activatable fluorochrome, beyond fluorescent protein and bioluminescence. In particular, we also refer on the properties of the porphyrin compound family to which belongs our fluorescent marker, hematoporphyrin (HP) dychlorohydrate. The advantages and drawbacks of the FRI techniques, in general, can be illustrated so in the next chapters we can put our HP mediated FRI in comparison with the other FRI techniques that have been developed in the more recent years.

### 2.2 *Biomolecules fluorescence*

#### 2.2.1 *A brief history*

In 1852 Stokes described the phenomenon of fluorescence observed in fluorite (36), which, irradiated by UV source, gave off radiation at a longer wavelength. In 1911 Stübel reported that most animal tissues were fluorescent upon UV illumination (37). Fluorescence was detected by the naked, un-aided eye, and classified according to apparent color: light green fluorescence from rabbit fat, and dark brown, or slightly greenish fluorescence from rabbit cardiac muscle (37). Thirteen years later, Policard discovered red fluorescence in animal tumors, exposed to a Wood's lamp (38) and suggested that this fluorescence was due to accumulation of endogenous porphyrins. So he performed an important first step towards realizing both the potential of fluorescence as a biomedical diagnostic tool, and the importance of the porphyrins as possible tumor markers.

Then, the fluorescent molecules, or fluorophores, responsible for the endogenous tissue fluorescence, called autofluorescence, have been extensively investigated, (39-50) and many diagnostic applications have been found that are based merely on the autofluorescence (51). Further, multiple exogenous fluorophores have been studied, enhancing the diagnostic potential of fluorescence considerably (52). Biomedically, fluorescence has been used in fluorescence microscopy, flow cytometry and cell sorting for some time. In addition, *in vivo* fluorometry applications are becoming established,

including tissue metabolic studies, cardiovascular diagnosis, and applications in ophthalmology and oncology (52). The latter application interests most of the fluorescence imaging and spectroscopy studies *in vivo*: the final goal is the detection of neoplasia, possibly at an early stage, probing tissue with light. So an “optical biopsy” is realized that in real time yields a histological, chemical and metabolic diagnosis, instead of the invasive, time consuming and costly procedure of removing tissue biopsies surgically for later microscopic analysis (52-59).

### 2.2.2 Fluorescence

As was briefly mentioned in the previous chapter, fluorescence is one of the possible results of resonant absorption of a photon in a molecule. The molecule is normally in its electronic ground state, which in most cases is the singlet state with the lowest energy,  $S_0$  (see the Jablonski diagram in Figure 2.1). One notable exception is the  $O_2$  molecule, which has a triplet ground state. These electronic levels are characterized by the resulting spin vector of the electrons in the molecule: singlet states exhibit a zero sum of the electron spin quantum numbers, whereas the spin of one electron has changed sign in the triplet states. The electronic levels of a molecule correspond to the energy levels of an atom, and are determined by the atomic and electron configuration of the molecule. A typical separation in energy between electronic levels is a few eV, corresponding to photons with a wavelength of 100 to 1000 nm; i.e. encompassing the range of visible light. The electronic levels are further subdivided into several vibrational levels that are further subdivided into rotational levels. The latter two are determined by the movements of the atomic nuclei of the molecule. The lower-lying vibrational levels are typically separated by fractions of eV (about 0.1 eV), which corresponds to EM radiation of about 10  $\mu\text{m}$ . Finally, the separation between rotational levels is about 0.001 eV, or roughly EM radiation of about 1 mm. For large molecules, the intervals between the different levels are very small, and may sometimes overlap due to molecular interactions (7, 59-61).

The vibrational structure of an electronic transition, e.g. from  $S_0$  to  $S_1$ , is explained by the Franck-Condon principle, which states that an electronic motions takes place considerably faster than those nuclei, since the nuclei are much more massive than the electrons. An electronic transition that occurs without change of nuclear geometry is called a vertical transition (Figure 2.1). Electron density is rapidly built up in new regions of the molecule, and removed from others, as a result of the electronic transition; thus, the nuclei suddenly experience a new force field, and will start to vibrate (in classical terms, the nuclei are considered initially stationary). The equilibrium bond lengths of an excited electronic state are usually shifted to greater internuclear separations compared to the electronic ground state, since the excited state has more antibonding character. Hence, the initial internuclear separation (where the molecule is in the lowest vibrational state of the electronic ground state) will be one of the two stationary turning points (the one with the shortest internuclear separation) in the vibrational motion of the excited electronic state. This is the explanation why the excited molecule is more likely to end up in a higher vibrational level than the lowest one, in its excited electronic state. Molecules are not long-lived in their excited states, and a rapid relaxation (picoseconds), through non-radiative kinetic interactions with surrounding molecules, internal conversion (IC), to the lowest

rotational-vibrational state of  $S_1$  will ensue, generating heat. The rapid relaxation is a result of the high density of rotational-vibrational levels (7,60)

From the lowest rotational-vibrational level of  $S_1$ , the molecule can either relax back to  $S_0$  through spontaneous emission of a photon of longer wavelength than the incident photon, since some energy has been lost to IC in the excited singlet state, and since the molecule may return to any of the many rotational-vibrational levels in  $S_0$ . This process is called fluorescence. The shift in wavelength from the absorbed photon exciting the molecule, to the fluorescent photon, is denoted the Stokes shift. The distribution of energies of the fluorescence photons, i.e. the fluorescence spectrum of the molecule, will reflect the probability of transitions to the rotational-vibrational levels contained in  $S_0$ , in accordance with the Franck-Condon principle. In a gaseous sample, the complex electronic spectra of a molecule, with a multitude of rotational-vibrational levels, may be resolved. However, in a liquid or solid phase, the molecules are interacting more closely, and the rotational and vibrational lines of the electronic levels usually merge together, resulting in broad, almost featureless absorption and fluorescence bands. Typically, the lifetime of fluorescence emission is on the order of nanoseconds. Finally, the molecule will return to its ground state, the lowest rotational-vibrational level of  $S_0$ , once again through internal conversion. Consequently, the fluorescence process is reversible, which is an advantage in a diagnostic setting (7, 59, 61).

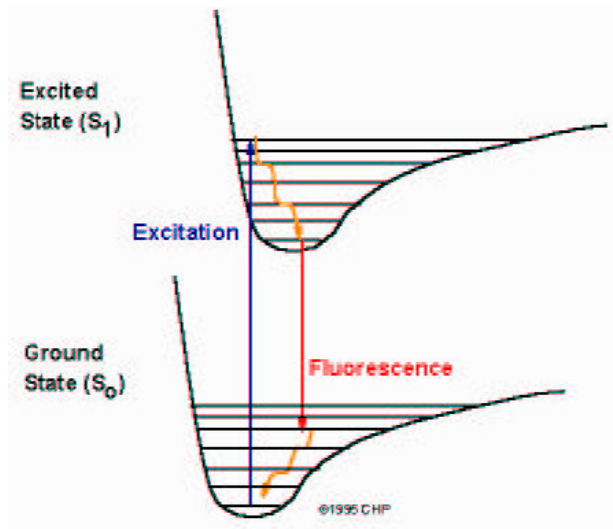


**Figure 2.1** Molecular energy level diagram illustrating the Franck-Condon principle. The transition from the lowest vibrational state of  $S_0$  to the vibrational state in  $S_1$  lying vertically above it (vertical transition) is illustrated by an arrow.  $S_1$  is in this case displaced to greater equilibrium bond lengths compared to  $S_0$ . In classical terms, the initial separation (corresponding to the sink of  $S_0$ ) becomes a stationary turning point in the final electronic state. In the quantum mechanical version of the Franck-Condon principle, the transition is from the lowest vibrational state of  $S_0$ , as illustrated in the figure.

### 2.2.3 Biomolecules fluorescence features

Fluorescent molecules have one structural feature in common – an unbroken chain of conjugated double bonds. Hence, the molecular structure of porphyrins (essentially four

pyrrole rings linked by methane bridges) is a good example of a fluorophore, as will be showed in a next paragraph (59,61).

The surrounding environment affects the molecules fluorescence. If the fluorophore is in a solution, both pH and polarity of the solution will affect the fluorescence properties. Polar solutions, such as H<sub>2</sub>O, can dramatically increase the Stokes shifts of fluorophores, compared to the situation in non-polar solutions (59). Another important factor is quenching of fluorescence, which will affect both fluorescence quantum yield, i.e. the fraction of the decay that proceeds through a fluorescence pathway (62), and fluorescence lifetime, the average time a molecule stays in S<sub>1</sub>. Quenching can be caused by coupling of the fluorophore to certain molecules, and is temperature dependent. Quenching can also occur if a solvent is composed of molecules with widely spaced vibrational levels (such as water), that can accept large quanta of electronic energy from the solute (fluorophore) (60).

It is to be pointed out that tissue structure, i.e. histology, the biochemical and metabolic states affect both light scattering and absorption<sup>2</sup>. Tissue fluorescence detected will be influenced both directly by the metabolic state and structural alterations of tissue in the emission fluorescence phase; and indirectly, because the emitted fluorescence photons will also be scattered and absorbed in tissue, before they can be detected and, hence, all parameters of tissue pathology will affect the detected fluorescence. Hence, both excitation and fluorescence light is subject to absorption and scattering in the tissue, but differently because of the Stokes shift and the wavelength dependence of the tissue optical properties (Figure 2.2). So, Monte Carlo simulations have shown that 35-40% of the fluorescence photons are remitted in the forward direction, away from the tissue surface (63); thus, resulting in a greater probing depth than would be expected based on the optical properties at the excitation wavelength, since the light attenuation is less pronounced for the Stokes shifted light.

As regard the absorption effects on fluorescence detected, one of the main chromophores is the hemoglobin. First, the Soret band of HbO<sub>2</sub> at 418 nm often interferes with the excitation process, since many fluorophores have their main absorption peak in this region. Most porphyrins, e.g. have their main excitation peak (Soret band) close to 405 nm, with a characteristic dual peaked fluorescence in the red at about 630 and 690-700 nm (Figure 3.2)(53). Second, the endogenous fluorescence of a biological tissue usually peaks in the blue-green region, e.g. at about 490 - 500 nm after 425 nm excitation (58). Thus, the Q-bands of hemoglobin have the potential of creating re-absorption dips in the fluorescence spectrum. This interaction both reduces the "true" fluorescence signal, and creates artificial peaks in the fluorescence spectrum. Obviously, other tissue chromophores may also influence the propagation of fluorescence photons.

In addition, the high and varying wavelength dependent scattering coefficients of tissue (53) can cause apparent changes in the spectral shape of the detected fluorescence (52). Similar discrepancies arise if one tries to compare fluorescence measurements using various optical configurations, e.g. varying source detector separations, both due to different sampling depths and light attenuation.

---

<sup>2</sup> Hence, a method designed to monitor these alterations could be used in detecting e.g. neoplasia, which is discussed in a review article by Bigio and Mourant (52).

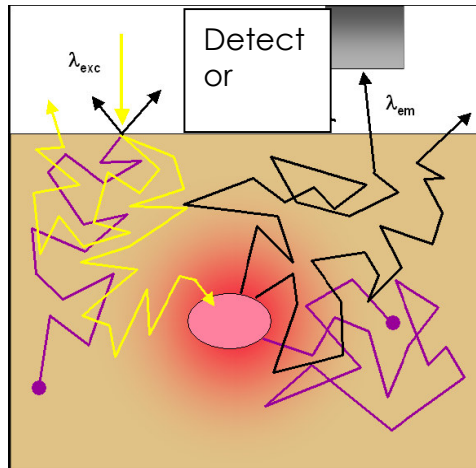


**Figure 2.2** The scattering and absorption phenomenon affects both excitation light moving from interface to fluorescent target and fluorescent light emitted from fluorescent target moving from it to the interface, with the difference that the fluorescent light suffers minor attenuation than excitation light being of wavelength longer.

## 2.2.4 Autofluorescence

Besides absorption and scattering, tissues are inherently characterized by autofluorescence since all tissues contain low amounts of fluorophores which absorb light and subsequently emit light at a higher wavelength. Andersson-Engels *et al* have reported on the fluorescence of some fluorophores suspected to be of relevant importance (51). Thus, using an excitation wavelength of 337 nm, tryptophan and collagen display fluorescence peaks at about 390 nm, elastin at 410 nm, NADH at 470 nm and carotene at 520 nm. All peaks are broad with FWHM on the order of 100 nm. These values are given for the purified compounds in solution. Endogenous porphyrins are excited using light slightly above 400 nm, yielding red fluorescence. Further, oxidized forms of riboflavin, flavin mononucleotide and dinucleotide, emit a strong fluorescence at around 515-520 nm, after excitation at 450 nm (64).

Because a general goal in diagnostics is to inflict no harm, and to be non-invasive, it would be advantageous if fluorescence diagnostics could be based merely on endogenous fluorophores: thus, reducing the risks of the diagnostic procedure to that of the ultraviolet radiation used in excitation of the fluorophores, especially for internal organs (52). Indeed, as normal tissue becomes dysplastic, there is a change in the spectroscopic properties of the tissue based likely on changes in the concentration of these components (65). Laser-induced autofluorescence spectroscopy (LIAFS) was first employed in the early 1980s to differentiate normal from tumorous tissues (66). This technique is based on fluorescence intensity spectra, which are acquired at excitation with different wavelengths. It has been shown, for instance, that bladder tumors exhibit a significantly lower fluorescence compared with normal tissue when examined with LIAFS (67). Bigio and Mourant (57) have presented a summary of clinical studies using autofluorescence and various metrics to discriminate adenomas, dysplasia and malignancies from normal surrounding tissue, in various organs *in vivo* (52). Results are impressive, with sensitivities and specificities in most cases in excess of 90 %, e.g. in uterine cervix, colon and esophagus. In the case of skin malignancies, results are more ambivalent. Some studies have claimed it to be possible to

distinguish non-dysplastic naevi from melanoma and dysplastic naevi, merely using autofluorescence with 365 nm excitation. Multiple studies have shown that the overall intensity of the autofluorescence is decreased in neoplastic tissue, compared to surrounding non-transformed tissue (55-58,64). Consequently, it has been suggested that an enhanced tumor demarcation can be achieved by incorporating the reduced autofluorescence in a diagnostic criterion, e.g. by normalizing the fluorescence signal from an administered tumor localizing exogenous fluorophore with the endogenous fluorescence.

A particular case is the protoporphyrins IX, a class of porphyrins that have been shown to accumulate in pre-malignant tissue and that exhibit favorable fluorescence properties with an excitation peak at 450 nm and a significant Stoke's shift (emission in the NIR at 620 nm). An endogenous precursor of these protoporphyrins (5-aminolevulinic acid, ALA) can be applied systemically in order to increase endogenous autofluorescence of malignant tissue. This technique has been successfully applied for the detection of dysplasia in Barrett's esophagus and colitis in endoscopic imaging (68). Whereas this approach focuses on enhancing the inherent autofluorescence of the tissue, specific or rather molecular events cannot be targeted using the autofluorescence detection.

Through several molecules are responsible for the autofluorescence of various tissues, however, the problem with autofluorescence techniques is that the autofluorescence emission spectrum will vary from tissue to tissue, and is dependent on excitation wavelength. Further, the SNR for early-stage diseases is low, due to low amounts of fluorophores and the relatively high background (e.g., scattering, reflection), which limits the applicability of these optical signatures for early cancer detection (66).

The Figure 2.3 shows an autofluorescence excitation-emission matrix (EEM), a matrix which contains the autofluorescence intensity as a function of excitation and emission wavelength, obtained *in vivo* at different excitation wavelengths (69). The excitation range, denoted as  $\lambda_x$ , is from 337 to 610 nm, and the emission range ( $\lambda_m$ ) is from 360 to 750 nm. It is noteworthy that the much lower tissue autofluorescence at longer wavelengths again justifies the preferential use of fluorochrome with excitation and emission wavelength shifted in the red-NIR spectral region, hence in the optical window where also absorption and scattering events are minimal.

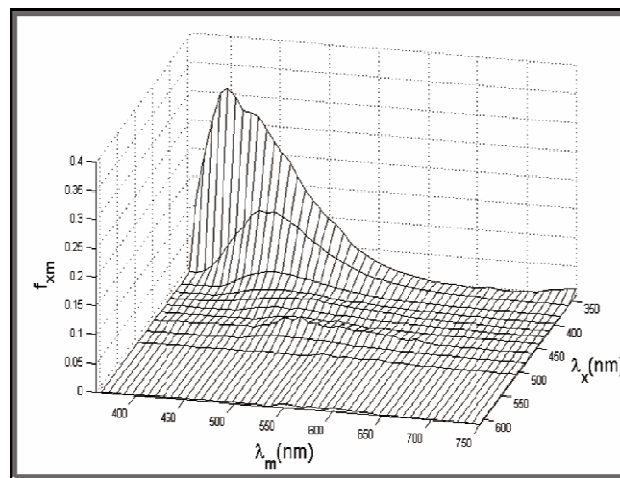


**Figure 2.3** Autofluorescence excitation emission spectrum. The autofluorescence intensity decreases with increasing of both excitation  $\lambda_x$  and emission  $\lambda_m$  wavelength, becoming almost constant in the red-NIR region.

### 2.3 *Optical imaging in vivo on small animals*

What is optical imaging? It could be defined as a visualization in space and/or time of normal as well as abnormal cellular processes involved in tissues of biomedical interest, at molecular or genetic level, by using the optical radiation as an analysis instrument.

Tissue observation with light is probably the most common imaging practice in medicine and biomedical research ranging from the simple visual inspection of a patient to advanced *in vivo* and *in vitro* spectroscopic and microscopy techniques (70). While intrinsic tissue absorption and scattering yields significant information on functional and anatomical tissue characteristics, significant attention has also been given to fluorescence investigations of tissue since many biochemical markers can be retrieved due to fluorescence contrast, and many more can be targeted using appropriate fluorescent markers (71,72). Numerous different optical imaging approaches can be used for imaging fluorescence *in vivo*. Traditionally, optical methods have been used to look at surface and subsurface fluorescent events using confocal imaging (73-75), multiphoton imaging (76-79) microscopic imaging by intravital microscopy (80,81) or total internal reflection fluorescence microscopy (82). Recently however, light has been used for *in vivo* interrogations deeper into tissue using photographic systems with continuous light (83-86) or with intensity-modulated light (87) and tomographic systems (88-89). Potentially, phased-array detection (90) can also be applied. This recent focus in macroscopic observations of fluorescence in tissues has evolved due to the potential of transferring this technology to imaging through animals and humans (71).

The considerable increased interest in the use of optical methods for medical imaging, diagnosis and therapy<sup>1</sup> is motivated by various and different factors. First, the considerable potential of the optical approaches has now become feasible because of the technological development of the component of the experimental apparatus, essentially monochromatic light sources (lasers) with higher but nevertheless safely delivered power per wavelength compared with white-light illuminators, and highly sensitive detectors with the associated data acquisition and analysis software. Second, different optical techniques have already been developed and used for many years in the molecular biology community to probe tissue samples or cells (such as, for example, the use of fluorescent proteins and fluorescently labelled antibodies). These techniques can be adapted and modified for *in vivo* applications. Further, since the techniques are of very sensitivity, where the autofluorescence of tissues is very low, a high SNR can be achieved even when low amounts of fluorescent reporter are present at the target. Then, this technology has become feasible mainly due to the development of fluorescence probes emitting in the near-infrared spectrum where tissue offers low absorption and minor scattering, whereas also the autofluorescence is minimum. A further catalyst has been the erosion of traditional boundaries that separated physicists, engineers, mathematicians, computer scientists, chemists, cell and molecular biologists and physicians and the establishment, at many leading institutions, of interdisciplinary programmes where the imaging sciences and biology are seamlessly integrated. Finally, different functional

paradigms can be applied for optical contrast agents, such as fluorescence energy transfer or bioluminescence, in order to detect specific target interactions *in vivo* such as enzyme activity.

From a some point of view, fluorescence imaging is nothing new: fluorescently labelled contrast agents that bind to specific proteins, particularly cell-surface receptors, have been employed for decades in cell culture. These techniques have since migrated to the *in vivo* environment. What has changed over the last several years, acting as a catalyst for the explosive growth and popularity of optical (and not only) imaging, is the extraordinary avalanche of information regarding the specific genes and proteins involved in disease mechanisms, the sequencing of the human genome (and more recently, the mouse genome) and the advent of combinatorial chemistry and mass screening techniques that produce large numbers of candidate molecules that can interact with a particular biological target of interest. In addition, the imaging field has embraced this opportunity by discovering and developing a range of novel approaches for generating protein and gene specific contrast in an image, and through stunning improvements in the imaging technologies themselves, particularly at the level of *in vivo* small-animal imaging. This is important, because as the genomic era provides us with better animal models of cancer and more specific therapeutics, better methods are needed to monitor tumour development in animals. The goal of molecular imaging is to image specific proteins, genes or the biochemical and molecular pathways they are involved in, within intact living subjects. The ultimate goal is to know where specific proteins or genes are expressed in the body, the level at which they are expressed and how that distribution and level changes over time or following an intervention.

## 2.4 *Fluorescence Reflectance Imaging: FRI*

Specifically, we focus on reflectance fluorescence imaging, which is the most common approach currently used for imaging *in vivo* fluorescent probes in tissues.

### 2.4.1 *Technology*

Reflectance imaging is a simple “photographic methods”, in which the light source and the detector reside on the same side of the object imaged. Fluorescence reflectance imaging (FRI) is currently the typical method for accessing the distribution of fluorescent probes *in vivo*, but the method can be applied more generally to imaging fluorescent proteins or even bioluminescence even if in the latter case no excitation light is used (91). FRI operates a source of light whose wavelength falls in the excitation band of the fluorescent molecule used as optical contrast agent or molecular probe. The fluorescence signal can be resolved with an emission filter and captured by a high-sensitivity CCD camera. A typical reflectance imaging system is shown in Figure 2.4.

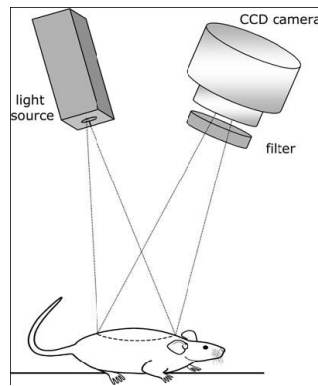


**Figure 2.4** Typical fluorescence reflectance imaging (FRI) system for in-vivo animal investigations. The illumination source and CCD camera are on the same side of the animal imaged. The components shown are usually enclosed into a light-tight box.

The two key light sources for fluorescence detection systems are lamps and lasers. Lamps are usually inexpensive and can yield high output powers, but are more difficult to efficiently couple to optical fibers in endoscopic applications, and may require multiple filters to select the appropriate wavelength. Lasers, on the other hand, have the advantage of high output power within a narrow wavelength band (temporal coherence), and a high spatial coherence, simplifying the coupling to optical fibers. Further, both continuous and pulsed lasers exist, allowing e.g. the introduction of gated detection, triggered by the light pulses. Fixed-frequency lasers operating at a certain wavelength, determined by the lasing medium, can be used to pump tunable lasers; thus, yielding light at another wavelength, depending on the lasing medium used in the tunable laser. The laser beam is expanded on the animal surface with an optical system of lenses (not shown). Narrow wavelength selection is important, especially in the NIR, whereas the excitation and emission spectra overlap and it is likely that excitation photons can propagate into the fluorescent images.

The CCD camera is usually a high-sensitivity camera since fluorescent signals are of low strength, while CCD chip resolution and dynamic range are not crucial factors in these types of systems since the targeted measurement is a diffuse-light measurement, emanating from a virtually flat surface. In the fluorescence measurements the detection sensitivity limit is set by the background tissue fluorescence (background probe distribution and auto-fluorescence); therefore, fluorescence strength can be adjusted above the camera noise floor by optimizing illumination strength and acquisition times, so that the noise requirements of a CCD camera for fluorescence imaging are not as stringent. Instead, in the bioluminescence measurements the detection sensitivity is usually set by the CCD camera noise floor.<sup>3</sup>

Typically, the fluorescence image acquired is accompanied by a second image measured without the fluorescence filter. The animal “photograph” obtained for registration purposes at the excitation wavelength also serves as a calibration measurement since it records the exact spatial distribution of the excitation light strength for later correction of excitation field inhomogeneities. It is noteworthy that the

<sup>3</sup> Detection systems that scan a single spot over a field of view and detect light using photo-multiplier tube detectors have also been reported (92). Such systems may offer greater dynamic range than CCD-based systems but compromise resolution, acquisition frame rate, and overall noise characteristics, and are not widely used in in vivo fluorescence reflectance measurements.

fluorescence (or luminescence) image, recording fluorescence signals emanating from under the surface and using mainly the diffuse component of light, is by nature a low-resolution image, while the intrinsic light image records the structure on the animal surface and can yield high-resolution images after appropriate focusing. The side-by-side comparison or the superposition of the two images into a single image yields a good visual effect since high resolution is retained.

The fluorescence imaging measurements *in vivo* on small animals are sometimes accomplished by fluorescence spectroscopic measurements on histological sections of healthy/diseased mice tissue to obtain a control measurement of the imaging results.

## 2.4.2 Targeting strategies

In order to obtain molecular information from an intact organism, several fundamentals have to be fulfilled. First of all, it is essential to define a target, which is highly relevant for the pathology to be imaged. Secondly, the target needs to be sufficiently characterized so that optical sensors with a high selectivity and affinity for the target can be developed. Thirdly, since imaging should ultimately be performed *in vivo*, a drug delivery paradigm has to be applied, which allows for sufficient delivery of the molecular probe to the target. Finally, if possible, signal amplification strategies should be applied in order to improve the signal-to-noise ratio (SNR) for molecular structure detection (93-94).

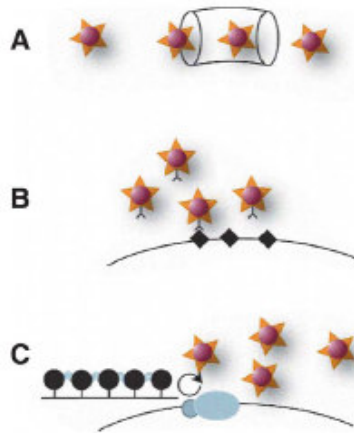


**Figure. 2.5 A-C** Design of different optical contrast agents. **A** Whereas non-specific fluorochromes, such as indocyanine green or porphyrins, show simple perfusion and/or permeability properties of the tissue, **B** targeted probes bind via specific ligands to protein structures on the cell surface. Targeting of tumor-associated receptors, such as the somatostatin receptor, allows for specific detection of cancerous lesions. **C** “Smart” probes are activated by enzymatic conversion. Whereas these probes are virtually non-fluorescent in their native state (**C, left**) due to fluorescence energy transfer, they become brightly fluorescent once the fluorochromes are released from the backbone (**C, right**).

Various strategies can be pursued to obtain optical information from the tissue ranging from endogenous tissue contrast<sup>4</sup> to non-specific, targeted, or “smart” optical probes (Figure 2. 5) (104). The choice of the targeting modality depends on the study objective. In general, if the scope is disease (tumor) diagnosis, then the non specific fluorochrome is a useful choice. If, instead, it is necessary to determinate the molecular and/or genetic pathway of the disease, then a more specific fluorochrome must be used.

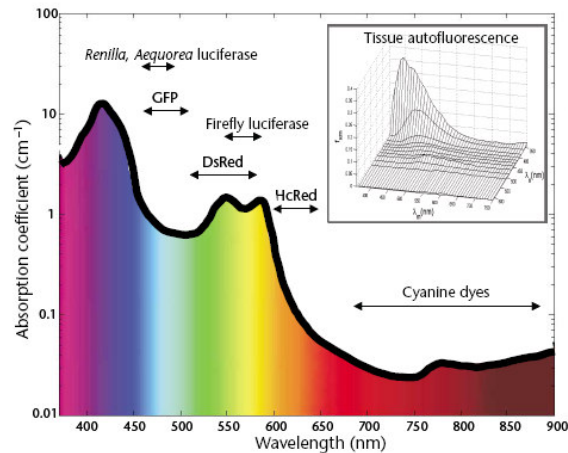


**Figure 2.6.** The emission range of several common fluorochromes and luciferases used for imaging on the tissue absorption coefficient graph calculated assuming normally oxygenated tissue (saturation of 70%), a hemoglobin concentration of 50 mM, and a composition of 50% water and 15% lipids.

In general, fluorochromes for optical imaging should ideally fulfill some criteria in order to be suitable for in vivo diagnostic imaging:

1. Excitation and emission maxima in the red-NIR range (600–950 nm) (Figure 2.6)(4)
2. High extinction coefficient
3. High quantum yield (i.e., strong fluorescence signal)
4. No photo-bleaching
5. No photo-sensitizing effects
6. Hydrophilicity
7. Low toxicity

<sup>4</sup> Photons interact with tissue by absorption, scattering, and reflection. Generally speaking, absorption of light in the NIR is due mainly to the hemo- and myoglobin content within a given volume and thus dependent on vascularization and/or perfusion in the tissue. Scattering, however, is determined by refraction leaps, which are dependent on tissue architecture and intracellular composition such as density of organelles (e.g., mitochondria) (95,96). Classic diaphanic/transillumination imaging thus depicts a combination of absorption and scattering processes in the tissue. In the early years, optical mammography, for instance, tried to apply this principle to medical practice. Whereas a few studies in the 1980s reported favorable results for optical mammography compared with radiological screening (97-99), other studies discouraged the use of light for breast cancer diagnostics mainly due to poor sensitivity and specificity (100-102). More recently, multi-spectral imaging measuring the spectral dependence of tissue absorption and scattering provide additional information concerning tissue contents (water, lipids, oxy- and deoxy-hemoglobin) which may be useful in managing breast disease (103).

### 2.4.2.a Non specific fluorochromes

Two principal non specific fluorochromes family will be considered: cyanine dyes and porphyrins.

#### Cyanine dyes

Cyanine dyes (CD) represent one of the most prominent classes of optical contrast agents with ideal properties for in vivo imaging. The chromophore's optical properties are adjustable offering high extinction coefficients with the desired absorption and emission ranges throughout the visible to the near-infrared range (66). At the same time, CD can be conjugated to specific ligands, which can impart molecular specificity within the optical probes (see next paragraph).

Indocyanine green (ICG, cardiogreen) is one example for a non-specific fluorochrome, which has been used clinically for many years for hepatic function testing, cardiac physiology tests, and ophthalmological fluorescence angiography (105-107). It is a safe imaging agent, having been used in tens of thousands of patients with a reported side effect rate of <0.15%, an extremely favorable index as compared with other reporter agents<sup>46</sup>. In addition, it has been used in at least one clinical study as an absorber (not a fluorochrome) for enhanced tumor detection<sup>31</sup>. Experimental studies have proven the feasibility of tumor detection using nonspecific CD fluorochromes (108-110). Moreover, in a clinical study on patients with various breast lesions, ICG proved to be an efficient tool for lesion detection (88).

Near-infrared fluorochromes with improved biophysical properties (solubility, quantum yield, stability, synthetic yield, conjugatability) have recently been developed<sup>47-49</sup> and open new avenues for high efficiency labeling of affinity molecules. Before they can enter routine clinical use, however, these fluorochromes will need to undergo testing and receive approval from the US Food and Drug Administration.

#### Porphyrins

##### Chemical properties

Pyrrole, or pyrrol, is a heterocyclic aromatic organic compound, a five-membered ring with the formula  $C_4H_5N$  (Figure 2.7). Pyrroles are components of larger aromatic rings, including the porphyrins of heme, the chlorins and bacteriochlorins of chlorophyll, and the corrin ring of vitamin B12.

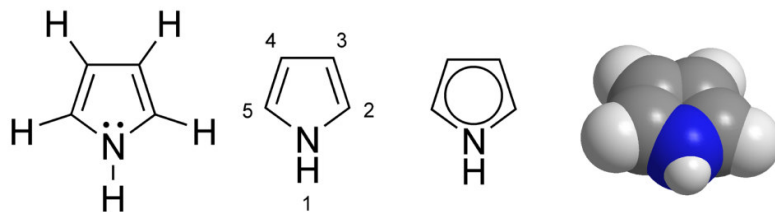
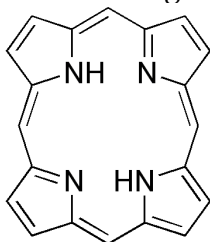


Figure 2.7 Pyrrole structure

A porphyrin is a heterocyclic macrocycle made from 4 pyrrole subunits linked on opposite sides ( $\alpha$  position) through 4 methine bridges ( $=\text{CH}-$ ) (Figure 2.8). The macrocycle, therefore, is more aromatic than the related corrins, chlorins (2,3-dihydroporphyrin) and bacteriochlorins (2,3,12,13-tetrahydroporphyrin). The extensive conjugated system makes the compound chromatic, hence the name porphyrin, from a Greek word for purple. The macrocycle has 22 pi electrons, 18 of which are active in the conjugated system. Porphyrins combine readily with metals, coordinating with them in the central cavity. Iron- (heme), magnesium- (chlorophyll), zinc-, copper-, nickel-, and cobalt- containing porphyrins are known, and many other metals can be inserted. A porphyrin in which no metal is inserted in its cavity is called a free base. Some iron-containing porphyrins are called hemes; and heme-containing proteins, or hemoproteins, are found extensively in biochemistry, e.g., hemoglobin. Hemoglobin iron is the actual transfer site for oxygen and can be preferentially bound up with carbon monoxide, thus poisoning by asphyxiation can occur. Some shellfish with green-colored blood have a copper-centered porphyrin. If one of the four pyrrole subunits is reduced to pyrroline, a chlorin is produced, the ring structure found in chlorophyll.

The number of double bonds in a row gives a rough estimate of the Q-band absorption wavelength. In the case of porphyrins, the number of double bonds is fairly large; hence, the Q-bands are located in the red region of the light spectrum.



**Figure 2.8** Porphyrin structure

### **Porphyrin for diagnostic purposes**

An overview of the main available diagnostic fluorophores is given by Andersson-Engels *et al*, (52) starting with the development of the first clinically significant photosensitizer and diagnostic fluorophore, hematoporphyrin (Hp) and a derivative thereof, hematoporphyrin derivative (HpD). Many of these substances have originally been developed for PDT purposes, and therefore carry potential side effects, such as skin photosensitization. However, reduction of dosage has been one way of minimizing the side effects. A multitude of studies, both experimental and clinical, have been published on the tumor marking properties of Hp and HpD,(53,111,112) showing tumor-to-normal substance related fluorescence intensity ratios of about 2-3:1, depending on the type of malignancy. However, if administered in therapeutic doses, general cutaneous photosensitivity may persist for several weeks (113). This fact combined with the heterogeneous chemical composition of HpD, and the presence of non-fluorescent aggregated material triggered the development of new sensitizers.

Several fluorophores have been developed and tested in tumor models, e.g. phthalocyanines (114), various chlorins (mono-aspartyl chlorin e6 (MACE) (115) and meso-tetra hydroxyphenyl chlorin (mTHPC) (116) and benzoporphyrin derivative (54). They all exhibit a strong fluorescence, but also have strong photosensitizing capabilities, which may be a drawback for diagnostic purposes. The tumor selectivity of the substance

uptake is not much better than that of HpD. However, Nelson *et al* did show that MACE does not induce any cutaneous photosensitivity because of a fast clearance rate. More recently,  $\alpha$ -amino levulinic acid (ALA) has been introduced as an attractive alternative for PDT (117). It is metabolized to protoporphyrin IX (PpIX) in the endogenous heme cycle (61), but PpIX has photophysical properties similar to those of HpD (52). Some research has been focused on finding exogenous fluorophores without any phototoxicity; i.e. these compounds could only be used for diagnostic purposes, and not PDT. Carotenoporphyrins have been found to demarcate MS-2 fibrosarcoma well in mice, with a tumor to peritumoral muscle concentration ratio of up to 30 (118). Takemura *et al* (119) have developed a chlorine derivative that is very tumor selective in a pancreatic cancer in hamsters, and without phototoxicity, but no numbers are given regarding the tumor selectivity.

### **Porphyrins tumor selectivity mechanisms**

Many different theories have been presented as to the mechanisms behind the relatively selective accumulation of porphyrins in neoplastic tissue. The tumor selectivity varies between different tumor models, and is not the same *in vitro* and *in vivo*. In some cases, there is no selectivity, possibly because of a poor vascular supply in fast growing malignancies. It has been proposed that the structure of the neoplastic tissue is more important for the selectivity, than the properties of the transformed individual cells. Evensen *et al* have pointed out that the large interstitial space of many malignant tumors, occupying about 50 % of the total tumor volume, or twice the fraction compared to normal tissue, may be important in this context (110). Porphyrins bind to plasma proteins after i.v. injection, (118,121) and will accumulate in the interstitial space, due to the increased endothelial permeability of neoplastic lesions. Once in the interstitium, these proteinporphyrin complexes bind to collagen, elastin and fibrin (122,123). Thus, a tumor to normal ratio of 2:1 may be expected, merely based on this mechanism. Indeed, this is the approximate ratio displayed for uptake of Hp, e.g. in an experimental colon adenocarcinoma in rats (53). In fact, tritiated water has shown the same uptake in a Lewis lung carcinoma in mice (124).

On a cellular level, it has been suggested that hydrophobic fractions of HpD traverse the plasma membrane of neoplastic cells, and by some mechanism are converted to highly fluorescent hydrophilic monomers inside the cell (125). Consequently, these monomers will in effect be trapped inside the cell. Porphyrin aggregates have also been suggested to enter cells through diffusion and pinocytosis (124). Another mechanism for retention of porphyrins in tumors, has been proposed to be due to the reduction of one half to one unit in pH in neoplastic tumors (126). The shift in pH will change the equilibrium towards more neutral, and less charged species of Hp. Since the neutral species are less soluble, they may be retained for a longer period of time in a malignant tumor. Further porphyrins bind to various plasma proteins, such as albumin and lipoproteins (118,121). Since the number of low density lipoprotein (LDL) receptors is increased on fast growing cells, especially malignant tumors, it has been suggested that porphyrin-LDL complexes will enter malignant cells preferentially (127). The uptake in this case would be through receptor-mediated endocytosis (128). However, there are also reports claiming that LDL inhibits the uptake of porphyrins into cells (129). *In vitro* experiments have shown that there is no difference between porphyrin uptake in normal and malignant cells in culture (130); hence, possibly supporting the aforementioned hypothesis, that the determining factor for

selective uptake of porphyrins in tumors, is the structure of the neoplastic tissue, and not so much the properties of the individual cells, even if the *in vitro* situation cannot be directly translated to the *in vivo* setting.

### 2.4.2.b Targeted fluorochromes

The two most common types of targets currently exploited in molecular imaging studies are enzymes and cell-surface receptors. Figure 2.10 (1) shows schematically how such a protein target could be imaged using the simple accumulation of a contrast agent. In this case the contrast agent molecules are designed to bind tightly to a cell-surface receptor protein found only on cancer cells. The contrast agent is also designed such that unbound contrast agent is cleared fairly rapidly by the body, either through the urogenitary or hepatobiliary systems. After the contrast agent is administered (usually by intravenous injection), it distributes rapidly throughout the body, accessing all the cells of the body. An image taken at this early time reveals little or no specific signal (Figure 2.10 (left)). But after waiting for some time, most of the unbound contrast agent has been cleared away, and the signal comes primarily from contrast agent molecules that are specifically bound to the receptors. Therefore, the image intensity reflects the distribution and density of these receptors (Figure 2.10 (right)). There is always some background due to contrast agent molecules that bind to other proteins in the body (no contrast agent is 100% specific), any contrast agent remaining in the circulation, routes of excretion of the contrast agent from the body and contrast agent that has been chemically modified so that it no longer recognizes the intended target. Minimizing this background is a key goal of contrast agent development. The timing of the imaging with respect to contrast agent administration depends on the type of contrast agent, and the time taken for distribution and clearance. For small molecule contrast agents, this process may only take a few minutes, while for larger biomolecules such as antibodies, it may take several days.

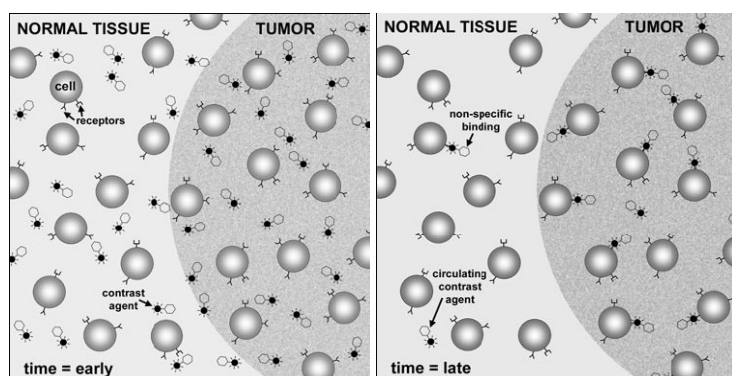


**Figure 2.10** Schematic diagram showing imaging of a cell-surface receptor found on cancer cells using a contrast agent designed to bind tightly and specifically to that receptor. At early times (left) after contrast agent administration, the agent is distributed throughout the tissues and there is no specific binding. At later times (right), the contrast agent has found and become bound to the receptor, and most of the unbound contrast agent has been cleared from the tissues and the circulation. The signal seen at this time comes predominantly from contrast agent that is specifically bound to the target receptors. There is also some signal from contrast agent that is nonspecifically bound to other proteins, and from remaining unbound contrast agent that is still in the circulation. In this figure, the 'target-to-background' ratio for the

contrast agent is 4:1 (12 contrast agent molecules are bound to the targeted receptor, 3 other molecules are present but not bound to the receptor).

Conjugating specific ligands to a cyanine dye is one way to obtain tissue-specific or molecular information with an optical contrast agent. Since many cancers overexpress various receptors, specific ligands can act as a vehicle for selective tumor visualization (66). In this context targeting of extracellular angiogenesis related matrix proteins (oncofetal fibronectin) using dye-labelled single-chain antibodies has been described (131). Other studies have exploited the folate receptor for cancer-specific targeting of fluorochromes (132). More recently, a peptide-dye conjugate consisting of a cyanine dye and the somatostatin (SST) analog octreotate (indotricarbocyanine-octreotate) was synthesized serving as a contrast agent for optical tumor imaging (133,134). The probe showed an accumulation in mouse xenografts detected by an *in vivo* near infrared (NIRF)-reflectance imager with a threefold higher tumor fluorescence compared with non-diseased tissue (133). The targeting conjugate was also specifically internalized by primary human neuroendocrine tumor cells (133). Figure 2.11 depicts fluorescence reflectance images using a conjugate of tricarbocyanine dye and an octapeptide (c.f. Fig. 11a) for targeting the somatostatin receptor in CA20948 tumor-bearing rats (135,136). The tumor cells were implanted subcutaneously in the left flank of the rat demonstrating a marked fluorescence increase compared with surrounding tissues (Fig. 11b, c).

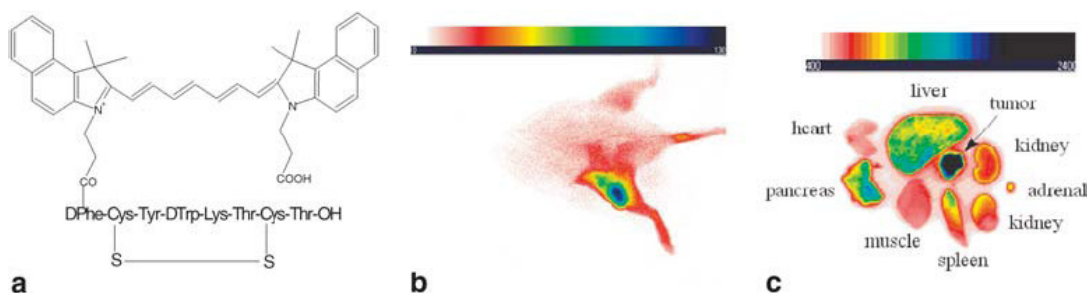


**Figure 2.11** a Molecular structure of cytate, a conjugate of tricarbocyanine dye for near-infrared imaging and an octapeptide for targeting somatostatin receptor which is up-regulated in neuroendocrine tumors. b Fluorescence intensity imaging of a CA20948 tumor-bearing rat 27 h post administration of cytate via the tail vein. Tumor cells were implanted subcutaneously in the left flank of the rat. c Fluorescence-intensity image of selected organ parts excised 24 h post injection of cytate. The somatostatin receptor-positive tumor, CA20948, preferentially retains cytate. (Adapted from 135 and 136)

Similar observations were performed in a separate study (133) that showed significant fluorescence increase from tumor sites compared with normal tissues using the somatostatin analog octreotate coupled to indocarbocyanine dyes. Specifically, the fluorescence detected before the injection of the dye-peptide conjugate administered in a tumor-bearing mouse (RIN38 pancreatic tumor expressing the somatostatin receptor subtype 2) and a control mouse are shown in Figure 2.12a and b, respectively. Figure 2.12c and d show the fluorescence images obtained from the same animals 6 h after probe injection. The administered probe dose was 0.02  $\mu\text{mol/kg}$  body weight. The receptor-binding indotricarbocyanineoctreotate conjugate leads to a significantly elevated tumor signal (Figure 2.12c), whereas a control conjugate with no receptor affinity does not generate contrast (Figure 2.12d).

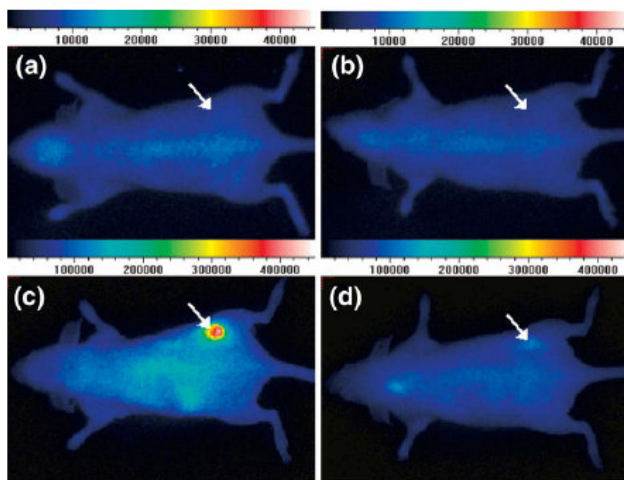


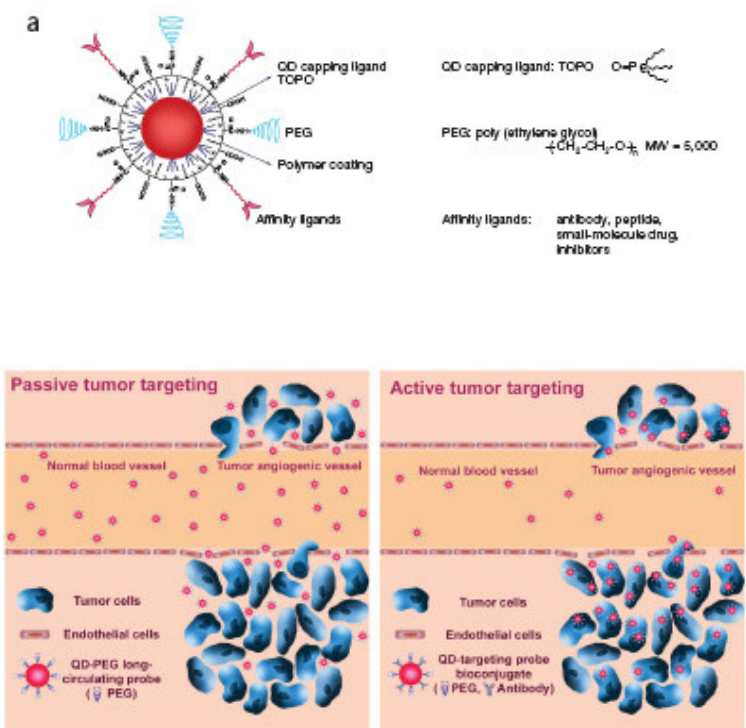
**Figure 2.12** In vivo fluorescence images of tumor-bearing mice (RIN38 pancreatic tumor expressing the somatostatin receptor subtype 2) **a, b** before and **c, d** 6 h after injection of dye-peptide conjugate at a dose of 0.02  $\mu\text{mol/kg}$  body weight. **c** The receptor-binding indotricarbocyanine-octreotate conjugate leads to a significantly elevated tumor signal, whereas **d** a control conjugate with no receptor affinity does not generate contrast.

A different strategy for specification of optical contrast has recently been described by Zaheer and coworkers. They synthesized a fluorescent bisphosphonate derivate (Pam 78) that exhibits rapid and specific binding to hydroxylapatite (HA) in vivo. After intravenous injection, the agent allowed for detection of osteoblastic activity in vivo using a NIRF-reflectance imager (137). This imaging approach might be useful to assess osteoblastic activity in metastatic disease or to study the skeletal development in vivo (137). Using the described receptor or binding affinity approach, high target specificity can be achieved using low amounts of fluorochromes. Nevertheless, this approach operates with a relatively low signal-to-background ratio, since non-bound probes are fully fluorescent and thus contribute to background noise.

## Nanoparticles

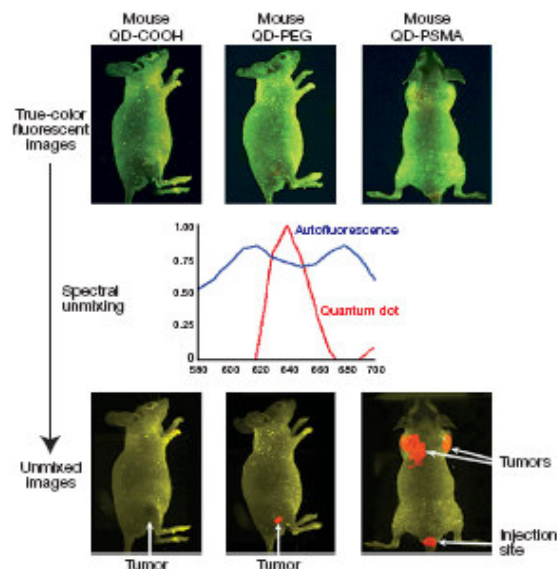
Organic fluorophores have been used in NIR applications for many years. They are typically 1200 or less Daltons in size, varying in toxicity, with widely different biodistribution and pharmacokinetics, and are cleared from the circulation by renal filtration in minutes (138). However, they suffer from problems with controlling their excitation and emission wavelengths, hydrophobia, molecular stability, low quantum yields (efficiency of emission) and are susceptible to photobleaching (loss of fluorescence) which limits their sensitivity to detection (138). Quantum dots have recently been introduced to the field of NIR and have the potential to solve many of the problems associated with organic fluorophores. Quantum dots comprise an inorganic core and shell of metal and an outer organic coating (Figure 2.13). The inorganic core and shell enables tuning of fluorescence with a narrow bandwidth (25–35 nm), thus enabling multi-coloured quantum dots for multiplexed detection of molecular targets (139). In addition, quantum dots are resistant to photobleaching, with an emission time constant (one-half) of approximately 16 min (140), and they have a high quantum yield of close to 90% (141). However, quantum dots are typically large structures of 3–20 nm hydrodynamic diameter,

and hence are difficult to clear from circulation by renal filtration, which results in a high background signal. Also, the issue of *in vivo* toxicity is as yet unknown, and needs to be addressed (140).



**Figure 2.13** Schematic illustration of biconjugated QDs for *in vivo* cancer targeting and imaging. (top) Structure of a multifunctional QD probe, showing the capping ligand TOPO, an encapsulating copolymer layer, tumor-targeting ligands (such as peptides, antibodies or small molecule inhibitors) and polyethylene glycol (PEG). (bottom) Permeation and retention of QD probes via leaky tumor vasculatures (passive targeting) and high affinity binding of QD-antibody conjugates to tumor antigens (active targeting).

Under *in vivo* conditions, QD probes can be delivered to tumors by both passive and active targeting mechanisms (see Figure 2.13, bottom). In the passive mode, macromolecules and nanometer-sized particles accumulate preferentially at tumor sites through an enhanced permeability and retention effect (142-144). This effect is believed to arise from two factors: (i) angiogenic tumors produce vascular endothelial growth factors that hyperpermeabilize the tumor-associated neovasculatures and cause leakage of circulating macromolecules and small particles; and (ii) tumors lack an effective lymphatic drainage system, which leads to macromolecule or nanoparticle accumulation. For active tumor targeting, are used antibody-conjugated QDs to target a prostate-specific membrane antigen (PSMA). Previous research has identified PSMA as a cell surface marker for both prostate epithelial cells and neovascular endothelial cells (145). PSMA has been selected as an attractive target for both imaging and therapeutic intervention of prostate cancer (146).



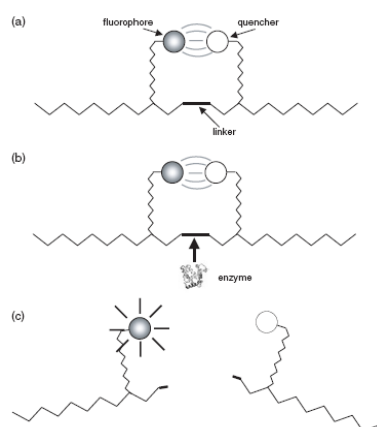
**Figure 2.14** *In vivo* fluorescence images of tumor-bearing mice using QD probes with three different surface modifications: carboxylic acid groups (left), PEG groups (middle) and PEG-PSMA Ab conjugates (right). For each surface modification, a color image (top), two fluorescence spectra from QD and animal skin (middle) and a spectrally resolved image (bottom) were obtained from the live mouse models bearing C4-2 human prostate tumors of similar sizes (0.5–1.0 cm in diameter). The amounts of injected QDs and the lengths of circulation were: 6 nmol and 6 h for the COOH probe; 6 nmol and 24 h for the PEG probe; and 0.4 nmol and 2 h for the PSMA probe. The site of QD injection was observed as a red spot on the mouse tail. The spectral feature at  $\approx 700$  nm (red curve, middle panel) was an artifact caused by mathematical fitting of the original QD spectrum, which has little or no effect on background removal.

Figure 2.14 (147) compares the *in vivo* imaging results from three types of surface modifications: COOH groups, PEG groups and PEG plus PSMA Ab. In agreement with histological examinations, no tumor signals were detected with the COOH probe, only weak tumor signals were observed with the PEG probe (passive targeting) and intense signals were detected in the PEGPSMA Ab conjugated probe (active targeting). This comparison provides further evidence for the conclusion that active tumor targeting by using a tumor-specific ligand is much faster and more efficient than passive targeting based on tumor permeation, uptake and retention.

### 2.4.2.c Activatable fluorochromes

A different means to impart molecular specificity into optical contrast agents is to design activatable probes (148), appropriately engineered fluorochromes that, in the non-activated state, are loaded in closed proximity onto a graft copolymer consisting of a poly-lysine (PL) backbone through appropriate peptides and undergo mutual energy transfer; thus, they exist in a quenched state. At the presence of the targeted enzyme, cleavage of the peptide link releases the fluorochromes (dequenching) which results in a bright fluorescence signal, up to several hundredfold increase, which can be detected *in vivo* (Figure 2.15) (1).

Multiple enzymes, especially proteases<sup>5</sup>, are involved in a whole variety of pathologies ranging from carcinogenesis to immune diseases (149). In 1999 an autoquenched fluorescent probe was developed, which is converted from a non-fluorescence to fluorescence state by proteolytic activation (148). The first generation of this type of molecular contrast agent consisted of a long circulating macromolecular carrier molecule (poly-lysine backbone) shielded by multiple methoxy-polyethylene-glycol sidechains (PLL-MPEG). Multiple cyanine dyes (Cy 5.5; excitation maximum: 675 nm; emission maximum: 694 nm) are loaded onto this carrier molecule resulting in a fluorescence signal quench due to fluorescence resonance energy transfer (FRET) among the fluorochromes (overlapping excitation and emission spectra) (148). This first generation of protease-sensing optical probes is activated by lysosomal cystein or serin proteases such as cathepsin-B (148). By linking the fluorochromes via a peptide spacer to the carrier molecule (second-generation probe) the probe selectivity can be tailored to other enzymes such as matrix-metalloproteinase- 2, cathepsin-D, or thrombin (148-154).



**Figure 2.15** Example of an activatable optical contrast agent. The contrast agent is built on a backbone and consists of a linker that can be cleaved by a specific enzyme of interest and a fluorophore and quencher molecule that are on either side of the linker and in close proximity with one another. When the linker is intact (a), and the fluorophore is excited by an external laser, the energy is efficiently transferred to the quencher molecule and very little is emitted as light. If the contrast agent molecule encounters the enzyme of interest (b) and that enzyme cleaves the linker (c), the quenching molecule moves away from the fluorophore and now the excitation of the fluorophore leads to the emission of light. The signal is therefore switched on by the presence of the specific enzyme.

Cathepsin B is a lysosomal cysteine protease involved in cellular protein turnover and degradation (155, 156). It is overexpressed in many tumors as well as overexpressed by host cells associated with tumors. It has been implicated in tumor progression: both metastases formation (157,158) and *in vitro* growth (159-161) decrease in the presence of cathepsin B inhibitors. Several studies (162-165) have demonstrated that high levels of cathepsin B expression correlate with aggressive tumor behavior. High levels of cathepsin B expression also correlate inversely with patient survival (164-167). Given cathepsin B's close relationship with early cancers and metastasis with resultant host response, the first optical probes constructed for targeting protease activity were specific for cathepsin B

<sup>5</sup> Proteases: enzymes that catalyze the proteins hydrolysis.

(168-169). Figure 2.16 shows how a breast cancer implanted in a nude mouse is revealed with cathepsin B imaging (163). The time for imaging after probe administration may be as short as 2 h, depending upon the location of the enzyme being imaged (170); optimal timing after injection depends as well upon the disease imaged (171, 172). Image acquisition times on newer systems are in the subsecond time frame, allowing real-time visualization of fluorescent anatomical detail. The bright fluorescence, as this example shows, helps locate this micrometastasis-sized tumor, based upon its cathepsin B activity.

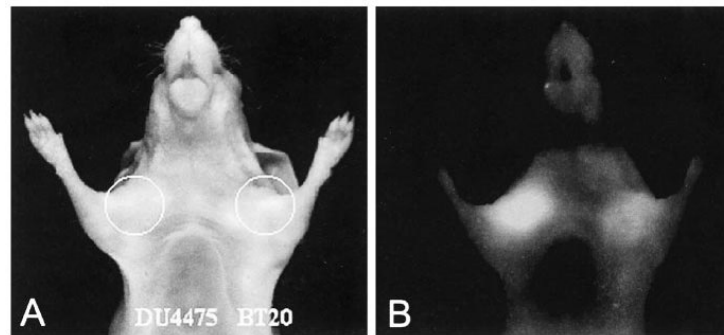


**Figure 2.16** Aggressiveness of breast cancer revealed with cathepsin B imaging. An aggressive (*left*) and well-differentiated (*right*) breast tumor implanted in a nude mouse have different fluorescent signal intensities correlating with their invasive and metastatic potential (from Ref. 25).

A probe specific for cathepsin D has also been synthesized and tested in mouse models (56-57). The main function of cathepsin D is in protein catabolism; however, a 2-50-fold increase in enzyme levels has been reported in breast cancers (173-174), and overexpression has been associated with higher metastatic potential (175). Imaging of cathepsin D was analogous to cathepsin B imaging in Figure 2.17. However, these studies additionally demonstrated that it was possible to selectively image tumors based on a difference of a single gene expression.

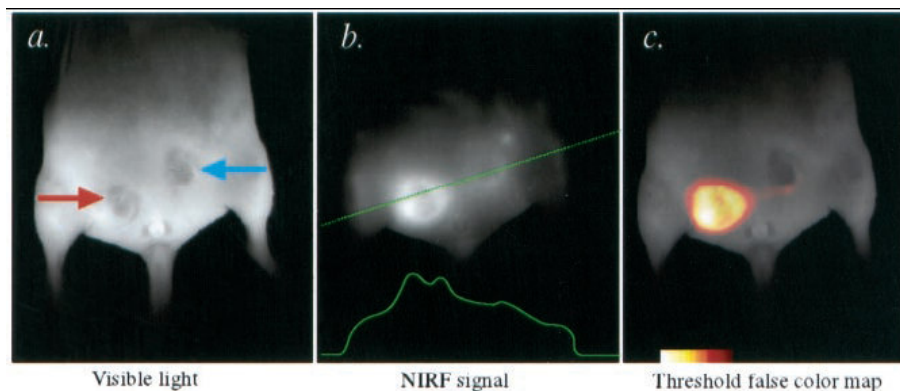


**Figure 2.17** Representative optical images of the lower abdomen of a nude mouse implanted with a CaD1 (*red arrow*) and CaD2 (*blue arrow*) tumor. *a*, white light image 24 h after i.v. injection of the reporter probe. *b*, identical imaging set-up as in *a*, except that NIRF fluorescence is shown at 700 nm. Note that the CaD1 tumor emits fluorescence, whereas the CaD2 tumor has a significantly lower signal. The *dotted green line* represents the line for the density slice profile shown at the bottom. *c*, superimposed images from *a* and *b*, with CaD information shown as a thresholded false color map.

### Imaging MMP-2 and Its Inhibition

MMPs (176) similar to the cathepsins detailed above, are proteases overexpressed in many cancers. The level of MMP expression has been shown to be related to tumor stage (177) and metastasis (178). Among the subtypes, MMP-2 (gelatinase) has been identified as one of the key MMPs. Numerous clinical studies show a clear correlation between MMP-2 expression and poor outcome of disease (179-182). A number of MMP inhibitors, some of which advanced to Phase III clinical trials, have been developed (183-185). A characteristic example of this technology applied to elucidate different expression levels of tumor MMP-2 activity is shown in Figure 2.18 using an MMP-2-positive human HT1080 fibrosarcoma and an MMP-2-negative BT20 mammary adenocarcinoma (153).

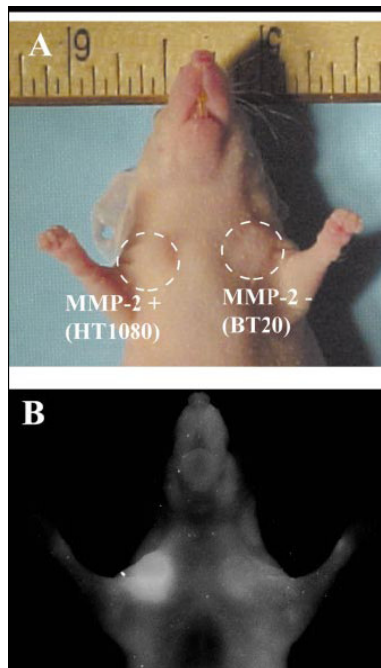


**Figure 2.18** . NIRF imaging of a nude mouse implanted with both an MMP-2-positive human HT1080 fibrosarcoma and an MMP-2-negative BT20 mammary adenocarcinoma. Top: Both tumors measured approximately 2 3 3 mm. Bottom: Raw NIRF image shows that the fibrosarcoma generated strong fluorescent signal intensity 2 hours after intravenous injection of the MMP-2-sensitive probe, but the signal intensity of the BT20 tumor was only slightly higher compared with the background fluorescence of the skin. Quantitative analysis revealed a significant difference between the fluorescent signal intensity in BT20 tumor and that in HT1080 tumor.

Given its importance in tumor pathology, a MMP-2-selective probe was constructed. Imaging of MMP-2 activity was demonstrated, starting 2 h after probe administration (171, 153). Most importantly, a series of experiments showed in parallel cohorts of mice that fluorescent signal intensity after MMP-2 probe administration significantly decreased in tumors from animals that were pretreated with a MMP-2 inhibitor compared with controls. Thus, essentially realtime protease inhibition may be imaged noninvasively, instead of waiting several months to evaluate anatomical response, as is traditionally done in individual patients, as well as in *in vivo* animal trials of inhibitor therapy. Such imaging has implications for faster, more accurate titration of inhibitor

dosing in human drug trials, as well as potentially routine care in the future for individual patients.

#### 2.4.2.d Fluorescent protein

Green fluorescent proteins are native to a few marine organisms, but can be introduced into the cells of other organisms by gene transfer. These transferred GFPs act as a chemical fluorescent contrast agent for protein activity inside the cell 186. Unlike NIR fluorescent imaging, GFP imaging does not use exogenous fluorochromes. The original GFP was cloned from the bioluminescent *Aequorea victoria* jelly fish<sup>6</sup> 187, and had an absorption and excitation wavelengths in the green part of the spectrum from 489 to 508 nm, respectively. FP expression is based on emission of visible photons at specific wavelengths based on energy-dependent reactions catalyzed by luciferases, whose gene have been cloned from a large number of organisms, including bacteria, firefly (*Photinus pyralis*), coral (*Renilla*), jellyfish (*Aequorea*), and dinoflagellates (*Gonyaulax*). Sensitive imaging systems have been built to detect quantitatively a small number of cells or organisms expressing luciferase as a transgene (188).

Fluorescent proteins offer another possibility for extracting molecular information in small animals but have a less defined role in clinical applications. A drawback of GFP is its low emission wavelength (□510 nm), which overlaps with the autofluorescence of many tissues. This is one of the reasons that mutants of GFP with redshifted emission have been engineered. A new red fluorescent protein (DsRed) that emits fluorescence at 583 nm has been isolated from tropical *Discosoma* corals (189). Another red fluorescent protein that is potentially even more suitable for *in vivo* imaging is HcRed, generated by site-directed and random mutagenesis of a nonfluorescent chromoprotein isolated from the reef coral *Heteractis crispa*, which emits light at 618 nm (190,191). Unlike bioluminescent proteins (discussed below), fluorescent proteins do not require cofactors or chemical staining before *in vivo* imaging. The ability to quantify fluorescence accurately and repeatedly will be essential in different biological applications. Currently one of the main imaging applications of fluorescent proteins is in monitoring tumor growth (192,193) (Figure 2.19) and metastasis formation (194,195) (Figure 2.20) as well as occasionally gene expression (196) (Figure 2.21). Fluorescent proteins have also been used as reporters to image gene promoter activity (197). Because hemoglobin is an efficient light absorber, GFP-expressing tumors have been used to image angiogenesis, as vessels are contrasted against fluorescent tumor background (198) (Figure 2.22).

---

<sup>6</sup> The green fluorescent protein is found in the jellyfish, *Aequora Victoria*, that contains a bioluminescent protein -aequorin- that emits blue light. The green fluorescent protein converts this light to green light, which is what we actually see when the jellyfish lights up.

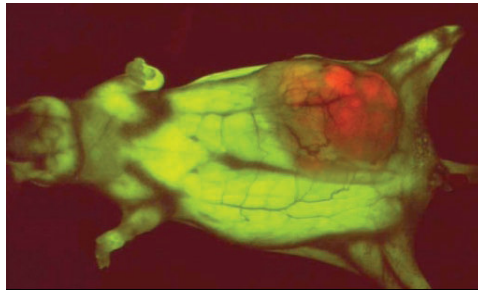


**Figure 2.19** Whole-body image of orthotopically growing HCT 116-RFP human colon cancer in GFP nude mouse. Image was acquired in a fluorescence light box with a CCD camera 10 weeks after orthotopic implantation of HCT116-RFP cells.

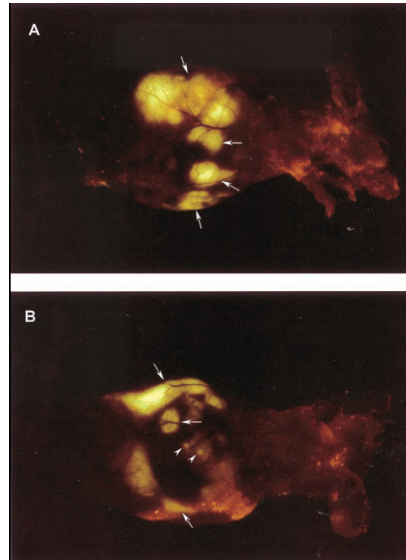


**Figure 2.20** External images of B16F0-GFP colonizing the liver. A metastatic lesion of B16F0-GFP in the liver growing at a depth of 0.8 mm after portal vein injection was externally imaged through the abdominal wall of the intact nude mouse. (A) An external image of multilobe liver metastases of the B16F0-GFP cells (large arrows). (B) An external image of small liver metastatic lesions of approximately 1.5 mm in diameter (small arrows) and other larger metastatic lesions (large arrows).

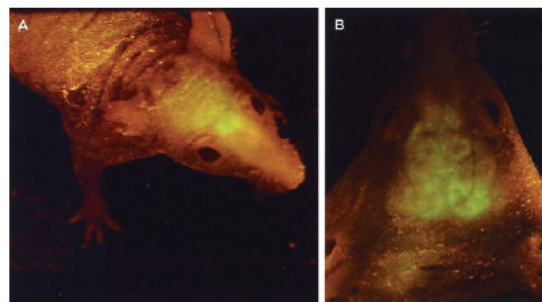


**Figure 2.21** External whole-body image of vAd-GFP gene expression in the brain. An external image of vAd-GFP gene expression in the brain acquired from a nude mouse in the light box 24 h after gene delivery. Clear image of transgene expression in the brain can be visualized through the scalp and skull.

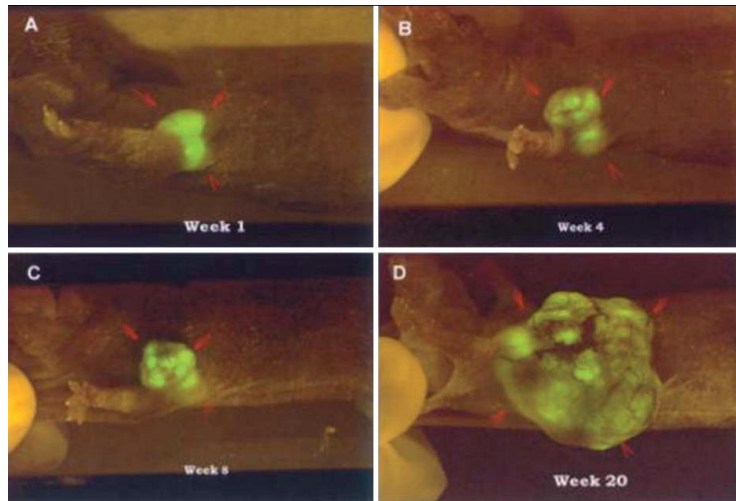


**Figure 2.22** : Time course of whole-body fluorescence imaging of MDA-MB-435-GFP human breast cancer angiogenesis in orthotopic primary tumor. The GFP expressing human tumor was transplanted by SOI in the fat pad of nude mice and whole-body imaged. (A) Week 1. (B) Week 4. (C) Week 8. (D) Week 20. (E) Quantitative graph of microvessel density as a function of time.

### 2.4.2.e Bioluminescence

Bioluminescence imaging is used to detect the photons that emanate from cells that have been genetically engineered to express luciferases. Luciferases comprise a family of photoproteins, isolated from a variety of species, which modify their substrate, called luciferin, causing the release of a photon. Firefly luciferin (a benzothiazole) and *P. pyralis* luciferase are the most commonly used substrate-enzyme pairs for *in vivo* imaging (199-202) because of their high wavelength and quantum yield. In the firefly, luciferase utilizes energy from ATP to convert its substrate luciferin to oxyluciferin, with the emission of a detectable photon. The names 'luciferin' and 'luciferase' are generic terms for the active agents (substrate and enzyme, respectively) in bioluminescent organisms. Numerous examples of bioluminescence exist in nature, most notably the flashes of light emitted by the male firefly (*Photinus pyralis*). Other examples include light emission by various marine organisms such as sponges, corals, jellyfish, clams and a few types of fish. More recently, imaging using *Renilla reniformis* luciferin and coelenterazine in mice has also been reported (203). Firefly luciferin normally produces light at 562 nm, although a number of genetically engineered luciferases from the firefly have been created, resulting in spectral shifts of released light photons. Luciferase can be transgenically expressed in mammalian cells, and when exposed to substrate, releases photons that can be detected and quantified using lowlight photon-counting cameras. Using sensitive filters, these mutants can be used to track more than one protein, similar to what has been done with blue- and red-shifted GFP.

Bioluminescence imaging has emerged as a useful and complementary experimental imaging technique for small animals. Because of its simplicity and ease of generating *luc/lux* cells, its primary uses have been for tracking tumor cells, stem cells, immune cells and bacteria as well as for imaging gene expression. In contrast to fluorescence techniques, there is no inherent background with bioluminescence, which makes this technique highly sensitive. The main limitation has been that the method currently does not allow absolute quantification of target signal. Rather, its primary uses

are either in binary mode (yes/no *luc* expression) or as an imaging tool to follow the same animal under identical conditions, including positioning. The imaging signal also depends on ATP, O<sub>2</sub>, depth and the presence of excess substrate, which is administered exogenously. Typical doses of luciferin are in large excess (120 mg/kg i.p.) and are injected immediately before data acquisition with photon-counting cameras. Image acquisition times are on the order of minutes, depending on expression levels, depth and photon flux. One of the principal uses of luciferase imaging has been to track cells, in particular dividing cells such as tumor cells (199,204), progenitor and stem cells (Figure 2.23), immune cells (205) and bacterial cells (206). Thus, for example, *luc*-expressing stem cells can be seen crossing the cerebral hemispheres in a tumor model (Figure 2.23a), and peritoneal proliferation of ovarian cancers can be monitored over time (Figure 2.23b). Estimates from subcutaneous implantations indicate that between 10<sup>3</sup> and 10<sup>4</sup> *luc* cells can be detected at this location. Another important application has been to use *luc* as a transgene in experimental gene transfer studies (207-209), as a screening tool for rapid identification of transgenic founder mice (210) or to visualize activation of specific pathways in cancer formation (211). Most recently, engineered luciferases have been used to image specific cellular processes. In one study, the estrogen receptor domain was fused through a caspase-3-cleavable site to both ends of luciferase to image apoptosis *in vivo* (B. Ross, personal communication). In experimental studies, bioluminescence has been used to image protein-protein interactions (212) and NF-κB degradation (213). It is likely that the imaging applications of luciferase will continue to expand rapidly with the use of engineered luciferases, activatable luciferins and bioluminescence resonance energy transfer (BRET) strategies.

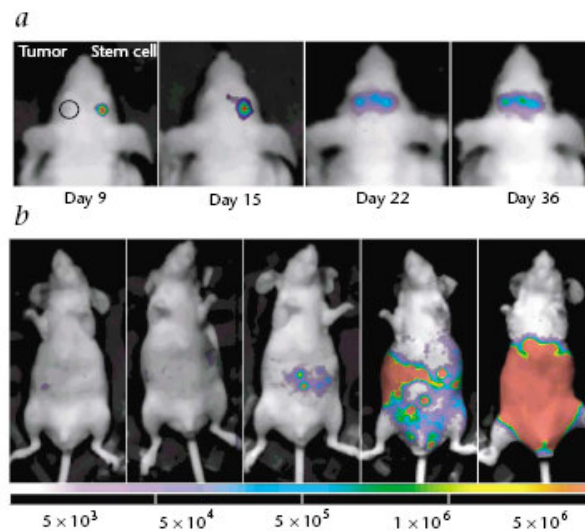


**Figure 2.23** Bioluminescence imaging. Two examples of imaging with bioluminescence. *a*, Migration of *luc*-labeled neural progenitor cells (C17.2, obtained from E. Snyder) across the brain midline attracted by a contralaterally implanted glioma. *b*, *Luc*-labeled OVCAR-8 ovarian cancer cells implanted into the peritoneal cavity at different densities. Note that there is a faint focus of signal even with 5 10<sup>3</sup> implanted cells.

### 2.4.3 *Advantages and drawbacks*

Encouraging results have already been obtained for use of optical techniques for *in situ* monitoring of tissue parameters, discrimination of diseased tissue from normal, mammography, and several therapeutic applications. Despite advances in medical imaging technologies over the past two decades, we are currently still limited in our ability to detect tumors or other diseases in their earliest stage of formation, phenotype tumors during complex cycles of growth, invasion and metastases, to use imaging techniques to speed up drug testing, and to use imaging as an objective endpoint for tailoring therapies in a given individual.

Reflectance imaging is an ideal tool for high-throughput imaging and screening of surface fluorescent events *in vivo* or in excised tissues. It offers simplicity of operation and high sensitivity for molecular events that are close to the surface. Typical acquisition times range from a few seconds to a few minutes. For laboratory settings, multiple animals can be simultaneously imaged. Hardware development and implementation is also straightforward and relatively inexpensive. Reflectance systems do not use ionizing radiation, employ safe laser powers, can be made portable and attain small space requirements to be ideal for the laboratory bench. These features can allow easy laboratory and bench-top use and enable monitoring of molecular events repeatedly and over time. The combination of molecular beacons and optical imaging technologies is expected to play a fundamental role in biomedicine in the next decade and continued developments in probe design and imaging technologies will undoubtedly further expand current capabilities.

On the other hand, reflectance imaging has fundamental limitations both as a research or clinical tool. Firstly, the technique attains only small penetration depths (a few millimeters). This is because the appearance of deeper lesions is significantly blurred and the signal detected from them is significantly attenuated as a function of lesion depth while the background noise remains constant in reflectance mode since it consists of fluorescence signals from superficial layers and intrinsic light contaminating the fluorescence measurement due to imperfect filtering. This is in contrast to tomographic methods where both signal and noise reduces so that signal to noise remains significant for lesions that are much deeper than a few millimeters. Secondly, reflectance imaging is not capable of quantification: a small structure of high fluorochrome concentration that is deeper into tissue could yield the same appearance on the surface as a larger structure of low fluorochrome concentration that is closer to the surface. This is due to the nature of propagation of diffuse photon density waves into tissue. The photon count reading at a surface of an animal due to a lesion on or under the surface depends on the lesion depth, the lesion volume and the optical properties of both the lesion and the surrounding tissue; therefore, images from different animals, or from the same animal at different time points, are generally insufficient for yielding quantitative insights. Further, one of the major rate-limiting steps is the development of well designed and carefully validated contrast agents that are selective for major molecular pathways implicated in disease. Attracting talented chemists and creating appropriate training programs to increase the pool of available chemists that are interested in developing imaging agents should also be a priority. Finally, notwithstanding the tremendous promise of these techniques, the translation of molecular imaging methodology into the clinic, and its role in the diagnosis and staging of disease, and the monitoring of therapy, is yet to be defined and demonstrated. There is a

need to improve imaging performance, either increasing spatial or temporal resolution, sensitivity, or commonly both. The ability to accurately quantify molecular imaging studies is of great importance when these tools are used to track disease and the effects of interventions. There also has been little characterization of the quantitative accuracy or reproducibility of imaging methods, nor a careful statistical analysis of to what degree longitudinal molecular imaging studies provide an advantage over generally more accurate, but usually much more invasive, methods and techniques. In all these areas, and many more, there are opportunities for biomedical physicists to make significant and important contributions which will help build the solid foundation required for the future anticipated growth of molecular imaging science.

## 2.5 *Conclusions*

The fluorescence is the third fundamental phenomenon, after absorption and scattering, that interests the interaction light-biological tissue. Hence, it is naturally born a family of fluorescence imaging techniques, FRI, different relatively to the fluorescence labelling strategy, but about identical relatively to the experimental implementation. The FRI technique, as well as optical, is non invasive and the fluorescent marker are generally not toxic. The experimental apparatus is simple, inexpensive, generally compact and easy to use. Set the experimental apparatus, it is possible study different biological target exploiting the most adapt strategy labelling: tumor diagnosis can be performed by a non specific fluorophore, as cyanine or porphyrin, while molecular pathway studies use fluorophores of high specificity, targeted or “smart”, or fluorescent protein expressed by only the cells transfected with the FP gene. The FRI technique allows for monitoring in vivo tumor growth, detection of metastasis formation and dissemination, gene expression, apoptosis, angiogenesis, inflammatory diseases. However, the analysis in vivo is limited to penetration depth of few centimetres in the range spectral of NIR, so that the applicability to clinic of FRI techniques is a challenge. The absence of quantitative determinations is another important limit. So the FRI principal applications are the studies in vivo on small animals, that represent today a research field rich and very important because of the possibility of study in mice human diseases and transfer these knowledges to humans.

# Chapter 3

## *HP-FRI in vivo on small animals: preliminary measurements*

### *3.1 Introduction*

In this chapter and in the successive it will be showed the way of our experimental work to obtain the final aim: detection of subcutaneous solid in early stage tumors *in vivo* on small animals through HP mediated FRI. Hence, the biological target is the early detection: it is crucial, indeed, in the tumor diagnostic to be able to detect the tumor formation, since earlier diagnosis greater the patient survival probability, especially if the tumor is highly invasive.

Before we reach this research stage, it is been necessary to carry out a preliminary work studying the HP water solution fluorescence spectrum at different concentration; evaluating the more efficient HP injection modality in mouse by FRI and spectrofluorimetric measurements; verifying the resistance of HP compound to photobleaching; estimating the HP accumulation in different tissue types both tumor and healthy by spectrofluorimetric measurements on histological sections of mice tissue.

Then, in a first part of the work, the *in vivo* FRI measurements were performed combining the *in vivo* fluorescence image of the tumor region on the mouse with a fluorescence image of a healthy region on the same mouse to perform a digital subtraction of the last image from the first. This simple operation, reducing the autofluorescence and the HP background fluorescence contribute, enhances the contrast of the tumor region. It was so possible to reveal an increased fluorescence emission in tumor region with respect to healthy region with different tumor types and to correlate this feature to the tumor malignancy degree.

Furthermore, we present the results obtained by imaging *in vivo* mice surface solid tumor bearing with simultaneous acquisitions in two modalities: our HP-FRI and a radionuclide imaging based on a semiconductor pixel detector of the Medipix family at high spatial resolution. With this combined system we investigated the detectability of two different types of tumor, having different malignancy degree.

In a second part of the work it is been employed a new CCD camera with high sensitivity and low noise that, combining with the HP features, allows for a new imaging modality and more advanced results, as just early tumor detection. This last part is deferred to the next chapter.

### *3.2 Experimental set-up.*

#### *3.2.1 HP-FRI measurements*

In the preliminary and first part of the work the experimental apparatus (Figure 3.1) for FRI measurements was composed by:

- Excitation source, a frequency doubled mode-locked active-passive Nd:YAG laser ( $\lambda = 532$  nm, beam diameter = 7 mm, energy/pulse = 30 mJ, pulse width = 50 ps, repetition rate = 10 Hz);
- Optics for the collection of the excitation radiation on the sample (neutral filter, reducing the excitation intensity to avoid that intensity too high reaches the CCD camera in the excitation image registration, collimation lens, matching the excitation beam section to the tumour area, and mirror, reflecting the laser beam onto the mouse);
- sample, a tumor bearing or healthy anesthetized mouse;
- emission filter, a cut-on long wave pass filter (Andover 600FH90-25, cut-on wavelength: 600 nm). This filter allows HP fluorescence radiation (whose spectrum extends beyond 600 nm) to be recorded and backscattered radiation at 532 nm to be rejected.
- an analogue CCD camera (Hamamatsu C3077-71S, 560x575 pixels, sensitivity = 0.3 lux) equipped with a Computar objective of 16 mm focal length;
- image acquisition (average of 32 single frame consecutive acquisitions) and analysis board, Hamamatsu Lepas 11 system (10 bit ADC).

During the FRI measurements, the whole apparatus was closed by dark panels to avoid the penetration of spurious light in the CCD camera.

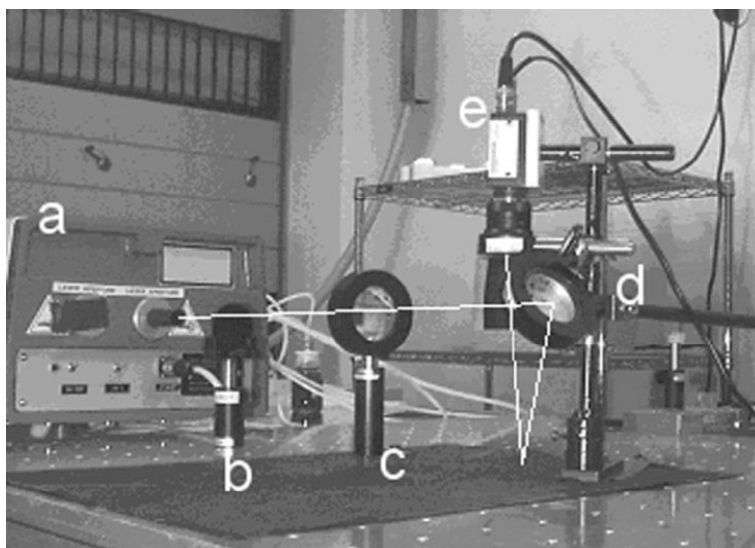


**Figure 3.1** View of the experimental setup used in the preliminary measurements and in the first part of the FRI measurements. From left to right: (a) the laser head; (b) the neutral filter; (c) the collimation lens; (d) the mirror; (e) the CCD camera with cut-on filter. Also drawn is the optical ray path from the source to the camera, when the animal is placed on the table top.

Moreover, was used also a spectrofluorometer (Perkin Elmer LS50) computer controlled to obtain fluorescence spectra of histological sections of mice tissues.

We observe explicitly that, although the main absorption band of HP compound is localized in the UV region, at about 405 nm (Figure 3.2), nevertheless we prefer exploit a secondary absorption band centred at about 530 nm exciting it with the Nd:YAG second

harmonic light at 532 nm, since, as explained in the Chapter 1, the penetration depth is higher and the autofluorescence emission is lower at higher excitation (and fluorescence emission) wavelength.

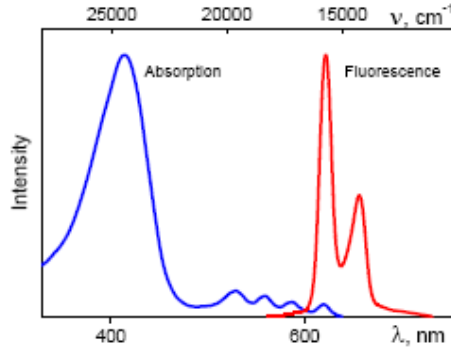


**Figure 3.2** A typical Hp compound absorption and fluorescence emission spectra. The maximum absorption band is centered at about 405 nm, while a secondary absorption band is at about 530 nm. The typical fluorescence peaks at 620 nm and 680 nm are also showed.

The analog CCD camera operates at 25 frames per second with internal trigger and is inactive only for 10  $\mu$ s (blanking time) per frame. Then, the CCD image acquisition is not triggered by the trigger signal available at each laser shot, and some camera frames may correspond to a no-irradiation period and are not useful for analysis. Anyway, given the laser repetition frequency and the rapid fluorescence decay of the fluorophore (10–20 ns half-life), we consider that by grabbing 32 consecutive camera frames the number of useful frames included is always the same. Then, the final image is the accumulation of those 32 single frame consecutive acquisitions.

In the Appendix at the end of this chapter is presented a brief overview of the features of the CCD camera, because of the key role played by this instrument in FRI measurements.

### 3.2.2 FRI/Gamma combined imaging

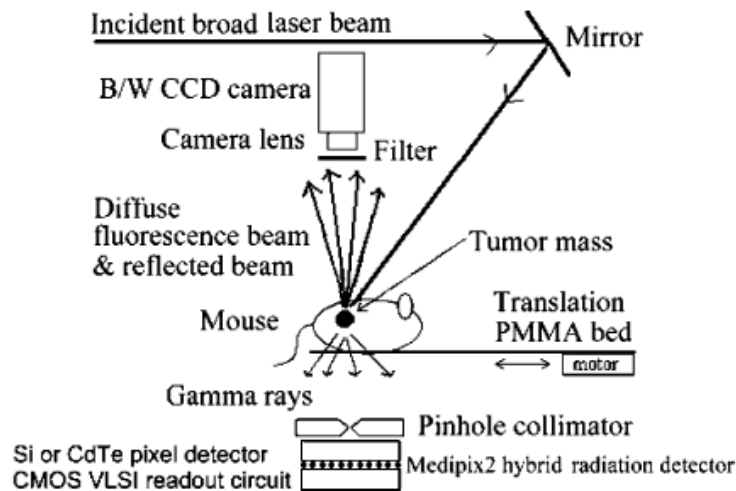


**Figure 3.3** Schematic view of the experimental combined (fluorescence, radionuclide) imaging system.

The experimental setup for combined fluorescence and radionuclide imaging is shown in Figure 3.3. The radionuclide imaging set-up, combined with our FRI set up described in the previous paragraph, uses as gamma radiation detector two hybrid detectors based on the Medipix2 read-out circuit (214), which features 256x256 pixels with 55- $\mu\text{m}$  pitch, for a total sensitive area of 14x14 mm<sup>2</sup>. The Medipix2 chip is interfaced serially (215) to a PC, running the Medisoft 4 software (216). One hybrid detector is obtained by bump-bonding Medipix2 to a 300- $\mu\text{m}$  thick silicon pixel detector, the second one by bump-bonding Medipix2 to a 1-mm thick CdTe pixel detector (217). The silicon detector was reverse biased at 80 V, the CdTe detector was biased at 100 V. At 140 keV, the silicon detector has only about 1% quantum efficiency, while the 1-mm CdTe detector has quantum efficiency greater than 30%. For gamma-ray imaging, we have used 90 knife-edge pinhole collimators made of pure tungsten with 0.78-mm diameter (7-mm thick) or 1.0-mm diameter (4-mm thick), respectively.

### 3.3 Materials and methods.

In the next paragraphs we describe the steps that have preceded the FRI measurements *in vivo*.

#### a. HP solutions fluorescence spectroscopy

The HP solution for fluorescence tumor labeling in mice *in vivo* was obtained by dissolving 4.448 mg of powder of hematoporphyrin dichlorohydrate (Vit-porphyrin II, Teofarma, Italy), corresponding to 4 mg HP, in 2 ml distilled water. HP dichlorohydrate water solutions emission fluorescence spectra at higher dilution with respect to the solution injected in mice (1:2, 1:4, 1:8, 1:16, 1:32) were measured with spectrofluorometer. In these measurements the excitation wavelength was 532 nm, the scanning velocity 120 nm/min and the spectral resolution 5 nm. The wavelength scanning range is 550–800 nm and the scan step is 0.5 nm. Moreover, we also checked the stability of the spectra of the solutions, repeating the spectroscopic measurements on HP water solutions 24 h after they have been kept at room temperature. Finally, in order to check the HP photobleaching resistance, we exposed to the same laser light dose administered to mice during the fluorescence measurements Petri dishes containing the HP solutions at different concentrations and we recorded the emission spectra of the solutions before and after irradiation.

#### b. HP injection modality in mice

In all the measurements *in vivo* we used six-week-old Crl:CD-1 athymic nude mice (Charles River Laboratories, Calco, Italy) of about 20 g of body weight. These studies were conducted in accordance with the Italian regulation for experimentation on animals. All *in*

*in vivo* experiments were carried out with ethical committee approval and met the standards required by the United Kingdom Co-ordinating Committee on Cancer Research (UKCCCR) guidelines (available at [www.ctu.mrc.ac.uk](http://www.ctu.mrc.ac.uk)). No mice showed signs of wasting or other signs of toxicity.

Healthy mice were injected subcutaneously (*sc*) (two mice), or intraperitoneally (*ip*) (two mice), or intramuscularly (*im*) (one mouse), with 200  $\mu$ l of the above solution, corresponding to a dose of approximately 7 mg HP/kg mouse body weight. A not injected mouse was used as a control. Fluorescence measurements on healthy *sc* and *ip* injected mice were performed, respectively, 3, 6, and 24 h after HP administration and after 3 h only for *im* injected mice. Ten minutes before the measurements the mice were anesthetized by the injection of 100-110  $\mu$ l of a solution of chloral hydrate 10 mg/ml in NaCl 0.9%.

### c. HP-FRI *in vivo*

In the first HP-FRI measurement, the tumor cells are the ARO tumor cell line, derived from anaplastic human thyroid carcinoma cells. This is a tumor poorly differentiated and, therefore, with high degree of malignancy. Tumor in mouse was obtained by injecting  $5 \times 10^6$  ARO cells in the mouse back and the fluorescence measurements were performed 6 and 24 h after HP administration. Mouse was injected in a leg muscle with HP solution at the same dose as the healthy ones (7 mg HP/kg mouse body weight). This mouse will be called mouse #0.

In the successive FRI-HP measurements, tumor cells are derived by two human thyroid tumors with different degree of malignancy. Besides the ARO cell line, was considered also the NPA tumor cell line, derived from papillary human thyroid carcinoma cells. The ARO cells are much more malignant with respect to the NPA cells. Cells were cultured in DMEM culture medium supplemented with 10% fetal calf serum, penicillin (50 U/ml) and streptomycin (50  $\mu$ g/ml).

ARO or NPA cells ( $\sim 3.5 \times 10^6$  cells/mouse) were inoculated into the right dorsal portion or paw of mice. Measurements on tumor bearing mice are performed approximately ten days after cell inoculation, when the tumor mass achieved the volume of about 50 mm<sup>3</sup> (NPA tumors) and 400 mm<sup>3</sup> (ARO tumors) and 6 h after HP administration.

We have imaged 10 ARO tumor bearing mice and 9 NPA tumor bearing mice. These mice will be called numbering them from 1 to 10 for those ARO tumor bearing and from 1 to 9 for those NPA tumor bearing.

Furthermore, an ARO tumor histological section (mouse #9) was imaged by FRI to analyze the HP spatial distribution in all the points of the tumor region and in the region surrounding the tumor.

In our HP-FRI measurement protocol the following sequence of optical images was acquired:

- image of laser beam 2-D profile at 532 nm (with neutral filter on the laser way);
- black and white (b/w) image of the mouse acquired under white light illumination and without emission filter;
- fluorescence image of the mouse.

The average image of the 2-D laser beam profile was integrated to supply a reference value to take into account possible intensity fluctuations of the laser beam in different sets of measurements. The average fluorescence image was divided by the mean beam intensity during each set of measurements.

#### *d. Fluorescence spectroscopy*

At the end of the fluorescence imaging measurements, some healthy and tumor bearing mice were sacrificed and tissue biopsies were taken and kept at low temperature (20 °C) to study their fluorescence spectra. The examined samples were:

- frozen skin samples for control and *im* injected healthy mouse;
- frozen skin samples for *sc* and *ip* injected healthy mouse;
- frozen histological sections (thickness 30 μm) of mouse muscle for control and *im* injected healthy mouse;
- frozen samples of ARO tumor and healthy tissues of the tumor bearing mouse #0;
- histological sections from the healthy muscle and tumor tissues of three of the ten ARO-bearing and three of the nine NPA-bearing mice, sacrificed immediately after the fluorescence imaging measurements.

In these measurements the excitation wavelength was 532 nm, the scanning velocity 120 nm/min and the spectral resolution 5 nm. The wavelength scanning range is 550–850 nm and the scan step is 0.5 nm. Measurements of frozen tissue samples were performed so quickly that they did remain frozen. After measurements the frozen samples were added with one or two drops of a solution of PBS and glycerol (1 : 10) and then saved at 4 °C. The stability of the spectra following sample fixation with formalin and saving at 4 °C was also investigated. Since the addition of glycerol may change significantly their optical properties, these samples were not anymore used for spectroscopic measurements.

#### *e. Combined imaging*

The mice imaged with combined system were an ARO tumor bearing mouse and a NPA tumor bearing mouse. Once anaesthetized (like explained in paragraph 3.3 c), the mice were put horizontally in the imaging field (Figure 3.3). The fluorescence image provides a top view of the HP injected 6 h before concentration in the subcutaneous tumor area, and the bottom view taken with the hybrid pixel detector gives the scintigraphic image of the tumor area using <sup>99m</sup>Tc MIBI injected (74 MBq) about 2 h beforehand.

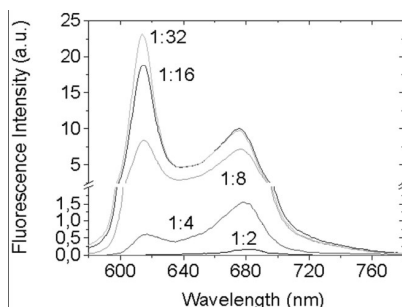
To obtain a control measurement for radionuclide emission, immediately after the combined imaging the mice were imaged by a commercial gamma camera. Finally, tissue autoradiography was performed on fresh tumor tissue histological sections.

### *3.4 Results and their discussion*

#### *a. Preliminary tests*

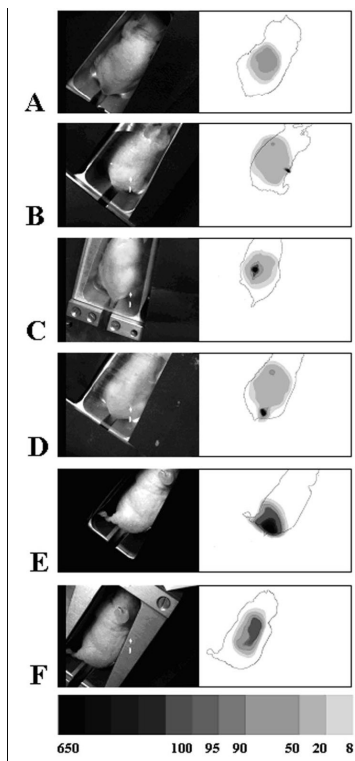
Figure 3.4 shows fluorescence spectra of water solution of HP for different concentration values. These spectra exhibit the well known emission peaks around 610 and at 680 nm. Both peaks decrease in intensity with increasing HP concentration, the peak at 610 nm decreasing more rapidly than that one at 680 nm, so that they have the same height at a

dilution ratio 1 : 8. The HP concentration dependence leading to the disappearance of the peak at 610 nm can be ascribed to the aggregation state of the HP molecules, which strongly affects both their fluorescence quantum yield and lifetime (218). We recall that the HP compounds shows also a secondary absorption band centered at about 630 nm (Figure 3.2), that at least partially reabsorb the fluorescence emission of the peak at 610 nm, especially in the tissue, where the emission peaks are shifted toward longer wavelengths (Figure 3.7).



**Figure 3.4.** Fluorescence spectra of water solution of HP for different values of dilution. The starting solution is that one we injected in mice (HP concentration = 0.7 mg/ml).

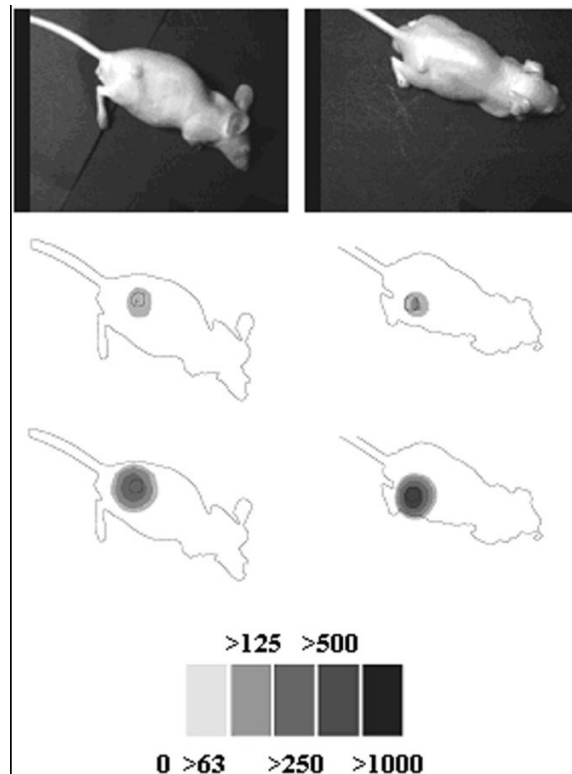
These spectra do not change both upon long lasting exposure to light at 532 nm or after sample keeping at room temperature: the HP chemical stability is high and photobleaching is negligible.



**Figure 3.5** For each treatment condition (A-F) the anesthetized mouse, contained in the metal holder, is imaged optically (left column images) and correspondingly via its fluorescence emission (right column images, showing the iso-intensity contour plot and the mouse silhouette). A: untreated (control) mouse; B:

HP injected subcutaneously, fluorescence image taken at 24 h after injection; C: HP injected intraperitoneally, fluorescence image after 6 h; D: HP injected intraperitoneally, fluorescence image after 24 h; E: HP injected in the left leg muscle, fluorescence image after 3 h, laser beam hitting the mouse in a region that includes the injection site; F: as in (E), but in this case the laser beam hits the mouse in a region that does not include the injection site. The grayscale indicates fluorescence intensity (CCD pixel value) in arbitrary units.

Figure 3.5 shows the optical (left) and corresponding fluorescence (right) images of the tests performed on a healthy control mouse and on healthy mice injected with the HP fluorophore with different modalities. These tests were performed in order to determine good experimental conditions as for type and site of injection and imaging exposure. The comparison of b/w images, those taken at 532 nm and fluorescence images, allows the basic check that excitation light impinges really on the region under investigation and that it spatially corresponds to fluorescence emission images. Fluorescence levels in the images obtained with the filter with wavelength cut-on at 600 nm are higher than the same images obtained with a filter with the cut-on at 650 nm. This is in agreement with the spectroscopic measurements on water HP solutions which show the presence of an emission peak located between 600 and 650 nm. Therefore, we decided to consider the images obtained with the filter with the lower cut-on wavelength. The comparison (Figure 3.5) of fluorescence images of the injected mice (normalized to the mean intensity of the laser beam during the measurement) with the control one (Figure 3.5A) shows that the increase of fluorescence due to HP administration is detectable 24 h after *sc* injection, 6 h after *ip* injection and 3 h only after *im* injection. In this last case the fluorescence is diffused in a body region well outside the injection site. Therefore, since these measurements showed that the *im* administration gives a higher and quicker HP uptake in tumors with respect to the *sc* and *ip* injection, all the successive HP injections in mice were of this type.



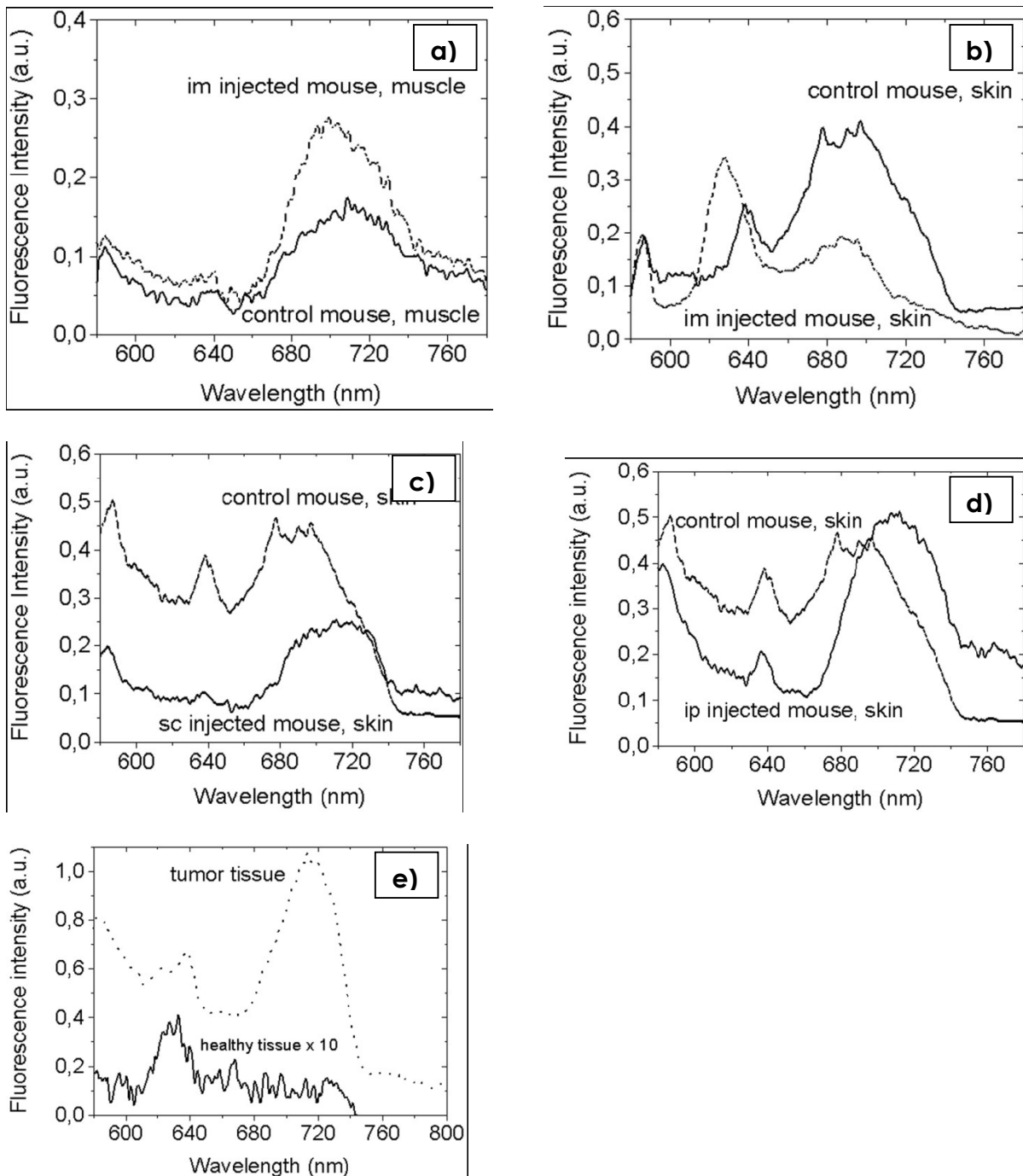
**Figure 3.6** Gray level contour plots of the tumor fluorescence (second row) and of the difference between healthy tissue and the tumor fluorescence (third row) superimposed to the mouse silhouette, 6 h (left column) and 24 h (right column) after HP administration, respectively. Note that the tumor contrast in the difference image is enhanced with respect to the fluorescence image. The tumor (<10 mm diameter) is visible on the mouse leg in the images in the first row. The grayscale on the bottom fourth row indicates fluorescence intensity levels expressed in arbitrary units.

Figure 3.6 shows (from the top to the bottom row):

- b/w image of the tumor bearing mouse;
- fluorescence image of the tumor, where the area of the laser beam, i. e. of the region irradiated by excitation laser light, is slightly greater than the tumor region;
- difference image obtained subtracting the fluorescence area of a healthy region fluorescence image of the same mouse by the fluorescence area imaged in the previous item.

The left and right column images in Figure 3.6 refer to measurements performed 6 h and 24 h after HP administration, respectively. The contrast between the tumor region and the neighboring healthy tissue is noteworthy increased in the image obtained as the difference of the fluorescence image of a healthy and the tumor region of the same mouse. In fact, by defining the contrast in terms of minimum,  $I_{\min}$ , and maximum,  $I_{\max}$ , intensity levels as the ratio  $I_{\max}/I_{\min}$ , we found that the raw fluorescence image contrast is of the order of 2, while for the digitally subtracted image is approximately 90.

We used a very simple approach, in which background digital subtraction is performed between optically filtered fluorescence image of tumor region and filtered fluorescence image of a healthy region of the same laboratory animal, taken in the same conditions. The use of the fluorescence of a healthy region of the mouse as a background fluorescence is based on our spectral measurements on the explanted tumor, reported below (see Figure 3.7 e), showing that its emission can be interpreted as a superposition of a strong tumor-associated fluorescence (peaked at approximately 700 nm) and a faint background fluorescence. The first one can be ascribed to the strong HP uptake by the tumor, the second one to the endogenous fluorescence and, possibly, to the low HP concentration fluorescence by healthy tissues. This is in agreement with the finding of Profio *et al.* (219) for an human *carcinoma in situ*. A reliable evaluation of this last fluorescence can be obtained by measuring the fluorescence of a healthy region of the mouse far enough away from the tumor region. By measuring the fluorescence of different healthy regions of the same mouse, we found relative fluctuations of the average fluorescence intensity in the order of few percent, as it can be expected if we consider that the laser beam impinges on a large fraction of the mouse surface.



**Figure 3.7:** Fluorescence spectra of frozen sample of a) muscle control mouse and *im* injected mouse histological section; b) skin control mouse and *im* injected mouse tissue; c) skin control mouse and *sc* injected mouse tissue; d) skin control mouse and *ip* injected mouse tissue; e) mice healthy/tumor tissue.

From the spectroscopic measurements of the various tissue samples it was found the following results:

- Fixation with formalin and sample keeping at 4 °C significantly affect their spectra. freezing could change indeed the optical properties of tissues, depending on the type of biological sample. Prahl (220) states that the evidence for changes of the optical properties of tissues exists for muscle tissue, while aorta and dermis seem

not susceptible to freezing artifacts. This last statement seems to be confirmed by a similar finding for optical properties of porcine skin dermis at IR wavelengths (221). In some cases, the freezing is a beneficial technique: at liquid nitrogen temperature, fluorescence spectroscopy of rapidly-frozen trapped tissue blocks was shown to recognize pathological human cervical tissues (222). In any case the freezing is necessary to obtain very thin sections and to perform, without a severe damage of the sample, spectroscopic measurement with a standard spectrofluorimeter.

- The fluorescence peaks are shifted toward longer wavelengths, being located at 635 nm and 710 nm for *ip* injected mouse skin (Figure 3.7d) and for tumor tissue (Figure 3.7e). The other spectra (Figures 3.7a, b, c) show a weak correlation with the emission spectrum illustrated in Figure 3.4. In addition, the peak at 710 nm has, in any case, height and width greater than that at 600 nm. The preferential attenuation of light to shorter wavelengths could explain these differences.
- Three h after HP inoculation, the muscle tissue of *im* injected mouse shows (Figure 3.7a) a fluorescence slightly higher than the control in the 700 nm band, while the skin sample shows an intensity decrease in this same band (Figure 3.7b). This finding could be due to the wavelength-dependent differences in absorption of the fluorescence, or to the change of the optical properties of the samples produced by the freezing.
- The fluorescence peak at 700 nm of the skin tissue (measured 24 h after HP inoculation), with respect to the control, is lower for *sc* injected mouse and higher for *ip* injected mouse (Figure 3.7 c and d, respectively). We remark that the differences of fluorescence intensity could also be due to a different thickness of the sample. Fluorescence spectra of tissue samples of the tumor bearing mouse 24 h after HP administration clearly show that the fluorescence of tumor tissue increases by a factor up to approximately 100 with respect to healthy tissue in the wavelength band at longer wavelengths (Figure 3.7 e).

### *b. HP\_FRI in vivo*

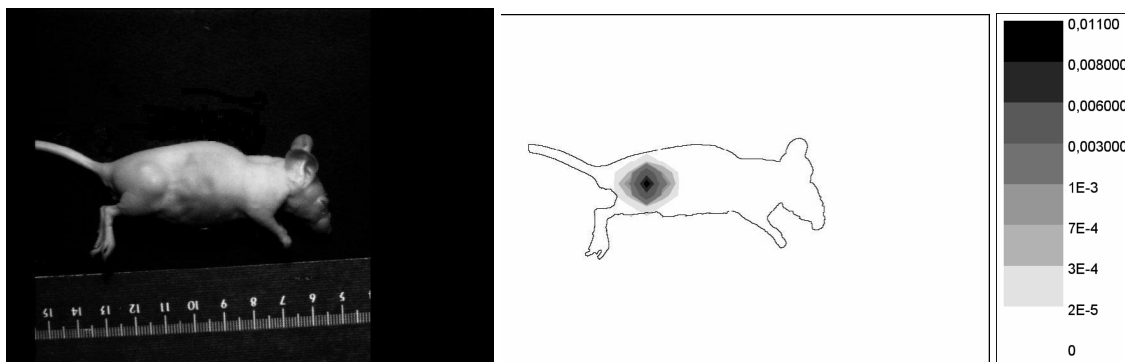


**Figure 3.8:** Images of an ARO tumor bearing mouse: left side: white light image; right side: fluorescence image after digital background subtraction, superimposed to the mouse silhouette. The grey scale of the fluorescence isointensity regions is also reported.

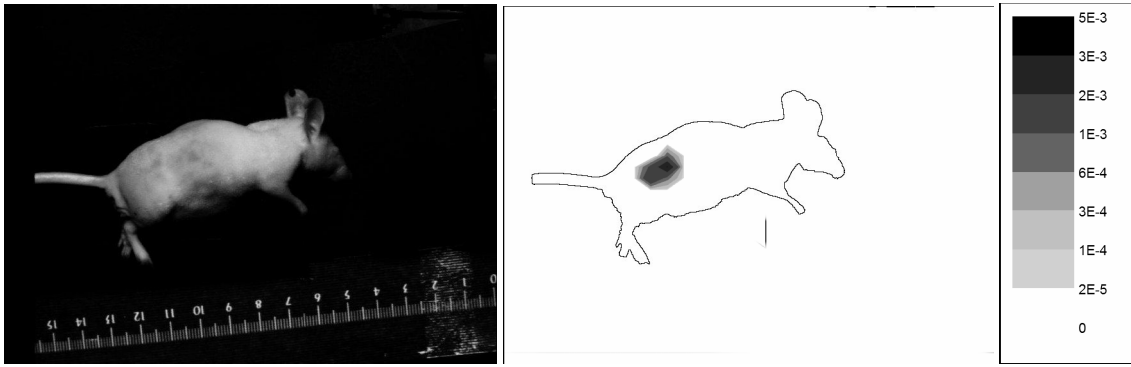


**Figure 3.9:** Image of an NPA tumor bearing mouse: left side, white light image, right side, fluorescence image after digital background subtraction, superimposed to the mouse silhouette. The grey scale of the fluorescence iso-intensity regions is also reported.

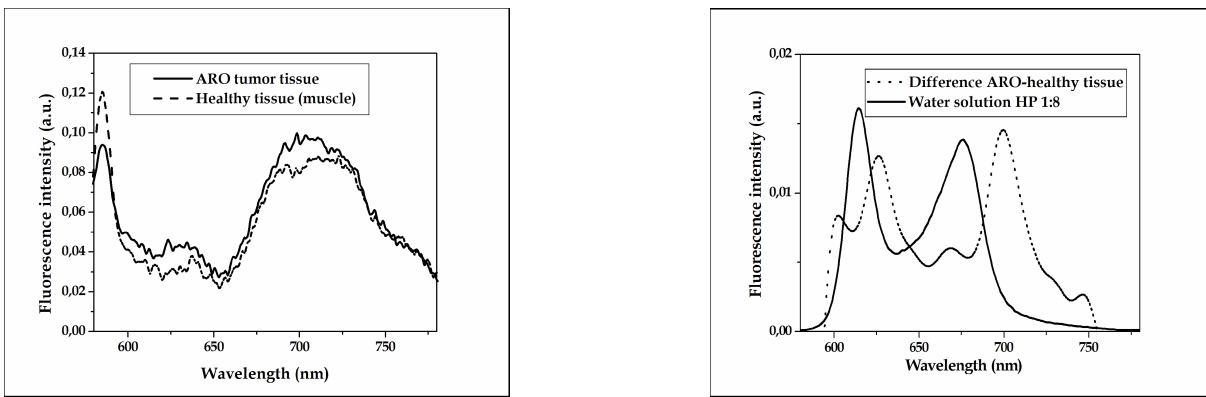


**Figure 3.10:** Left side: fluorescence spectra of histological sections of an ARO tumor tissue (solid line) and a healthy muscle tissue (dashed line) for the mouse imaged in Fig. 2. Both fluorescence spectra are the mean of the fluorescence spectra of several histological sections of the same tissue. Right side: difference between the fluorescence spectrum of sections of ARO tumor and healthy tissue in comparison with the fluorescence of HP water solution diluted 1:8.

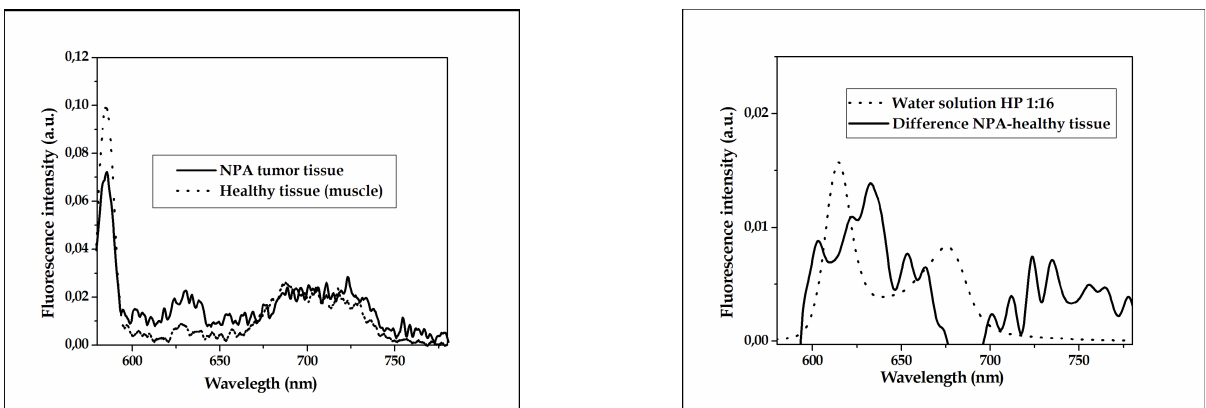


**Figure 3.11:** Left side: fluorescence spectra of histological sections of an NPA tumor tissue (solid line) and a healthy muscle tissue (dashed line) for the mouse imaged in Fig. 3. Both fluorescence spectra are the mean of the fluorescence spectra of several histological sections of the same tissue. Right side: difference between the fluorescence spectrum of sections of NPA tumor and healthy tissue in comparison with the fluorescence of HP water solution diluted 1:16.

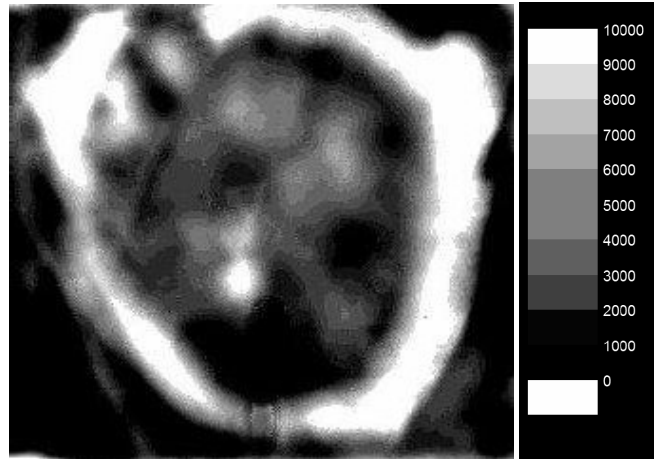


**Figure 3.12:** Fluorescence image of a histological section of ARO tumor tissue. On the right side the grey scale of fluorescence isointensity regions is reported. The fluorescence emission is higher in the skin tissue near the tumor and in those regions that appear non necrotic from the histological analysis.

The HP-FRI images, after the digital background subtraction, superimposed on the mouse silhouette of the ARO tumor bearing mouse #2 and NPA tumor bearing mouse #2, reported in right side of Figures 3.8 and 3.9 respectively, show that a fluorescence intensity enhancement is present in the region where the tumor is visually recognizable, according to the preferential accumulation of the HP fluorescent marker in the tumor region with respect to the healthy region. In the fluorescence images, the fluorescence emission of ARO tumors, more malignant with respect to NPA tumors appears higher than the fluorescence emitted by NPA tumor. This observation is confirmed by the quantitative analysis performed on the fluorescence images by means of the fluorescence emissivity ratio, a parameter used to characterize the fluorescence properties of the two different types of investigated tumors. It was calculated by integrating the fluorescence image (normalized to the laser beam intensity, but not background subtracted) and by dividing it by the area of the irradiated region of the mouse, which coincides with very good approximation with the tumor area. The ratios between these emissivity values for unit area for the tumor region and those for a healthy region of a same mouse were calculated for each analyzed mouse. It was found that the value of this parameter for the ARO tumor tissue is generally greater than that for the NPA tumor tissue, the mean value of the fluorescence emissivity ratio for ARO tumor being about two times that for the NPA tumor (Table 1). This seems to indicate that higher fluorescence emissivity is associated to higher malignancy degree.

NPA/ARO mouse number	1	2	3	4	5	6	7	8	9	10	Mean	SD
NPA/healthy tissue emissivity	2.70	1.87	1.66	2.60	1.53	1.20	2.60	3.91	1.00		2.1	0.3
ARO/healthy tissue emissivity	1	4.72	2.08	2.68	10.29	6.30	4.22	2.30	3.71	1.2	3.9	0.9

**Table 1** Fluorescence emissivity ratio values for the examined NPA and ARO tumors. The corresponding mean values and standard deviations (SD) are listed in the last two columns.

In Figure 3.10 the fluorescence spectrum of histological sections of tumor tissue is compared with that of the healthy tissue for the ARO tumor imaged in Figure 3.8 (left side). In the right side of the same figure, the difference between the fluorescence spectra of histological sections of tumor and healthy tissue is compared with the fluorescence spectrum of HP water solution at a suitable dilution factor. Figure 3.11 shows the same quantities in Figure 3.10 for the NPA tumor imaged in Figure 3.9. The right side spectra in Figures 3.10 and 3.11 show also a red shift of the HP spectrum in cells with respect to the spectrum obtained for HP water solution.

The spectroscopic results confirm those of the HP-FRI. In fact, in the wavelength region 550 - 800 nm, that is the spectral band contributing to the fluorescence imaging, the spectral intensity of the tumor tissue, both ARO and NPA, is higher than that of the healthy tissue (left side plot of Figures 3.10 and 3.11). The difference in the fluorescence emission we have found for the two types of tumors can be explained in terms of different HP uptake by tumors. The plots in the right side of Figures 3.10 and 3.11 show that the difference between the fluorescence spectrum of sections of tumor and healthy tissue, i.e. the net emission of HP accumulated in the tumor, is consistent with the spectrum of water solution of HP at the dilution factor 1:8 for the ARO tumor and 1:16 for the NPA tumor.

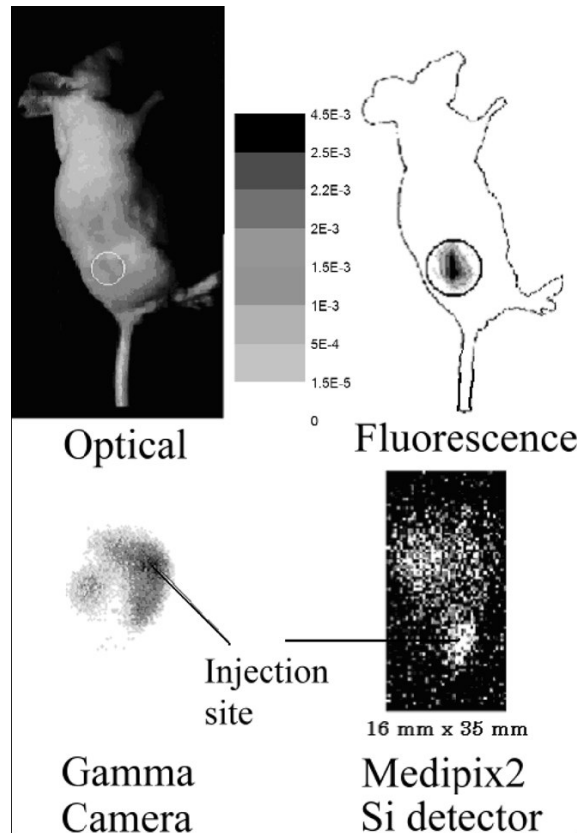
A series of findings can be found in the literature according to this result. Gupta et al.(223) found that the oral squamous carcinoma cells accumulated significantly higher amounts of HpD (a mixture of ether and ester linked porphyrins, that in a partially purified form takes the commercial name of Photofrin II) than glioma cells. They conclude that this difference could be imputed to the variations of the frequency and affinity of HpD binding sites as well as the aggregation and ionic states of intracellular HpD. Similarly it was found that Photofrin II uptake is slightly higher for leukaemic T cell lymphoblast Jurkat cells than for breast adenocarcinoma MCF 7 cells (224). This result is explained by a different membrane composition and LDL receptor presentation. HpD level in glioma was correlated to the grade of evolution and malignancy of the tumor, highest levels of photosensitizers being present in glioblastoma, lower levels in intermediate-grade anaplastic astrocytoma and low-grade astrocytoma (225). This last result agree qualitatively with our finding that poorly differentiated highly malignant ARO cells show a greater HP uptake than highly differentiated less malignant NPA cells. In the above referenced paper (224) it is also reported a red-shift of the fluorescence spectra of Photofrin II in both tumor cell lines with respect to the spectrum of the same compound dissolved in PBS (hydrophilic) solution. From the observation that a red shift of 20 nm is obtained when the photosensitizer is dissolved in PBS solution and in lipophilic environment (PC liposome) the authors argue that this spectral change of Photofrin II is due to its incorporation in cell membrane.

Finally, Figure 3.12 shows the fluorescence image of the histological section of an ARO tumor (mouse # 9): clearly the fluorescence is higher in the skin around the tumor and in the region where tumor cells are viable, while it is very low in the tumor regions appearing necrotic from the histological analysis. This suggests that the HP retention is concentrated in the peritumor region and it is absent in the necrotic region.

### *c. Combined imaging*

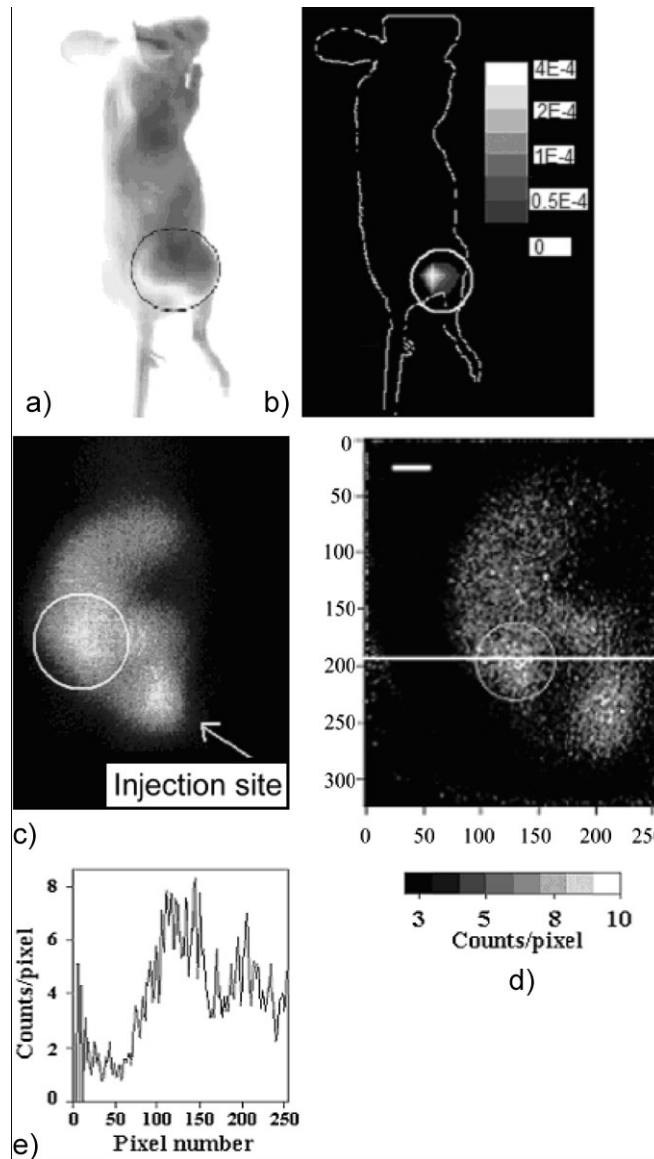
In the following, we present two combined images (white light, isointensity fluorescence contour plot superimposed on the mouse silhouette, commercial pinhole gamma camera, hybrid pixel detector Medipix2) generated after different test sessions. The comparison of the images taken in the different modalities is presently carried out offline and visually using an image processing software, by rotating, mirroring and scaling the images in order to have a rough visual match of the structures.

Figure 3.13 shows the combined images of the NPA tumor-bearing mouse. The gamma detector is the Medipix2 Si pixel hybrid detector. The acquisition time for the optical system was less than half minute and 25 minutes with the radionuclide imaging system with a total 80000 counts. The resolution in gamma-ray imaging is about 2 mm (with a 0.78-mm pinhole diameter) and the FOV is 16x35 mm<sup>2</sup>. The system spatial resolution was calculated by summing in quadrature the intrinsic detector resolution (as twice the detector pixel pitch) and the knife-edge pinhole geometric resolution due to its 140-keV effective diameter, taking into account the system magnification  $M=0.4$ . The fluorescence emissivity ratio is about 2. The quality of the inefficient silicon detector is very poor due to its low count statistics (a bare 3200 cpm). We show it mainly for comparison with the following CdTe detector image and to indicate the progress in the development of our project. However, this figure indicates that the NPA tumor was clearly observed only in the fluorescence image, since the area of accumulated counts showed in the Medipix2 image was found to correspond to the injection site, after the comparison with the image from the gamma camera.



**Figure 3.13** Combined images of an NPA tumor-bearing mouse. In this case, the tumor (circled area) is visible only in the fluorescence image, while the gamma camera and Medipix2 systems show an accumulation of counts only in a region corresponding to the radionuclide injection site. The Medipix2

silicon detector image has a FOV = 16 x 35 mm<sup>2</sup> and contains 80 000 counts in total (25 min acquisition time). The pinhole magnification in this Medipix2 image is M = 0.4. Injected activity = 74 MBq( <sup>99m</sup>Tc).



**Figure 3.14** Images of an ARO tumor-bearing mouse. a) Optical. b) Fluorescence. c) Clinical pinhole gamma camera. d) Medipix2 CdTe pixel detector (1-mm pinhole) (5 min acquisition time, low-pass filtered image). e) Count profile along the line indicated in d). The surface tumor area (7–8 mm in diameter) is circled. The arrow indicates the injection site. The count rate of the gamma camera image is 200 000 cpm. The Medipix2 image (pinhole magnification = 0.45) has an area of 256x322 pixels (about 32x40mm<sup>2</sup>), a count rate of 40 000 cpm and it has been obtained by the composition of two partially overlapped images; the white bar corresponds to 4 mm. Injected activity = 74 MBq( <sup>99m</sup>Tc). The images have been matched visually. In the fluorescence and radionuclide images the circle delineates the area of maximum signal intensity.

Figure 3.14 shows the combined images of the ARO tumor-bearing mouse. The gamma detector is now the Medipix2 CdTe pixel hybrid detector. With the radionuclide imaging system the acquisition time is 5 minutes with a total of 200000 counts, the spatial resolution, calculated as above, is about 3 mm (with a 1 mm pinhole diameter,

magnification  $M=0.45$ ), the  $FOV= 32\text{mm}^2$ . The short acquisition time permitted by the CdTe hybrid pixel detector has made possible a longitudinal scan of the mouse body in steps of 10 mm (adjacent images have a field of view (FOV) partially overlapping). With the composition of two such images, we have thus obtained a rectangular FOV of  $32 \times 40 \text{mm}^2$ . The line profile across the tumor area shows an increased activity (by a factor of roughly 3:1 in the tumor area with respect to the background). We notice that in our experimental conditions, the CdTe based system produced 9 cps/MBq as against 0.7 cps/MBq for the Si based system (i.e., just a factor 12 higher, as against a factor greater than 30 in the quantum efficiencies of our CdTe and Si detectors), while the mouse imaging with the scintillator based clinical gamma camera was performed with 45 cps/MBq. We also notice that, from the analysis of tissue autoradiographies (data not shown), both the ARO and NPA tissue sections appear radioactive in the tumor area.

Different imaging modalities may supply different information for *in vivo* imaging, that could determine improvements on oncological investigations (226) and tumor diagnosis. For example, in Figure 3.13 (NPA-type tumor) the tumor area was detected only by the fluorescence technique (although with a low fluorescence signal), while the gamma camera and the Medipix2 hybrid pixel detector were unable to detect it. This different behavior could be ascribed to different mechanism of accumulation of  $^{99\text{m}}\text{Tc}$ -MIBI and HP in tumor cells. HP is reported to enter *in vivo* cells following its binding with serum lipoproteins and albumin, to diffuse in the cytoplasm and to localize in mitochondria (227).  $^{99\text{m}}\text{Tc}$  -MIBI diffuse across cell membrane via passive diffusion and is largely sequestered in mitochondria (228). Washout of  $^{99\text{m}}\text{Tc}$  -MIBI is related to transmembrane transporter proteins whose concentration in different cell types determines the tracer uptake (229-231).

However  $^{99\text{m}}\text{Tc}$  -MIBI uptake was found strongly dependent on the viability of the thyroid tissue (232). To the purpose of assembling a compact gamma-ray imaging system with semiconductor detectors, the Medipix2 system offers some advantages. Though its sensitive area is just  $2 \text{cm}^2$ , the use of a pinhole collimator in demagnification allows reaching a FOV useful for imaging the entire tumor area, while exploiting the high intrinsic spatial resolution of this hybrid pixel detector.

Previous studies (233,234) using a Medipix1 silicon detector had already revealed the feasibility of designing a compact gamma camera with such hybrid pixel detectors, with high intrinsic spatial resolution. As for its sensitivity, the 1-mm thick CdTe detector with a 1-mm pinhole collimator produced 9 cps/MBq; a thicker and more efficient CdTe detector (e.g., 2 mm or higher) is expected to improve the detection efficiency and hence the system sensitivity.

### 3.5 Conclusions

From the preliminary and first HP-FRI measurements we wish outline that:

- a) The fluorescence spectra of water solution of HP for different concentration values exhibit the well known emission peaks around 610 nm and at 680 nm.
- b) The fluorescence spectra of water solution of HP don't change in the range of time durations, temperatures and light doses typical of our experiments.
- c) The optimal injection site is the muscle, the *ip* and *sc* injection leading to a lower fluorescence emission in the tumor tissue.

- d) The optimal delay between the time of the HP injection and the FRI measurements is between 6 and 24 h.
- e) The well known selective uptake by tumors of HP compound is confirmed also for our HP dichlorohydrate by the FRI *in vivo* measurements.
- f) The results of HP-FRI imaging *in vivo* in mice are consistent with spectroscopic results on samples excised by tumor and healthy tissues of the mice and by fluorescence imaging of histological sections of tumor tissues.
- g) In the case studied of mice bearing two different types of tumors, by the combined imaging *in vivo* we were able to discriminate the different uptake of the gamma/fluorescent marker in the tumor (235).

The detection of HP mediated fluorescence is characterized from the use of a non specific fluorochrome and it could not be classified as a quantitative technique for tumor imaging, since it is very difficult to control the number of parameters determining the cellular fluorescence response (236-238). This type of compounds has been largely studied in the past years because of their tumor selective uptake, which has been exploited especially for photodynamic purposes. In the photodynamic therapy (PDT) the interest for porphyrin compounds is increased in the years producing a large number a new photosensitizers, the so called "second generation porphyrins", in the attempt of decreasing the photosensibilization effects and allowing for a better therapeutic effect. Although the PDT is the main application of the porphyrin compounds, they have been applied also in the photodiagnosis (6). Nevertheless, the HP-FRI techniques has many advantages: short measurement times, high spatial resolution, large field of view, wide applicability to a large variety of surface tumors. It is able to reveal tumor *in vivo* through the increased optical contrast of the tumor region with respect to the surrounding healthy tissue and also to distinguish tumor of different malignancy degree being higher the fluorescence emissivity higher is the malignancy degree of the tumor. We limited our attention to surface tumors of macroscopic dimension (<2 cm), that are relatively simple to be revealed with FRI.

### 3.6 Appendix: an overview on CCD technology(239)

CCD detectors are made of silicon crystals sliced into thin sheets for fabrication into integrated circuits using similar technologies to those used in making computer silicon chips. One of the properties of silicon-based detectors is their high sensitivity to light. Figure A.1 (240) represents a schematic illustration of a CCD chip. Electrical potential wells, known as picture elements (pixels) are created, during manufacture, as a rectangular array on the surface of the silicon. When the CCD image sensor is exposed to photons (light), which are able to penetrate into the silicon layer, the energy breaks the bonds that bind the electrons to the silicon lattice, releasing an electron per photon of light absorbed. Applied voltages create electrical potentials on the pixels preventing transfer of charge between adjacent wells. The charge can then be transferred to adjacent pixels by altering their relative potentials. In this way, a charge pattern, corresponding to the intensity of incoming photons, is read out of the CCD into an output register and amplifier at the edge of the CCD for digitization. This process of converting incoming photons to electrons and capturing them in discreet wells is extremely linear, meaning that as the exposure time on

a sample is increased, the output signal increases in exact proportion until the well is full and saturation has occurred. This feature is extremely useful for quantification in fluorescence imaging. The digitized image can then be transferred *via* a dedicated data link to a fast PC for storage and subsequent analysis.

In summary, there are many different types of CCD chip available whose features are suited for particular applications. Some of the features that define the differences between CCD types, such as pixel size, chip geometry, quantum efficiency and readout rate have been briefly discussed in this Appendix.

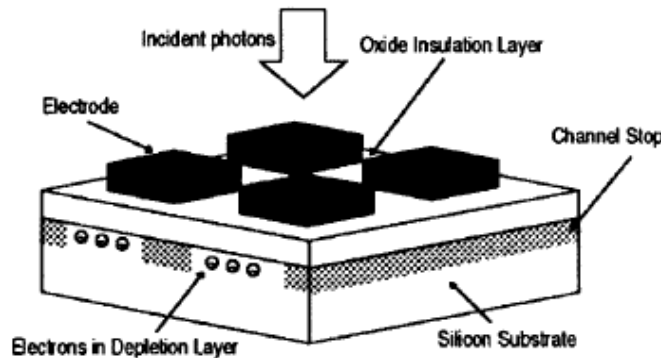


Figure A.1. Schematic cross-section of a CCD.

### Scientific Camera Types

Scientific Digital cameras come in 4 primary types based on the sensor technology they use. The principal forms of high performance digital camera include:

- The popular Charge-Coupled Device (CCD) Camera
- The Electron Multiplying Charge Coupled Device (EMCCD) Camera
- The Complementary-Metal-Oxide-Semiconductor (CMOS) detector camera
- The Image Intensified CCD Camera (ICCD)

In the first three detectors, a silicon diode photosensor (pixel) is coupled to a charge storage region that is, in turn, connected to an amplifier that reads out the quantity of accumulated charge. Incident photons generate electronic charges, which are stored in the charge storage region. If the incident photons have sufficient energy and they are absorbed in the depletion region, they liberate an electron which can be detected as a charge. Then, the transmission and absorption properties of the silicon define the spectral response of the detector and this is explained further as QE in a later section.

In a CCD, there is typically only one amplifier at the corner of the entire array and the stored charge is sequentially transferred through the parallel registers to a linear serial register, then to an output node adjacent to the read-out amplifier (Figure A.2). CCD sensors were first developed in the late 60's and the technology is relatively mature now. CCD performance has pushed the boundaries in the efficiency of light detection and in reducing the noise from either dark signal or amplifier readout. One weakness of a CCD is the fact that the CCD is essentially a serial readout device and low noise performance is only achieved at the expense of slow readout speeds. CMOS cameras can achieve high frame rates with moderate sensitivity.

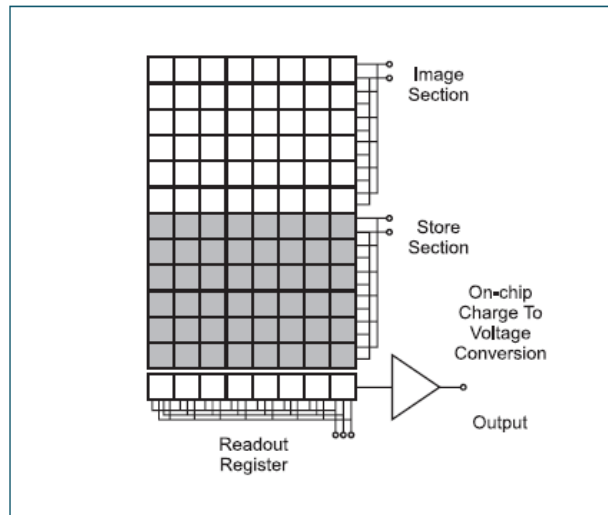


Figure A.2 Typical CCD structure

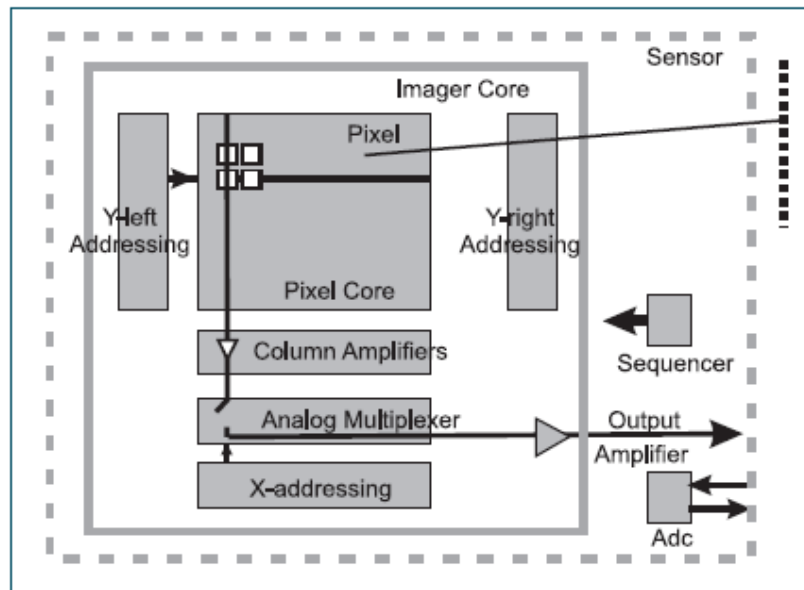
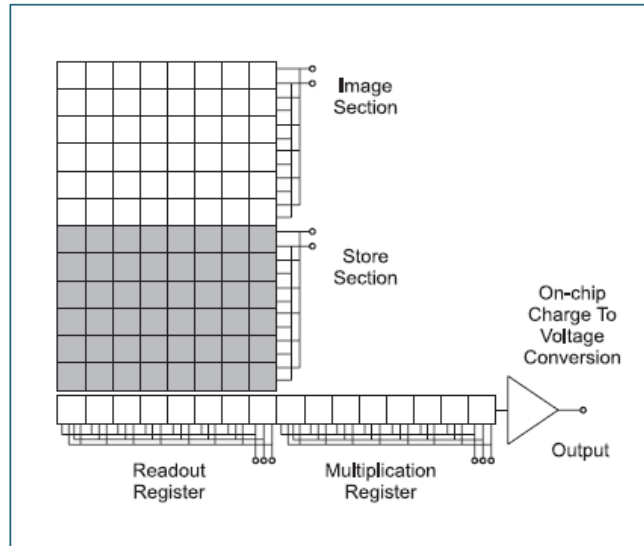


Figure A.3 CMOS structure

In CMOS detectors, each photosensor or, more typically, each column of photosensors has an amplifier associated with it (Figure A.3). A row of pixels can be readout in parallel with the row selected by an addressing register or an individual pixel can be selected by column multiplexer. A CMOS device is essentially a parallel readout device and therefore can achieve higher readout speeds particularly required by imaging applications. CMOS detector technology however still needs considerable development to compete against CCD for performance in scientific applications. To achieve the parallel readout the CMOS amplifier uses multiple amplifiers, each with its own gain, linearity and noise performance variation. Compensating for the variations in the current state of the art CMOS devices is difficult over a wide range of illumination levels and to the accuracy required by scientific applications. High speed readout with high sensitivity can be achieved by EMCCD cameras.



**Figure A.4** EMCCD structure

The EMCCD has essentially the same structure as a CCD with the addition of a very important feature (Figure A.4). The stored charge is transferred through the parallel registers to a linear register as before but now prior to being readout at the output node the charge is shifted through an additional register, the multiplication register in which the charge is amplified. A signal can therefore be amplified above the readout noise of the amplifier and hence an EMCCD can have a higher sensitivity than a CCD. EMCCDS use similar structures to CCD's and are similarly restrained in the minimum exposure time they can achieve.

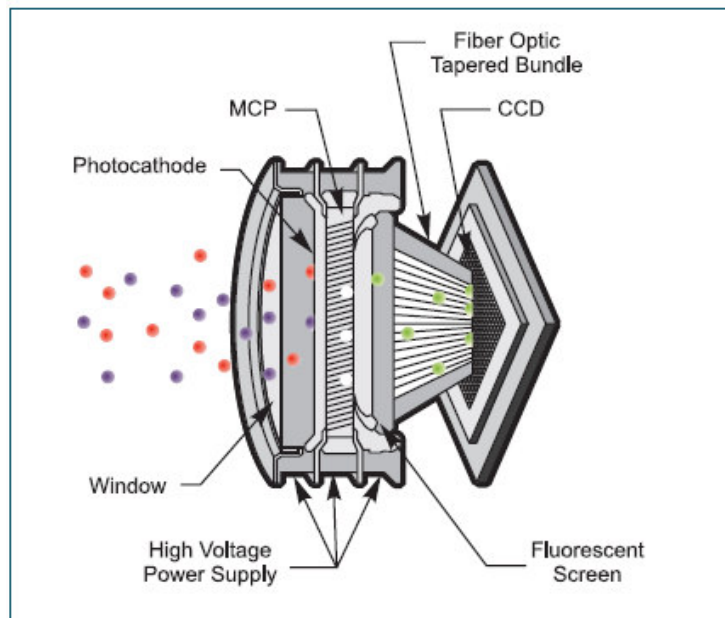


**Figure A.5** ICCD structure

Intensified CCD Cameras can achieve ultra short exposure times. In the Image Intensifier a photosensitive surface (Photocathode) captures incident photons and

generates electronic charges that are sensed and amplified (Figure A.5). The photocathode is similar in nature to the photosensitive region of a Photomultiplier tubes (PMTs) that are widely used in confocal microscopes and spectrometers. When photons fall on a photocathode they utilize the energy of the incident photons to release electrons. The liberated electrons are then accelerated toward an electron multiplier composed of a series of angled tubes known as the Micro-Channel Plate. Under the accelerating potential of a high voltage, the incident electrons gain sufficient energy to knock off additional electrons and hence amplify the original signal. This signal can then be detected in several ways, either by direct detection using a CCD (also called an EBCCD Electron Bombardment Charge Coupled Device) or indirectly by using a phosphor and CCD. The ICCD can achieve short exposure times by using a pulsed gate voltage between the photocathode and MCP. By applying a small positive voltage, electrons liberated by the photocathode can be suppressed and hence not detected. By switching the voltage to a negative voltage, electrons from the photocathode are accelerated across the gap to the MCP where they can be amplified and detected. By applying a suitable short voltage pulse the intensifier can therefore be effectively turned on and off in sub nanosecond intervals.

ICCD cameras find uses in applications where short exposure times or gating is required such as LIBs or combustion research.

CCD cameras are the camera of choice for most scientific applications which require sensitivity or dynamic range. The sheer range of CCD sensor options offers the prospect to select a sensor of the best overall characteristics for applications ranging from astronomy to spectroscopy. CCD technology is relatively mature while CMOS technology still needs major development to compete with CCD's in scientific applications.

An EMCCD camera works best in applications when a high sensitivity needs to be coupled with high speed such as fluorescent microscopy or ultra fast spectroscopy. EMCCD is relatively new technology and there is still a relatively limited range of sensor formats currently available. In coming years these sensors are expected to get faster with increasing numbers of formats becoming available.

Hybrid sensors which combine CCD and CMOS technologies can potentially deliver performance superior to either CCD or CMOS bulk detectors. They look the better long term option but there is still a considerable amount of development required before they can be commercially viable. In particular to overcome the issues associated with compensating for the variation of the multiple amplifiers. Many of the principals that apply to CCD's also apply to other camera formats. In the following section we will cover the characteristics of the CCD and then cover in more detail EMCCD's and ICCD's in later sections and highlight how their characteristics differ.

### **CCD Sensor Formats**

The most common scientific camera, the Charge Coupled Device camera (CCD), comes with three fundamental architectures and these are Full Frame, Frame Transfer and Interline format.

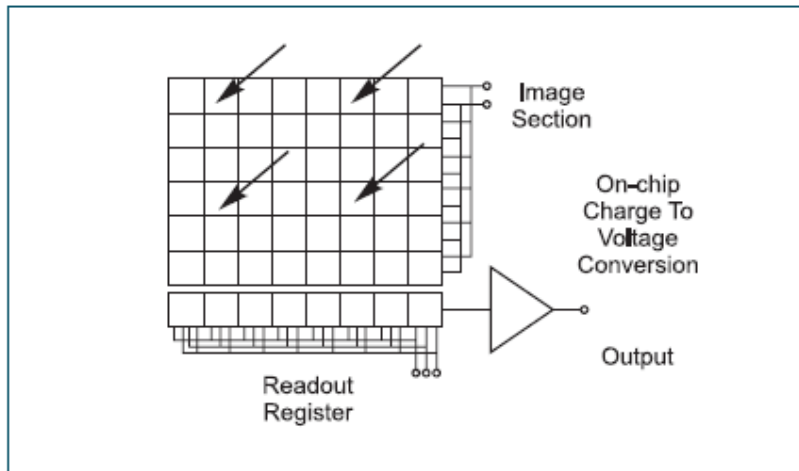


Figure A.6 Typical full-frame CCD sensor format

The full frame CCD is the simplest form of sensor in which incoming photons fall on the full light sensitive sensor array (Figure A.6). To readout the sensor the accumulated charge must then be shifted vertically row by row into the serial output register and for each row the readout register must be shifted horizontally to readout each individual pixel. This is known as "Progressive Scan" readout. A disadvantage of full frame is charge smearing caused by light falling on the sensor whilst accumulated charge signal is being transferred to the readout register. To avoid this, devices sometimes utilize a mechanical shutter to cover the sensor during the readout process. However, mechanical shutters have lifetime issues and are relatively slow. Shutters are not needed however in spectrographic operations or when a pulsed light source is used. Full frame CCD's are typically the most sensitive CCD's available and can work efficiently in many different illumination situations.

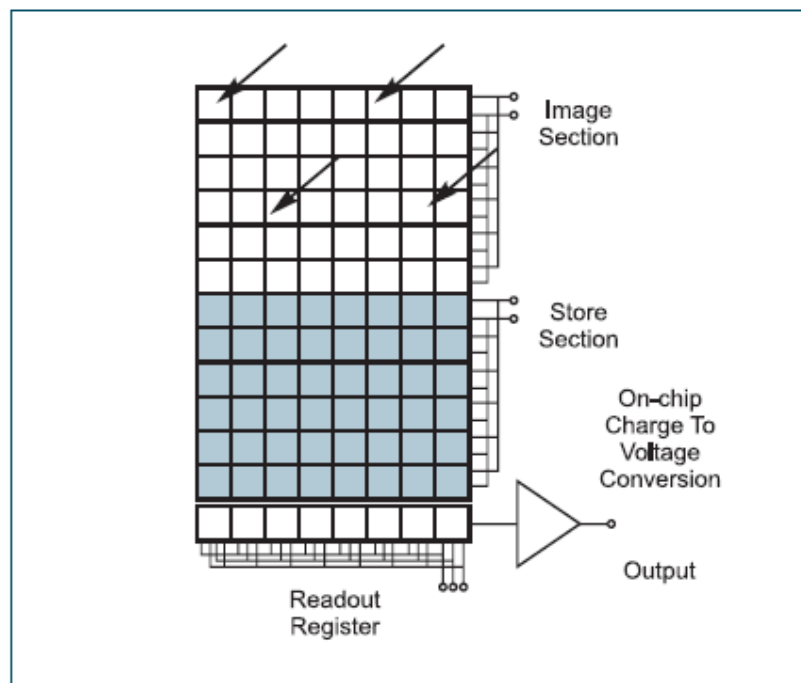
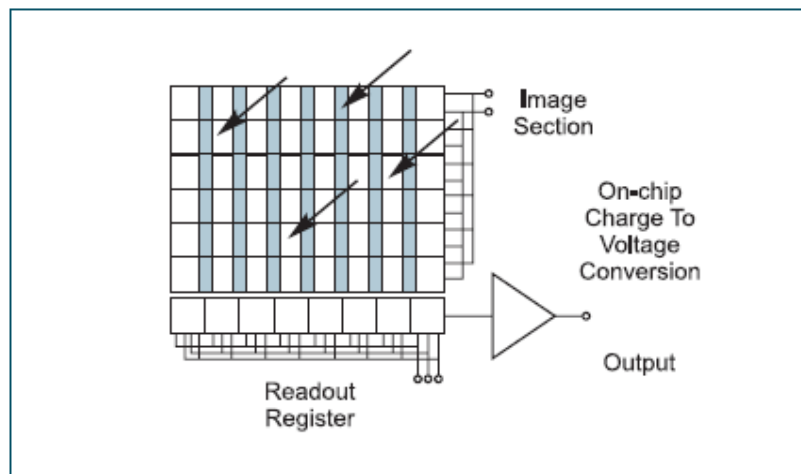


Figure A.7 Typical frame-transfer CCD sensor format

The frame-transfer CCD uses a two-part sensor in which one half of the parallel array is used as a storage region and is protected from light by a light-tight mask (Figure A.7). Incoming photons are allowed to fall on the uncovered portion of the array and the accumulated charge is then rapidly shifted (in the order of milliseconds) into the masked storage region for charge transfer to the serial output register. While the signal is being integrated on the light-sensitive portion of the sensor, the stored charge is read out. Frame transfer devices have typically faster frame rates than full frame devices and have the advantage of a high duty cycle i.e. the sensor is always collecting light. A disadvantage of this architecture is the charge smearing during the transfer from the light-sensitive to the masked regions of the CCD, although they are significantly better than full frame devices. The frame transfer CCD has the sensitivity of the full frame device but are typically more expensive due to the larger sensor size needed to accommodate the frame storage region.



**Figure A.8** Typical interline transfer CCD sensor format

The interline-transfer CCD incorporates charge transfer channels called Interline Masks (see Figure A.8). These are immediately adjacent to each photodiode so that the accumulated charge can be rapidly shifted into the channels after image acquisition has been completed. The very rapid image acquisition virtually eliminates image smear. Altering the voltages at the photodiode so that the generated charges are injected into the substrate, rather than shifted to the transfer channels, can electronically shutter interline-transfer CCDs. Interline devices have the disadvantage that the interline mask effectively reduces the light sensitive area of the sensor. This can be partially compensated by the use of microlens arrays to increase the photodiode fill factor. The compensation usually works best for parallel light illumination but for some applications which need wide angle illumination (small F/# number) the sensitivity is significantly compromised.

### Spectral Response

The spectral response of a camera refers to the detected signal response as a function of the wavelength of light. This parameter is often expressed in terms of the Quantum Efficiency (QE), a measure of the detector's ability to produce an electronic charge as a percentage of the total number of incident photons that are detected.

The spectral response (or QE) of the CCD is governed by the ability of the photons to be absorbed in the depletion region of the detector. It is only in the depletion region that photons are converted into electronic charges and subsequently can be held by the electric fields which form the pixel. The charge held in the depletion region is then transferred and measured. To highlight the spectral response effects lets examine the cross section of a typical CCD detector shown in Figure A.9.

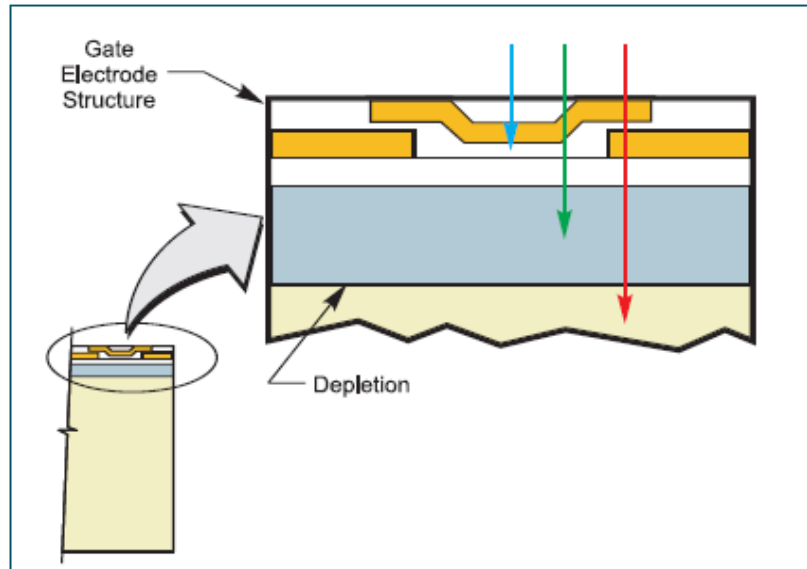


Figure A.9 CCD cross section showing depletion region

Photons falling on the CCD must first transverse the region dominated by the gate electrodes by which the applied clocking voltages create the electric fields that form the boundary of the depletion region and shift charge through the CCD. The gate structures can absorb or reflect all wavelengths to some extent and as a result reduce the spectral response below the theoretical maximum of 1 electron charge generated per one photon (in the case of visible light). The shorter wavelengths (blue light) are particularly absorbing and below  $\sim 350\text{nm}$  they absorb all the photons before they can be detected in the depleted region. Photons with longer wavelengths (i.e. red photons) have a low probability of absorption by the silicon and can pass through the depletion region without being detected and hence reduce the red sensitivity of the device. Photons with wavelengths greater than  $1.1\mu\text{m}$  do not have enough energy to create a free electron charge and so they cannot be detected with Silicon CCD's. The various absorption effects combine to define the spectral sensitivity of the CCD. The spectral sensitivity is typically expressed as a QE Curve, in which the probability to detect a photon of a particular wavelength is expressed as a percentage. So for example if one in every 10 photons is detected this is expressed as a QE of 10%.

The losses due to the gate electrode structure can be completely eliminated in the Back-Illuminated CCD. In this design, light falls onto the back of the CCD in a region where the bulk of the silicon has been thinned by etching until it is transparent (a thickness corresponding to about 10-15 microns). Back-thinning results in a delicate, relatively expensive sensor that has only been employed in high-end scientific grade CCD cameras.

## Camera Sensitivity & Noise

The sensitivity of a camera is typically expressed in either the number of photons or in a measure of photon flux which can be related to human observations, called the lux. A lux is a measure of illumination which has a value of 1 lumen per square meter. The lumen is a photometric equivalent of a Watt which is weighted to match the eye response of the "standard observer".

The sensitivity of the human eye varies at different wavelengths and this has an implication of the number of photons equivalent to a given photometric quantity. The conversion to photons in the table above assumes the light is monochromatic yellowish green light with a wavelength of 555nm which is at the peak of the sensitivity of the human eye. For a given minimum sensitivity in lumens the number of photons varies (Figure A.10).

Wavelength	Photons per second	Radiometric Measure Watts	Photometric Measure Lumens
450	213	9.40E-17	2.44E-15
555	10	3.58E-18	2.44E-15
650	110	3.36E-17	2.46E-15

Figure A.10

If a given light signal induces a signal on the camera below the readout noise of the camera, it cannot be detected so the total noise of the camera is a useful way to define the sensitivity of the camera.

The noise measured by a digital camera comes from a number of sources which will be covered in detail in a later section. Here we will concentrate predominately on the three main sources and they are:

- Sensor readout noise
- Thermal noise
- The noise from the signal itself: photon noise

The total camera noise is the sum in quadrature calculated as:

$$\sigma_{\text{total}} = \sqrt{(\sigma_{\text{signal}}^2 + \sigma_{\text{dark}}^2 + \sigma_{\text{readout}}^2)}$$

The readout noise is an inherent property of the sensor and is usually the limit on sensitivity for most cameras. The readout noise is a combination of noise sources, which originate from the process of amplifying and converting the photoelectrons created into a voltage. Over the years readout noise has improved but fundamentally the faster the readout of the camera, the higher the noise due to the increasing bandwidth required. Low noise CCD's in the past have typically employed very low readout speeds and hence they are often known as Slow Scan CCD's.

The second source of noise is the dark noise that arises from thermally generated charges in the silicon sensor. Recent improvements in CCD design have greatly diminished dark noise to negligible levels and reduced their contribution to total read-out noise to less than 10 electrons per pixel at room temperatures. For the ultimate sensitivity

cooling the CCD to temperatures  $\sim -100^{\circ}\text{C}$  is still required. Some room temperature cameras may have such a low dark signal that it can be ignored for integration periods of a second or less. Cooling further reduces the dark signal and permits much longer integration periods, up to several hours, without significant dark charge accumulation. The noise arising from the dark charge is given by Poisson statistics as the square root of the charge arising from the thermal effects, i.e.:

$$\sigma_{\text{dark}} = \sqrt{N_{\text{dark}}}$$

The incoming photons have an inherent noise  $\sigma_{\text{signal}}$  known as photon Shot noise. If we consider the effects of a number of photons  $P$  which would generate in a pixel with QE  $D_{\text{QE}}$  a signal of  $N_e$  electrons, they will have a noise as defined by Poisson statistics shown here:

$$\sigma_{\text{signal}} = \sqrt{D_{\text{QE}}P}$$

### Dynamic Range

The dynamic range of a CCD is typically defined as the full-well capacity divided by the camera noise and relates to the ability of a camera to record simultaneously very low light signals alongside bright signals. The ratio is often expressed in decibels which is calculated as  $20\log(\text{full well capacity}/\text{read noise})$  or in the equivalent number of A/D units required to digitize the signal.

The full well capacity is the largest charge a pixel can hold before saturation which results in degradation of the signal. When the charge in a pixel exceeds the saturation level, the charge starts to fill adjacent pixels a process known as blooming (see below). The camera also starts to deviate from a linear response and hence compromises the quantitative performance of the camera. Larger pixels have lower spatial resolution but their greater well capacity offers higher dynamic range which can be important for some applications.

### Blooming & Anti-blooming

Blooming occurs when the charge in a pixel exceeds the saturation level and the charge starts to fill adjacent pixels. Typically CCD sensors are designed to allow easy vertical shifting of the charge but potential barriers are created to reduce flow into horizontal pixels. Hence the excess charge will preferentially flow into the nearest vertical neighbours. Blooming therefore produces a characteristic vertical streak, e.g. see Figure A.11.

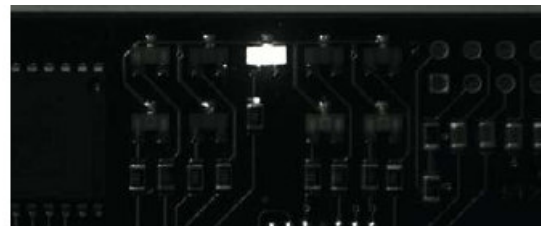
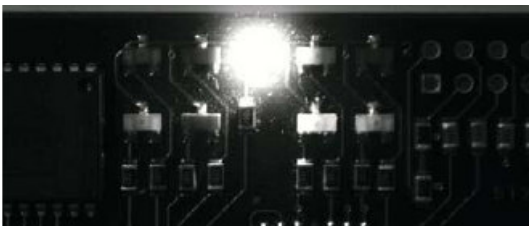


Figure A. 11

Blooming can be a nuisance when a strong signal can obscure data from a weak signal of interest especially on an image with a high dynamic range. Some sensors are designed with structures built into them which limit blooming, anti-blooming structures. Anti-blooming structures bleed off any excess charge before they can overflow the pixel and thereby stop blooming. Anti-blooming structures can reduce the effective quantum efficiency and introduce non linearity into the sensor. Therefore anti-blooming sensors are not recommended for applications requiring very low light or high accuracy measurements. As an alternative to using anti-blooming sensors an image can be acquired using accumulation mode. Accumulation mode allows successive scans of shorter exposures to be summed to achieve effectively an exposure which is longer by the number of accumulations acquired. If each of the accumulations has light just below the saturation point to be summed the dynamic range of the accumulated signal is also increased by the number of accumulations.

### Smear

When a interline-transfer-CCD image sensor is readout the generated charge carriers are transferred from the light sensitive part (photodiode) of a pixel to the shift register. This is located next to the photodiodes and acts like a potential bucket. As there is weak light sensitivity on these shift registers, they are shaded to prevent the additional generation of charge carriers. When the charge transfer to the shift register is complete, they are vertically shifted, row-by-row, to the horizontal readout line, which is then read out serially. This row-by-row vertical shifting is comparable to an endless conveyor belt. With every shift step, all registers are shifted by one register location, including those register rows that were previously drained from the image.

If an intense light source is imaged onto the CCD image sensor, this can generate unwanted charge carriers in the shielded shift registers (mainly due to the scattering of light on the CCD chip) in every line or row that is shifted below the spot. This results in additional unwanted light signals called "smear" (Figure A.12 ).

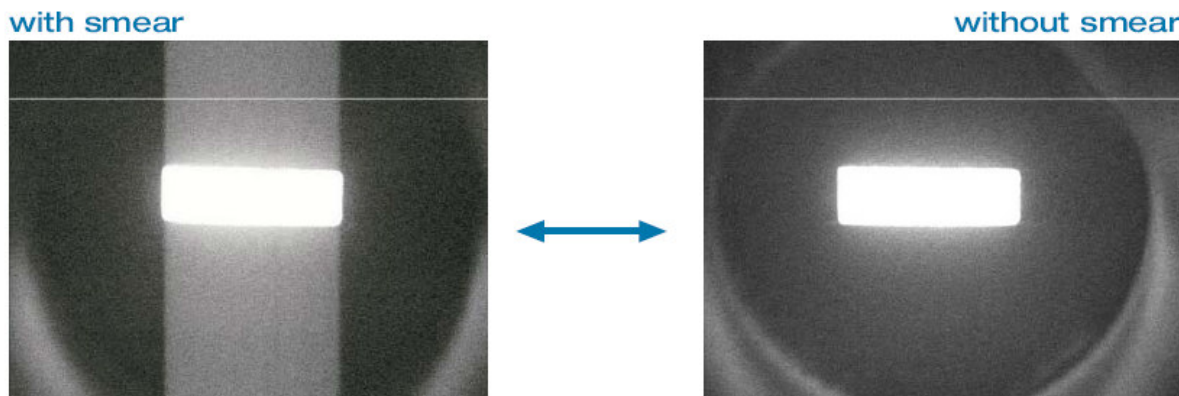


Figure A.12

Smear can be recognized as bright vertical bands below and/or above the bright image spot (interline or frame transfer architecture). Smear is dependent on the high intensity, therefore short exposure time, high intensity, more smear, while long exposure time, low intensity, less smear. Depends also on the image sensor read out time or speed, so slow readout, more time for smear, while fast readout, less time for smear

## Signal/Noise Ratio

A related measurement to sensitivity and noise is the signal to noise ratio. It is defined as the ratio of the light signal to the sum of noise signals and it is expressed as a ratio or factor in units of decibels [dB]:  $\text{ratio}[\text{dB}] = 20 \log[\text{ratio}]$ . Let's consider the theoretical prediction of signal to noise for a typical camera. If we assume we have a number of photons  $P$  falling on a camera pixel with a Quantum Efficiency  $D_{QE}$  this will generate a signal of  $N_e$  electrons as below:

$$N_e = D_{QE}P$$

The incoming photons have an inherent noise  $\sigma_{\text{signal}}$  known as photon shot noise and, as the photons follow Poisson statistics, this is the given below:

$$\sigma_{\text{signal}} = \sqrt{D_{QE}P}$$

The other noise sources are:  $\sigma_{\text{readout}}$  is the readout noise,  $\sigma_{\text{dark}}$  is the noise resulting from thermally generated electrons (so called dark signal), and  $\sigma_{\text{signal}}$  is the noise generated by the photon signal. Putting these terms together we can then generate an expression for the signal to noise ratio for a typical camera.

$$S/N = D_{QE}P / \sqrt{(\sigma_{\text{signal}}^2 + \sigma_{\text{dark}}^2 + \sigma_{\text{readout}}^2)}$$

Substituting for the expressions for noise we can see the equation for signal to noise is as follows:

$$S/N = D_{QE}P / \sqrt{(D_{QE}P + N_{\text{dark}} + \sigma_{\text{readout}}^2)}$$

The thermal noise component  $N_{\text{dark}}$  is a function of temperature and exposure time and in the limit where the exposure time is very short and the CCD is cooled to a low temperature this term is negligible.

It can be seen by manipulation of the equation that the signal to noise ratio approaches that of an ideal detector in the situation when light signal is high so that the shot noise is predominant with respect to readout noise and dark noise:

$$D_{QE}P \geq \sigma_{\text{readout}}^2 + N_{\text{dark}}$$

which can be rearranged thus:

$$P \geq (\sigma_{\text{readout}}^2 + N_{\text{dark}}) / D_{QE}$$

Expressing the photon number impinging on CCD as

$$P = \Phi t A / h\nu$$

where  $\Phi$  is the light power [ $\text{W}/\text{m}^2$ ],  $h\nu$  the photon energy [ $\text{Ws}$ ],  $t$  the time exposure [ $\text{s}$ ] and  $A$  the pixel area [ $\text{m}^2$ ], we see that to achieve a good SNR high QE, large pixel area, small readout and dark noise are all desirable.

## Spatial Resolution

The resolution of a CCD is a function of the number of pixels and their size relative to the projected image. CCD arrays of over 1,000 x 1,000 sensors (1 Mega-pixel) are now commonplace in scientific-grade cameras. The trend in cameras is for the sensor size to decrease, and cameras with pixels as small as 4 x 4 microns are currently available in the consumer market. Before we consider the most appropriate pixel size of a particular application, it is important to consider the relative size of projected image to the pixel size to obtain a satisfactory reproduction of the image.

Consider a projected image of a circular object that has a diameter smaller than a pixel (Figure A.13). If the image falls directly in the centre of a pixel then the camera will reproduce the object as a square of 1 pixel. Even if the object is imaged onto the vertices of 4 pixels the object will still be reproduced as a square, only dimmer – not a faithful reproduction. If the diameter of the projected image is equivalent to one or even two pixel diagonals the image reproduction is still not a faithful reproduction of the object and critically varies on whether the centre of the image projection falls on either the centre of a pixel or at the vertex of pixels. It is only when the object image covers three pixels do we start to obtain an image that is more faithfully reproduced, and clearly represents a circular object. The quality of the image is also now independent of where the object image is centered, at a pixel center or at the vertex of pixels.

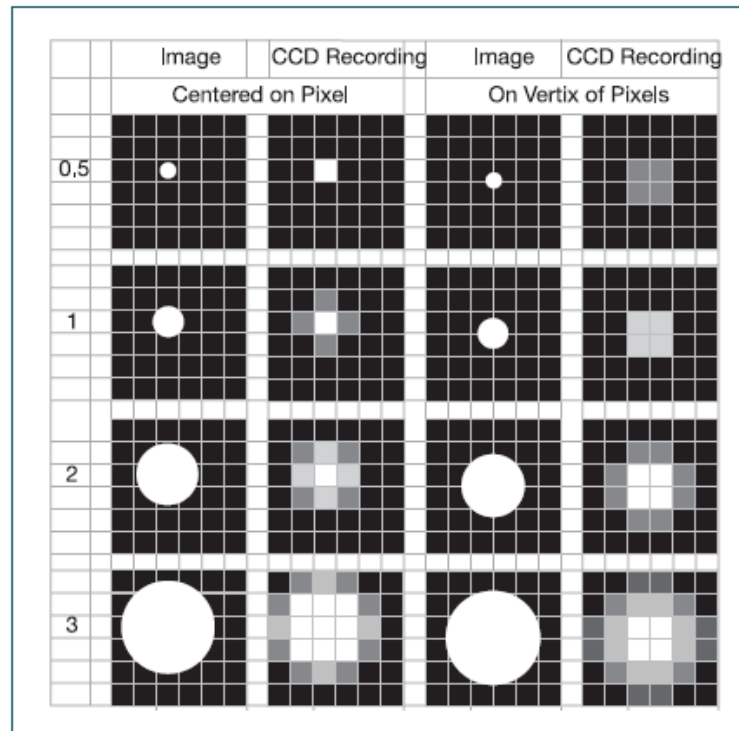


Figure A.13 CCD output patterns

In addition to the discrete pixels, other factors such as the quality of the imaging system and camera noise all limit the accurate reproduction of an object. The resolution and performance of a camera within an optical system can be characterized by a quantity known as the modulation transfer function (MTF), which is a measurement of the camera

and optical system's ability to transfer contrast from the specimen to the intermediate image plane at a specific resolution. Computation of the MTF is a mechanism that is often utilized by optical manufacturers to incorporate resolution and contrast data into a single specification. This concept is derived from standard conventions utilized in electrical engineering that relate the degree of modulation of an output signal to a function of the signal frequency (Figure A.14).

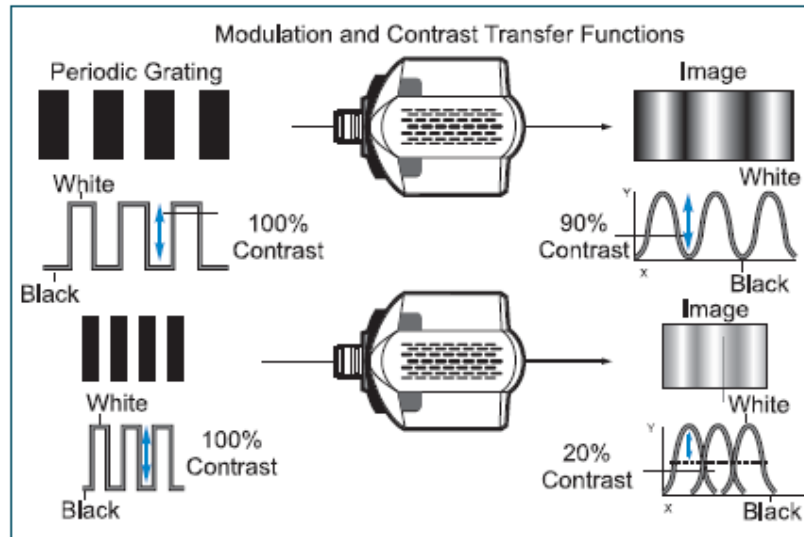


Figure A.14 Measurements of MTF

Adequate resolution of an object can only be achieved if at least two samples are made for each resolvable unit (many investigators prefer three samples per resolvable unit to ensure sufficient sampling). In the case of the epi-fluorescence microscope, the resolvable unit from the Abbe diffraction limit at a wavelength of 550 nanometers using a 1.25 numerical aperture lens is 0.27 microns. If a 100x objective is employed, the projected size of a diffraction-limited spot on the face of the CCD would be 27 microns. A sensor size of 13 x 13 micron pixels would just allow the optical and electronic resolution to be matched, with a 9 x 9 micron pixel preferred. Although small sensors in a CCD improve spatial resolution, they also limit the dynamic range of the device.

### Frame Rate

The frame rate of a camera is the fastest rate at which an image or spectra can be continuously recorded and saved. Frame rates are governed principally by the number of pixels and the pixel readout rate but other factors such as whether a sub array is used, whether there is binning and at which vertical shift clock speeds are also factors. Digital cameras can readout sub sections of the image or bin pixels together to achieve faster readout rates, therefore typically two frame rates are defined, i.e. one is a full frame readout rate and the other is the fastest possible readout rate.

### Binning

CCD's are very versatile devices and their readout pattern can be manipulated to achieve various effects. One of the most common effects is binning. Binning allows charges from adjacent pixels to be combined and this can offer benefits in faster readout speeds and improved signal to noise ratios, albeit at the expense of reduced spatial resolution.

To understand the process, let's compare the process of single pixel readout versus  $2 \times 2$  binning shown in the successive Figures A.15, when on the left side is showed a single pixel case and in the right side the binned case. If we consider a spot of light evenly illuminates the four pixels of our miniature CCD. The CCD has a light sensitive region of just four pixels and a readout register depicted in blue at the bottom of the CCD. The light signal induces a charge of 20 electrons in each of the four pixels as shown by their shading and the numbers in the bottom right hand corner of the pixel. The light falls evenly on the four pixels and creates a charge of  $20e$  in each of the four pixels.

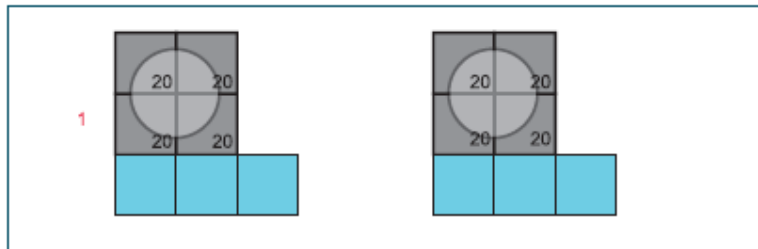


Figure A.15.1

The first operation is to shift the charge down one row. The charge from the lowest pixels gets shifted into the readout register.

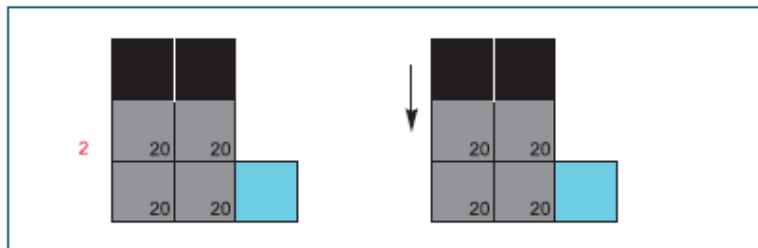


Figure A.15.2

For single pixel readout, the charge in the readout register is shifted to the right and into the readout amplifier. In the binning operation the charge is shifted down again and the charge from the second row is added to the first row in the readout register.

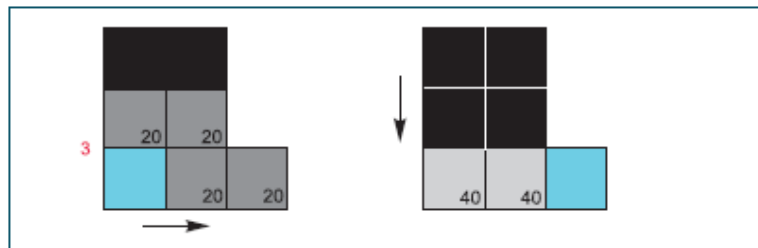


Figure A.15.3

For single pixel readout, the first pixel is readout while the readout register is shifted again to shift the charge in the second pixel into the readout amplifier. In the binning operation the summed charge from the two right pixels is shifted into the readout amplifier.

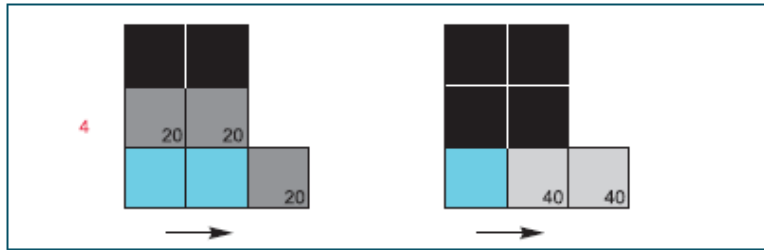


Figure A.15.4

In the single pixel readout, the next row is shifted vertically into the readout register. In the binning operation the readout register is shifted again to sum the charge from the 4 pixels in the readout amplifier before being readout.

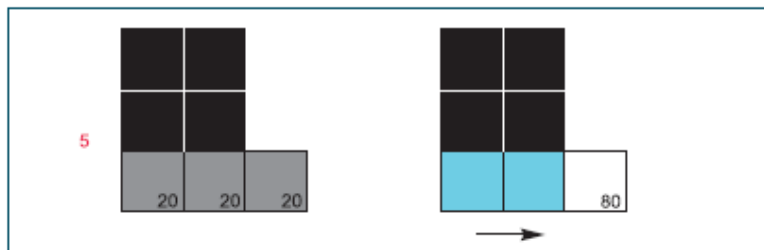


Figure A.15.5

In the single pixel readout mode, the readout register is shifted to the right again to readout the next pixel. Binned operation is now complete.

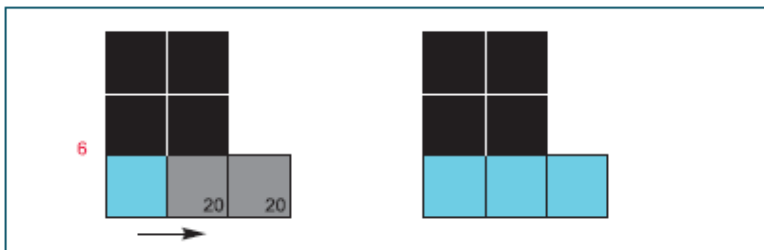


Figure A.15.6

In the single pixel readout the readout register is shifted to the right again to readout the final pixel.

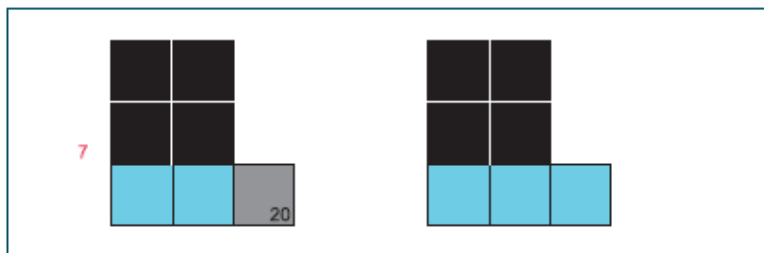


Figure A.15.7

It is important to highlight the main differences in the two readout schemes. In the first we achieve the full spatial resolution the sensor offers. In the binned example we have

reduced the 4 pixel pattern to a single pixel and hence lost spatial resolution. However the binned operation takes less steps to readout the sensor and hence is faster. Typically binning 2x2 is twice as fast; this is achieved by having to shift the readout register only every 2 vertical shifts. If we were binning 3x 3 or 4x4 on a CCD then the readout would be respectively 3 and 4 times faster.

The binned example also highlights how binning improves signal to noise ratio. If we assume our CCD has a readout noise of  $10e$  then in the single pixel example each pixel is readout with a noise of  $10e$  hence we achieve a signal to noise ratio of 2:1 ( $20e/10e$ ). Even if we subsequently sum the four pixels in a computer after readout, the signal-to-noise ratio becomes 4:1. In adding the four pixels we sum the signal (4 times  $20e$  i.e.  $80e$ ) and the noise is added in quadrature i.e. square root of the sum of the noises squared (square root of 4 times  $10$  squared i.e.  $20e$ ). In the binned example there is no noise until the signal is readout by the amplifier so the signal to noise ratio is 8:1( $80e/10e$ ) i.e. twice as good as the single pixel readout mode.

It is noteworthy that the binning reduces the detectable amount of light per pixel; however, in the majority of existing CCD image sensors, the serial shift and summation point register before the A/D conversion have enough capacity to accumulate charge carriers that are twice as large, compared to the full-well capacities of each pixel.

Binning is primarily used for low light level applications and for configured CCD image sensors where the readout noise (mainly in cooled CCD image sensors) is dominant, since other noise contributions such as dark current accumulate with binning.

### **Blemishes & Non-uniformities**

All cameras to some degree exhibit blemishes which impair the faithful reproduction of the light signal. The primary source of the blemishes is the sensor itself and here are some of the blemishes that occur.

#### **Black Pixels**

Black pixels are regions of the sensor, typically pixels or small clusters of pixels, which have significantly lower response than their neighbors (less than 75% the response of the average pixel). They are typically formed due to contamination on the sensor surface or embedded in the sensor. The effect of black pixels can be removed by taking a flat fielding reference or by post processing interpolation to mitigate their effects. Black pixels are rarely a major issue unless they extend to many pixels.

#### **Hot Pixels**

Hot pixels have a much higher dark current than their neighbors (50 times higher than specification). They typically have a different temperature response than the bulk of the sensor and so can appear to differing amounts at different temperatures.

They are usually due to contamination embedded in the sensor.

The effect of hot pixels, unless they are particularly large, can usually be removed by taking a background.

#### **Column Defects**

A combination of blemishes may adversely affect a column. A column defect may be due to some of the following:

- A total of more than 30 black pixels or hot pixels

- Hot Column: a column which has a dark current greater than 2 times specification
- Black Column: a column which has saturation less than 90% of the average column
- A trap: see next section

### Traps

Traps are peculiar to CCD's, they usually only occur in a single pixel and they can be caused by contaminants getting into the CCD during the production process or by the effects of radiation on the CCD structure. They act by becoming temporary holders of charge. As charge is shifted through a trap, the trap holds onto a portion of the charge (the trap size); while the trap is filled subsequent charge transfers are unaffected. The charge in the trap slowly dissipates until it is refilled by new charge created by illumination or by new charge being shifted through the pixel. Traps can be any size even down to a single electron charge trap but they are usually only noticeable when their size is greater than 200 electrons. Traps are identified by analyzing their impact on an illuminated CCD at a mixture of high and low light levels. The dynamic nature of the traps is difficult to model and therefore they are difficult to compensate for. Severe traps can be overcome by providing an initial light illumination to fill the traps before the proper exposure is required, but this adversely affects the signal to noise ratio.

# Chapter 4

## *HP-FRI in vivo on small animals: early tumor detection*

### *4.1 Introduction*

In this chapter we present the procedures and the results relative to HP-FRI measurements *in vivo* on small animals performed in the second part of our work. They contain the most important results both for implementation technical of the FRI system and the obtainment of the biomedical target of interest.

The second part of our work starts with the acquisition of a new CCD camera, Hamamatsu ORCA 285, an instrument of low noise, high sensibility, spatial resolution, dynamic range and quantum efficiency in the spectral region of our interest. As mentioned above, especially the CCD camera high sensibility is of fundamental importance in the FRI measurements. First, we calculated the spatial resolution of our FRI system with ORCA camera. Then we image different types of tumor (mammary, thyroid anaplastic and papillary), using also different collection geometry of fluorescent light (simple lenses system or stereomicroscope).

Exploiting the high sensibility feature of the ORCA camera, the submillimetric spatial resolution of our FRI system and the HP uptake selective in the tumor tissues, we have set as biomedical target the early detection of high malignancy tumor, i. e. the detection of tumor *in vivo* on mice in an early stage of its development. It is noteworthy that in the previous tumor detection by HP-FRI measurements, the dimensions of the studied tumors were about 50-400 mm<sup>3</sup>, so that the tumor masses were visible to the naked eye and palpable. Instead, it is crucial in the tumor diagnostic to be able to detect the tumor formation: earlier diagnosis greater the patient survival probability, especially if the tumor is highly invasive, as it is the ARO tumor. So, after a positive preliminary HP-FRI measurement on one mouse 6 h after HP injection and five days after ARO tumor cells inoculation, we performed HP -FRI measurements daily for 5 day on a set of 10 mice from the third day after ARO tumor cells inoculation and 6 h after HP injection; we repeat this series of HP-FRI measurements after a second HP injection the eighth day from tumor cells inoculation.

### *4.2 Experimental set-up*

In the second part of the work the experimental apparatus for FRI measurements (Figure 4.1) was so composed:

- Excitation source, a frequency doubled mode-locked active-passive Nd:YAG laser ( $\lambda = 532$  nm, beam diameter = 7 mm, energy/pulse = 30 mJ, pulse width = 50 ps, repetition rate = 10 Hz), or tungsten lamp with fiberoptic illuminator;
- optics for the collection of the excitation radiation on the sample: an iris diaphragm, a beam enlarging lens, a flat mirror directing the beam on the mouse surface;
- sample, a tumor bearing anesthetized mouse;
- optics for the collection of the fluorescence emission radiation in two alternative modalities: *a*) relay positive lenses and by the CCD camera equipped with a 16 mm lens (field of view (FOV)  $\approx 5 \times 4$  cm<sup>2</sup> or  $13 \times 10$  cm<sup>2</sup> on the animal body) (not shown in Figure 4.1)); *b*) a stereomicroscope at 1.3X (FOV  $\approx 1.1 \times 0.9$  cm<sup>2</sup>, resolution  $\approx 120$  pixel/mm) (Figure 4.1).
- cut-on long wave pass filter (Andover 600FH90-25, cut-on wavelength: 600 nm).
- detector, a CCD camera (Hamamatsu ORCA 285 G), equipped with a Computar 16 mm objective;
- image acquisition (average of 10 single frame consecutive acquisitions) and analysis board, a Hamamatsu Wasabi software.
- Offline image analysis software ImageJ.

The main features of the new CCD camera are:

- High resolution of 1.37 million pixels (1344×1024 pixels; cell size: 6.45µm; horizontal size: 8.67mm, vertical size: 6.6mm);
- A/D converter at 12 bit;
- Readout noise: 8 electrons r.m.s;
- Dark current: 0.8e<sup>-</sup>/pix/s;
- Full well capability (typical): 18000 e<sup>-</sup>
- Amplification gain conversion coefficient 4.6 electrons/ADC counts;
- Camera gain between 0 (0 dB) and 255 (20 dB);
- Exposure time from 10 µs to 10 s;
- Peak quantum efficiency (60%) at 500 nm (Figure 4.2 left side);
- Progressive scan interline CCD chip without mechanical shutter;
- About 10 µs electronic shutter to capture fast events;
- Binning 2x2, 4x4, 8x8 function to improve sensitivity and achieve a frame rate of 16, 27, 41 Hz respectively;
- Dynamic range (typical): 2250:1;
- Low dark noise with Peltier cooling (cooling temperature: +5 °C) for a dynamic range of more than 60 dB;
- Full remote control from PC via IEEE 1394 bus<sup>7</sup>;
- Camera head weight: 1.3 Kg.

---

<sup>7</sup> The Firewire interface was developed by Apple Computers in the mid 1990's and was adopted by the an independent trade association called the 1394 Trade Association after the IEEE 1394 computer interface standard. Firewire can be operated as a synchronous device which allows high speed bandwidth for short periods of time.

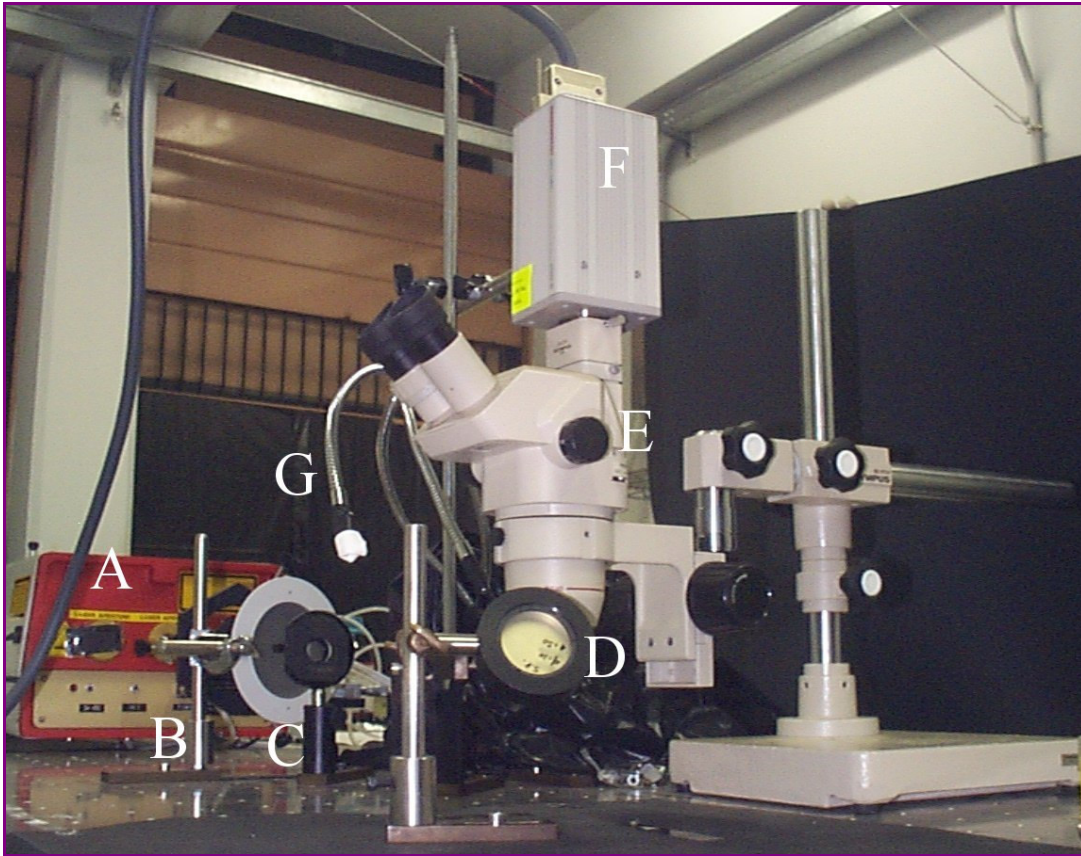


**Figure 4.1:** A: Frequency doubled pulsed Nd:YAG laser ( $\lambda = 532$  nm, energy/pulse = 30 mJ). B: Iris diaphragm C: Beam enlarging lens D: Flat mirror E: Stereomicroscope (Olympus SZ-40) at 1.3 X F: Cooled CCD monochrome digital camera (Hamamatsu ORCA 285 G) equipped with cut-on long-wavelength pass filters ( $\lambda > 600$  nm) G: Tungsten lamp with fiber optic illuminators.

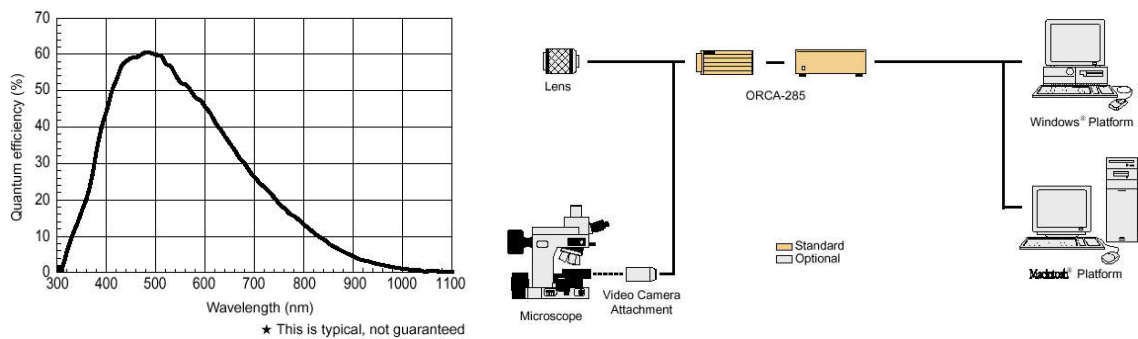


**Figure 4.2** Sensitivity spectrum (left side) and system configuration of our CCD camera Hamamatsu Orca 285 (right side).

### 4.3 Materials and methods

#### a. Spatial resolution measurements

In order to estimate the spatial resolution of our *in vivo* imaging system, we used a borosilicate glass capillary (5  $\mu$ L volume, nominal external and internal diameter of 1 mm and 260  $\mu$ m, respectively), filled with HP solution and inserted *post mortem* under the skin of a sacrificed mouse. The HP concentration was reduced 1:4 with respect to that used for the successive HP-FRI measurements. About 15 mm of capillary length was inserted under the skin. Before inserting it, we imaged by fluorescence about 25 mm of capillary length in air. We observe explicitly that in this manner the fluorescent source is placed at the same depth (about 1 mm under mouse skin) as the tumors we image.

### ***b. The new in vivo HP-FRI modality***

The dose of 400  $\mu$ l of aqueous solution of HP dichlorohydrate (Vit-porphyrin II, Teofarma, Italy), at the concentration of 4 mg HP/ml distilled water, corresponding to a dose of 28 mg HP/Kg mouse body weight, was injected *im* in the right posterior leg of the mouse, on the opposite side with respect to the tumor.

As in the previous experiments, we used six-week-old Crl:CD-1 athymic nude mice (Charles River Laboratories, Calco, Italy).

The tumor cell lines subcutaneously inoculated in the mice are: i) MDAMB361 cells (for brevity, MDA cells), derived from a mammary human carcinoma; or ii) ARO cells, derived from an anaplastic human thyroid carcinoma. Cells were cultured in Dulbecco's Modification of Eagles' Medium (DMEM) culture medium supplemented with 10% fetal calf serum, penicillin (50 U/ml) and streptomycin (50 g/ml). About  $10^7$  cells were injected in the back of the mice and the *in vivo* FRI measurements were performed 30-31 days later and from 6 h up to 30 h after the HP injection. Ten minutes before measurements, the animal was anaesthetized by injecting 300  $\mu$ l of a solution obtained by dissolving, in 20 ml physiological solution (NaCl 0.9% water solution), 0.5 ml of a solution of tribromoethanol (Avertin) in 2-metil-2-butanol at the concentration of 1 mg/ml.

We have imaged two MDA tumor bearing mice, called mouse  $\alpha$  and  $\beta$  with system lenses (FOV: 13 $\times$ 10 cm<sup>2</sup> and 5 $\times$ 4 cm<sup>2</sup>, respectively), and one ARO tumor bearing mouse, called mouse  $\gamma$  with stereomicroscope (FOV: 1.1 $\times$ 0.9 cm<sup>2</sup>).

In this new FRI apparatus, the measurements protocol includes in the red light image and fluorescence image. The first is obtained by white light illumination (fiberoptic illuminator, 50 W tungsten lamp, G in the Figure 4.1) and with the cut-on filter ( $\lambda > 600$  nm) in front of the CCD, showing visually the position and the dimensions of the interesting structures on the animal. The second image offers the map of the fluorescence emission registered with an exposure time ranging from 5 s to 10 s and a camera gain between 50 and 120. Hence, the exposure time corresponds to 50 or 100 laser pulses per image. In order to compare images with different gain and exposure times the image data matrix (pixel values) was suitably scaled. Furthermore, to each image we have subtracted the CCD camera background noise image (including readout noise), acquired in the dark (with diaphragm closed and minimum (zero) time acquisition and zero gain). We outlined that in these FRI measurements the image of laser beam 2-D profile at 532 nm doesn't is acquired, because we can infer from the previous measurements that the laser fluctuations don't affect significantly the imaging quantitative determinations when the image is the result of a media on numerous (>30) consecutive acquisitions, as it happens in our case. All the images are acquired as 12 bit images, but are represented here as 8 bit images.

Immediately after *in vivo* fluorescence imaging measurements, the two MDA tumor bearing mice were sacrificed and histological sections were obtained from tumor tissues.

### *c. Early tumor detection*

The HP dichlorohydrate (Sigma, Italy) dose, modality and localization on the mouse and mouse type are the same than the previous point *b*.

We have used the ARO tumor cells because of their high degree of malignancy that justifies the necessity of early detection. The doubling time *in vitro* of this cell line is approximately 20 h.

As preliminary experiment, we considered only one mouse, called mouse #0. The fluorescence measurements were performed the fifth day after the  $10^6$  cells injection, and after 6 h from HP injection. The mouse was also imaged five days after the tumor cell injection but before the fluorescent marker injection, in order to provide a control image. The animal was anaesthetized by injecting 50  $\mu$ l of a solution of chloral hydrate 10 mg/ml in NaCl 0.9%. The measurements protocol is the same than the previous point *b*.

Then, we have imaged 10 mice ARO tumor bearing numbered from 1 up 10. The camera lens provided a field of view of  $10.2 \times 7.8$  cm<sup>2</sup> in order to view the whole mouse body. The fluorescence measurements were performed the third day after the cell injection, and after 6 h from HP injection and repeated daily in the successive four days. The eighth day after cells inoculation a second HP injection (with the same dose of the first) was done and a second set of FRI measurements was performed identical to the first. Some mice dead before the performing all measurements.

Fluorescence images, all visualized using the same gray level scale, were processed according to the steps illustrated in the point *b*. Furthermore, the fluorescence intensity profile along a straight line across the fluorescent tumor area was determined, the constant grey level,  $I_0$ , for the healthy tissue surrounding the tumor and the maximum gray level,  $I_{\max}$ , in the fluorescent tumor region were determined, and the maximum optical contrast Tumor/Background (T/B) ratio was calculated as  $I_{\max}/I_0$ .

## **4.4 Results and their discussion**

### *a. Spatial resolution measurements*

The Figure 4.3 shows the line profile of the fluorescence image (drawn across the capillary diameter and integrated along a length of the capillary of the about 15 mm) of the HP filled capillary in the air (left side) and under mouse skin (right side). In the former case, the line profile present a Gaussian shape with a FWHM value of  $240 \pm 20$   $\mu$ m, in accordance with the nominal internal diameter of the capillary, while in the latter case the FWHM value increase up to  $770 \pm 20$   $\mu$ m, due to the light scattering effects by the mouse skin. By subtracting in quadrature the FWHM value measured in air, we obtained a value of  $730 \pm 30$   $\mu$ m for the FWHM system resolution estimated for our *in vivo* fluorescence imaging system.

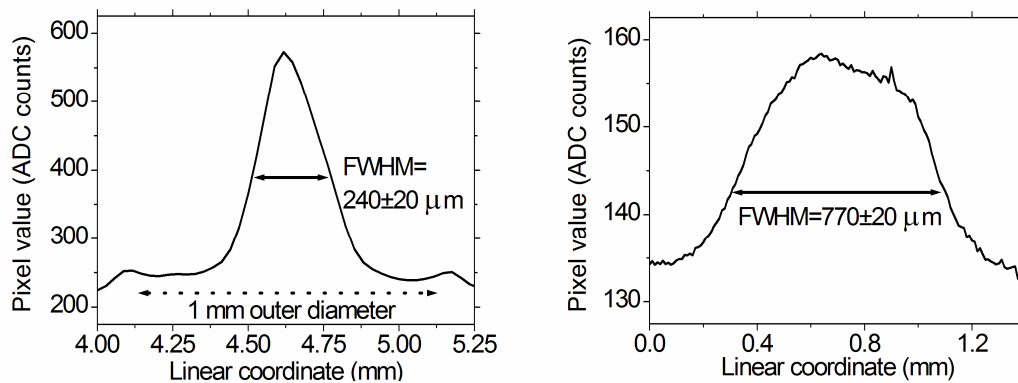
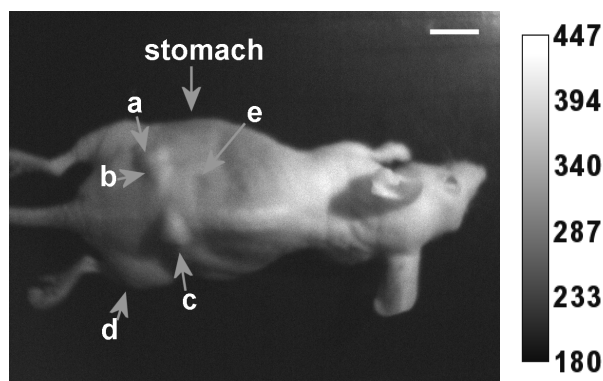


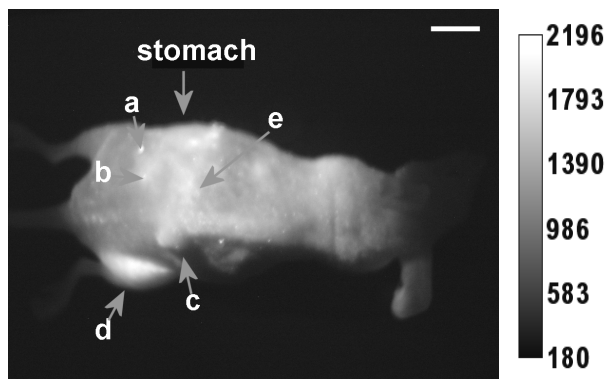
**Figure 4.3.** Fluorescence intensity profile across the diameter of a capillary filled with HP solution in air (left side) and then inserted under the mouse skin (right side); the relative FWHM value with their error are also reported. The profiles have been integrated for a length of several mm along the capillary (see text). In the top figure, the capillary tube walls are evident, as small peaks at about 1 mm distance, ascribed to the effect of internal diffuse reflection of fluorescence light at the glass-air interface.

### *b. The new in vivo HP-FRI modality*

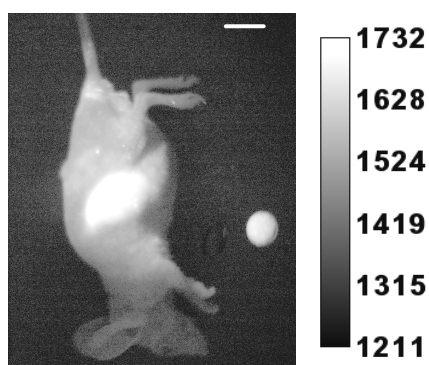
The mouse  $\alpha$  with a mammary MDA tumor, as observed in red light, shows three small tumors (*a*, *b* and *c*) on the back (Figure 4.4, top side). The corresponding HP fluorescence image (Figure 4.4, bottom side) shows the highly fluorescent HP injection site in the right posterior leg (detail *d*), and a diffuse fluorescence in the back with some brightest points which correspond to the tumor regions (*a*, *b* and *c*). Here, a fifth region (*e*), apparently a healthy area in the red light image and not correlated visually with any normal or tumor structure, presents an enhancement of fluorescence optical contrast with respect to the surrounding region. The histological analysis shows that this fluorescent region (*e*) corresponds to a tumor region. Thus, the features of our HP-FRI system allow us the detection of tumor area apparently healthy. We could talk of reduction of false negative, also if improperly, because referred to an unique case.

The mouse shows also a fluorescent region on the left flank in a rough anatomical correspondence with the stomach (Figure 4.5).



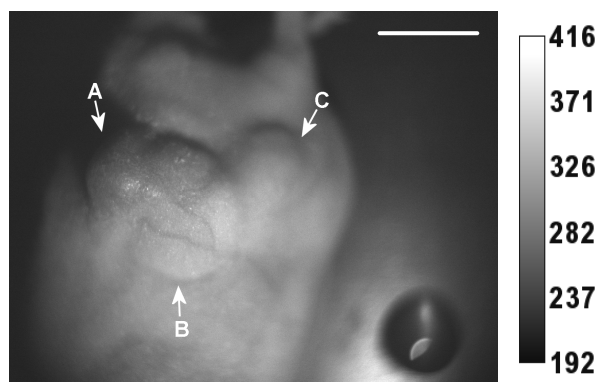


**Figure 4.4.** (Top) Red light image (exposure time 200 ms, gain 50) of the tumor area of mouse  $\alpha$  showing the three tumor masses marked as a, b, c. The fluorophore injection site is marked as d. The fifth fluorescent region (e) doesn't correlate visually with any normal or tumor structure. (Bottom) Fluorescence image (exposure time 10 s, gain 50) of the whole mouse. The horizontal white bar corresponds to 1 cm.



**Figure 4.5.** Fluorescence image (exposure time 10 s, gain 50) of the mouse # 2, 24h after HP injection. Here the image was plotted in logarithmic scale to show the correspondence of the fluorescent region with the mouse stomach location. The circle on the right is a fluorescent marker. The horizontal white bar corresponds to 1 cm.

The mouse  $\beta$ , bearing mammary MDA tumors, as observed in the red light (Figure 4.6, top), shows a tumor with three lobes; the two larger ones (A and B) are supposed, by visual inspection, in an advanced state of necrosis. The fluorescence image (Figure 4.6, bottom) confirms the finding of a tumor structure where two lobes (A and B) are less fluorescent with respect to the surrounding healthy tissues, and the last lobe (C) appears slightly fluorescent.



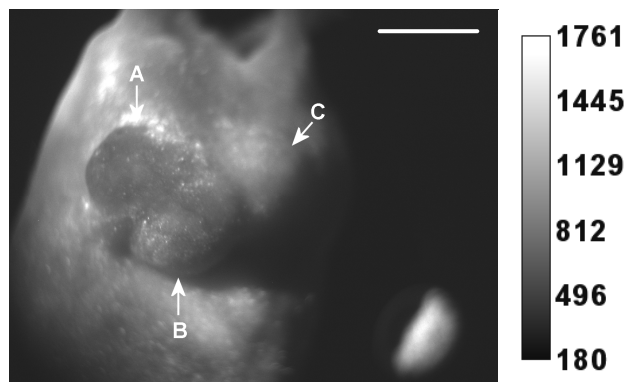


**Figure 4.6.** (Top) Red light image (exposure time 10 ms, gain 0) of the tumor area for mouse  $\beta$  showing the three tumor lobes marked as A, B, C. (Bottom) Fluorescence image (exposure time 10 s, gain 50) of the same tumor area. The horizontal white bar corresponds to 1 cm.

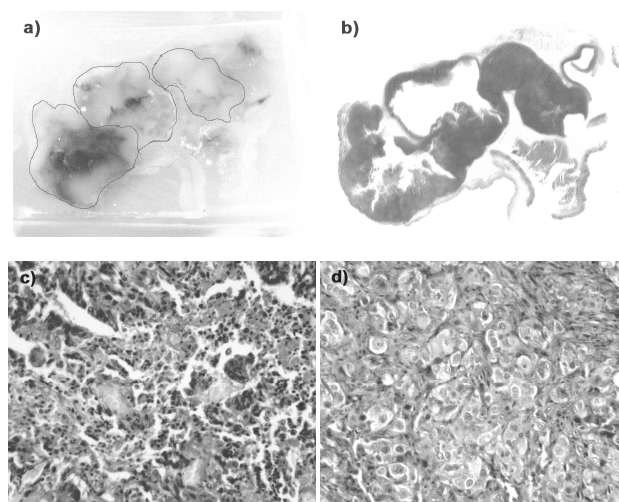


**Figure 4.7.** Macroscopic image of the tumor tissue of mouse  $\beta$ : a) paraffin inclusion of the whole tumor; b) histological section of the same region stained with hematoxylin - eosyn ; microscopic image of stained histological sections of lobe A showing damaged (necrotic, haemorrhagic) tumor cells (c) and viable tumor cells of lobe C (d). In a) the contours of the tumor lobes are roughly drawn.

The histological examination of this tumor biopsy (shown in paraffin inclusion and as a stained histological section in Figure 4.7 a and b, respectively) supports this conclusion. Indeed the micrographies of the tumor tissue of lobe A (Figure 4.7 c) and lobe B show damaged (necrotic, hemorrhagic) cells especially in the lobe central region, while the lobe C (Figure 4.7d) shows scarce necrosis and hemorrhagic phenomena and 1-2 mitoses per microscope field. The fraction of viable cells is approximately, 72%, 67% and 95 % for the lobes A, B, C respectively.

In conclusion, visually recognized tumor area does not fluoresce, while the histological analysis shows that the non-fluorescent tumor area is constituted of necrotic/hemorrhagic cells. We could so suppose that this tumor necrosis state prevents accumulation of the dichlorohydrate HP, as has been found for other HP compound.

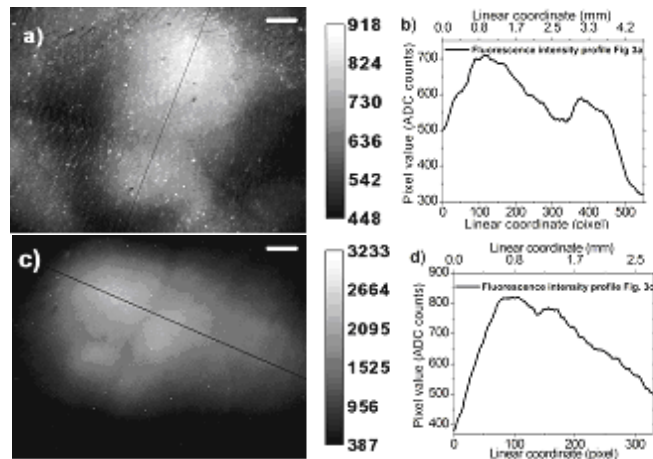


**Figure 4.8** Tumor (a) and healthy areas (c) fluorescence images for mouse  $\gamma$ . Plot represents profile in the tumor area (b) and in healthy areas (d) along the line drawn on the images. The horizontal white bar corresponds to 1 mm. Exposure time is 10 s; gain 120.

The mouse  $\gamma$  shows an ARO tumor region with a two lobes structure in the *in vivo* HP fluorescence image (Figure 4.8 a) acquired with the stereomicroscope (FOV of  $1.1 \times 0.9$  cm<sup>2</sup>). It is also possible to distinguish this structure from the fluorescence intensity profile along the line drawn across the tumor region (Figure 4.8 b), where the smaller lobe has a FWHM linear size of about 1 mm. In Figure 4.8 c (same FOV) is reported the HP fluorescence image of a region of the left flank of the same mouse corresponding to healthy tissue areas (intestinal tract). In the Figure 4.8 d the fluorescence intensity profile along the line drawn across this fluorescent region is showed. Hence, if the sensitivity and spatial resolution performances are combined with the magnification provided by the use of the stereomicroscope, some rough “structural features” can be visualized, as tumor lobes.

By these first *in vivo* HP-FRI measurements with the new apparatus, we can infer a series of observations about the system features. The high sensitivity of the new CCD camera and the higher dose of administered fluorescent marker with respect to the previous experiments allows the skin autofluorescence, red fluorescence of the skin when excited at 532 nm, and background fluorescence, due to the low accumulation of the exogenous HP in healthy tissues, to be detected. The detection of fluorescence skin has the advantage of providing the localization of the hyperfluorescent region on the mouse body and, however, doesn't prevent the detection of the tumor areas by an increased fluorescent contrast of the tumor area with respect to the healthy tissue. Indeed, the tumor area appears clearly more fluorescent than the surrounding healthy tissues. On the other hand, the resolution of the structures appearing both in tumors and organs fluorescence images is strongly affected by the high value of the scattering coefficient of the mouse skin, as it is note in literature and as it results also from our spatial resolution measurements. Finally, the tumor HP dichlorohydrate uptake is selective, although nonspecific and by mechanisms not absolutely understood, as explained in Chapter 2. Indeed, our HP compound allows for the fluorescent labelling of different tumor types (we have seen ARO and NPA, and now also mammary) for a diagnostic purpose, while doesn't allows for monitoring of molecular or genetic pathways of the diseases for a biomolecular study.

*c. Early tumor detection*

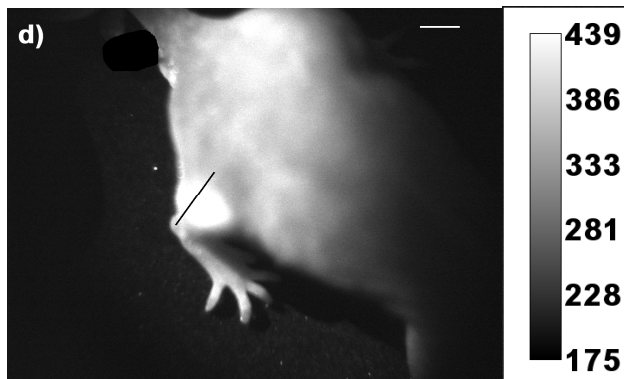
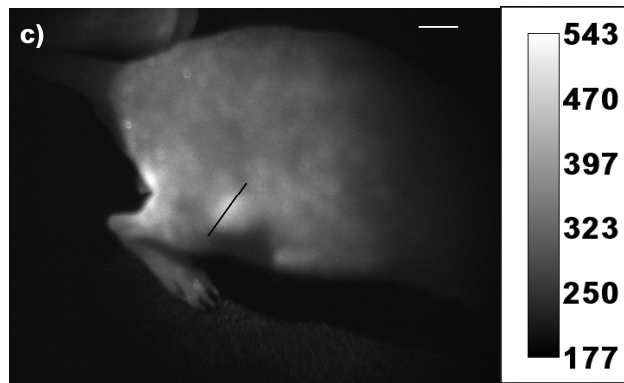
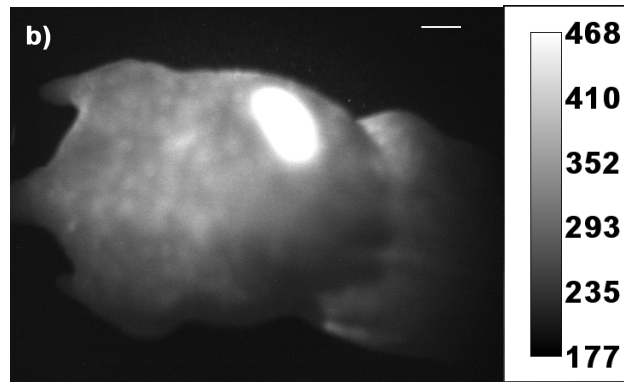
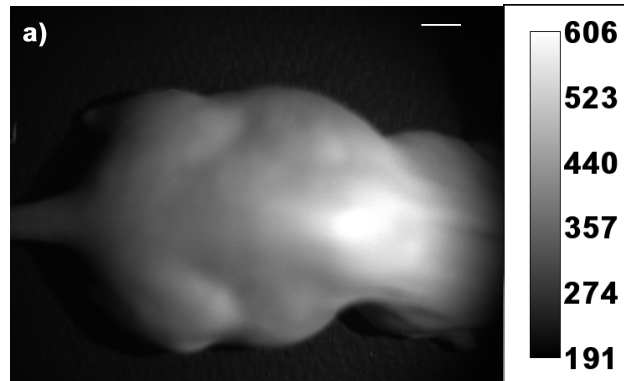


**Figure 4.9** Images of mouse #0. The mouse is imaged, before HP injection, in the red light (a), in the autofluorescence light (b and c) and, after HP injection, in the HP fluorescence light (d). The horizontal white bar corresponds to 1 cm. The black line across the suspected tumor region in c and d indicates the location of the fluorescence intensity profile reported in Figure 4.10. In red light image (a) exposure time: 1,5 s; gain: 0; in fluorescence images (b, c, d) exposure time is 10 s; gain 50.

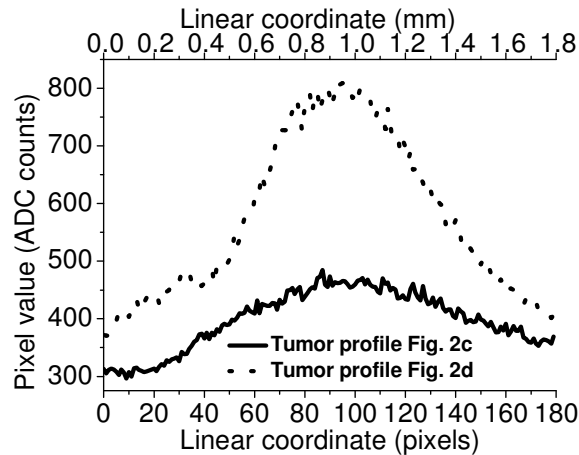


**Figure 4.10** Fluorescence intensity profiles of tumor area in Figure 4.9 c (solid black line) and in Figure 4.9 d (dotted line) along the lines drawn on the suspected tumor regions.

Figure 4.9 shows the sequence of *in vivo* images for mouse #0, corresponding to: whole mouse, back view, image in the red under white light illumination (Figure 4.9 a); whole mouse, back view, fluorescence image before HP injection (Figure 4.9 b); mouse flank with tumor, fluorescence image before HP injection (Figure 4.9 c); mouse flank with tumor, fluorescence image after HP injection (Figure 4.9 d). Hence, Figures 4b and 4c show the autofluorescence of the mouse, namely the red fluorescence of normal tissues when excited at 532 nm. Figure 4.9 d shows the increased fluorescence in selected regions on the mouse, due to the exogenous HP fluorescent marker, particularly in the tumor region.

In Figure 4.10 is plotted the profile of fluorescence intensity along the line drawn in mouse images Figure 4.9 c and Figure 4.9 d. The optical contrast, calculated as the ratio between the maximum and minimum value, is 1.6 for the tumor region in Figure 4.9 c and 2.2 in Figure 4.9 d.

Hence, the sensitivity and spatial resolution performances of the system allow for the detection of an early stage tumor, as the ARO tumor in Figure 4.9, implanted just 5 days before the fluorescence measurements. We can estimate that, starting from  $10^6$  injected cells, we have a number of ARO tumor cells of the order of tens of millions cells, corresponding to a volume of few cube millimeters. However, the tumor area appears clearly more fluorescent than the surrounding healthy tissues and the tumor tissue itself prior the HP administration. On the other hand, the relatively low fluorescence ratio tumor/healthy tissue due to the autofluorescence and/or fluorescence background remains one of the most limits to the detection sensitivity of the fluorescence systems.

We note also the bright spot appearing on the left flank of the mouse before HP injection (Figure 4.9 b), a fluorescence signal coming from a region corresponding to the mouse stomach. We have observed a single large fluorescence area located in the stomach region of the mice also in the Figure 4.5 and 4.8 b. Since this fluorescence appears also

without HP administration (Figure 4.9 b), we speculate that it could be due to the natural derivatives of Chlorophyll-a present in the mice food, whose fluorescence spectrum is similar to that of HP (241,242). Although it is generally recommendable to adopt for the mice a diet chlorophyll-free to avoid the presence of fluorescence signals “spurious”, in our work this organs fluorescence doesn’t affect the detection of the fluorescence of the tumor area, because the corresponding regions are well spatially separated. We note that the internal organs that, as tumor masses, are subcutaneous can be imaged by optical fluorescence since the radiation at the wavelength 530 nm has a penetration depth in tissues less than 1 centimeter (2,243).

It is distinguishable in the Figure 4.9 c and d a shadow, due to the fluorescence of the black cardboard under the mouse body.

Day after cells inoculation	$I_{max}/I_0$
1	1.58
2	1.38
3	1.21
4	1
5	1
6	
7	
8	1.28
9	1.35
10	1.33
11	1
12	1

**Table 1:** The values of the optical contrast of the tumor region with respect the surrounding healthy region are reported for the mouse #1 whose time sequence fluorescence images is showed in the Figure 4.11. The maximum optical contrast is obtained between 6-24 h after the first HP injection. After the second HP injection on the eighth day after tumor cells inoculation the optical contrast doesn’t reach values so high as after the first, although again it is higher in the first 24 h and decrease to unity the fourth day.

Figure 4.11 shows the time sequence of the red light (first column) and the corresponding fluorescence (second column) images of the mouse #1 for the first five days following the HP administration. In this measurements series it is provided that the position of the mice in the CCD camera FOV and with respect to irradiation geometry was about the same, so minimizing the signal fluorescence variations due to the not perfectly uniform irradiation distribution. On each fluorescence image a straight line was drawn under the right leg, where it is known that the tumor cells inoculation has been performed, along the region with increased fluorescence signal. It is to be noted that the tumor, in these first days after cells inoculation, wasn’t visible at naked eye: only a posteriori, when the tumor have developed, it was possible to verify that this region so individuated corresponded with the tumor. Along this line the tumor profile fluorescence intensity, showed in the third column, was determined. The fluorescence line profile across the tumor region exhibits the following features:

- a) constant level, corresponding to the fluorescence level of the healthy tissue;
- b) sharp peak of fluorescence, corresponding to the tumor region;

c) fluorescence quickly dropping, due to a geometric effect of the mouse body.

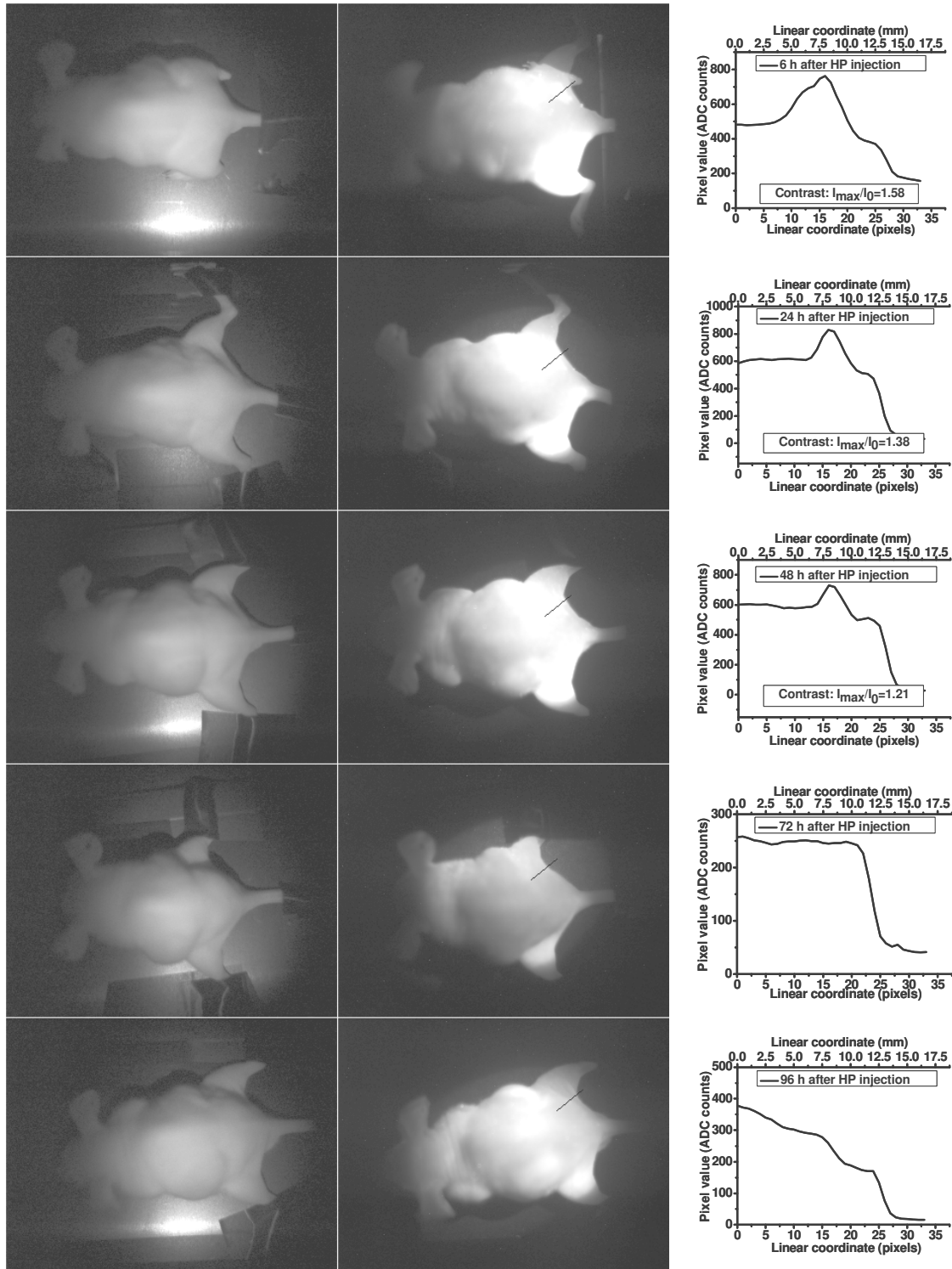


**Figure 4.11** Time sequence of the red light images (first column), corresponding fluorescence images (second column) and tumor profile fluorescence intensity (third column) of the mouse #1 for the first five days following the HP administration.

The constant grey level,  $I_0$ , for the healthy tissue surrounding the tumor and the maximum gray level,  $I_{max}$ , in the fluorescent tumor region were determined for all

measurements days and the optical contrast was calculated as the ratio  $I_{\max}/I_0$  and reported in the Table 1, from which we can observe that:

a) the contrast fluorescence ratio decreases with the increasing delay from the HP administration and vanishes after the third day from the first HP administration;

b) some other fluorescent regions are visible on the mouse body, corresponding to the HP injection site (left leg) and to some internal organs where HP accumulates as well;

c) the most suitable time to detect the fluorescence of the tumor is between 6 h and 24 h from the first HP administration;

d) the second HP administration on the eighth day after tumor cells inoculation doesn't allow returning of the optical contrast to the values obtained after the first HP injection;

e) again, also after second HP injection it can be seen that the optical contrast is higher in the first 24 h and it became unitary after the third day.

The control image of the mouse before HP injection indicates that fluorescence contrast between tumor and healthy region is absent (data not shown).

Again, we started from  $10^6$  injected cells, so we have imaged, at least in the first measurements day, tumors constituted by tens of millions ARO cells with a volume of few cube millimetres. From fluorescence imaging measurements we have estimated that the system resolution is about 700  $\mu\text{m}$  for imaging *in vivo* masses at about one millimeter below the mouse skin. Nevertheless, we investigated tumors whose dimensions are in the order of few millimeters. This is related to the biological difficulty of implanting a tumor by using a limited number of cells. In addition, in order to be sure of the effective tumor implantation, a delay of at least 3 days is normally required.

Hence, we showed that HP as a fluorescent marker is suitable for detecting the early stages of tumor development, provided that the imaging system has sufficient spatial resolution and photometric sensitivity to detect small tumors via their fluorescence. Nevertheless, this detection has characterized by a low optical contrast, as typically for the family of our fluorescent marker (see paragraph on porphyrins in the chapter 2). Moreover, it is limited to a time window of 48 h after the first HP injection and isn't repeatable after few days from the first HP injection, related to the different uptake and washout timings of the HP compound in the tumor and in the healthy tissue. Indeed, it can be inferred from our measurements that our HP compound accumulates in the tumor tissue preferentially with respect to the healthy, but with a washout time lower, so that some quantity of the HP compound remains in the healthy tissue also when it have been expelled from the tumor and it add itself to the HP administrated with the second injection.

The tumor early detection is a clinical requirement of primary importance. Many FRI techniques aim to this scope with different strategies for fluorescent labeling. In general, the specific or "smart" targeting can obtain information on molecular or genetic pathways of the oncological diseases, while the targeting with fluorescent protein can supply a high optical contrast also for diseased internal organs. In the first case (244, 245), it is required a large amount of work before the FRI measurements in order to obtain the fluorescent labeling through a biomolecular study that allows for the identification of the best combination between the fluorochrome and the specific ligands of the tumor cells. In the

second case (246-248) the fluorescence labeling of tumor cells is genetically performed before their injection, so that the tumor cells only are fluorescent. This approach does not allow to detect tumors that have unknown localization and nature.

#### 4.5 *Improvements and future project*

A number of improvements can be investigated for our optical *in vivo* imaging system for each component.

- Source: We are testing as excitation light source a 150 W halogen lamp with fiberoptic illuminator. This illumination system, indeed, is more compact and cheaper with respect to the picoseconds laser source, although it requires more stringent conditions on filter excitation that must excite the fluorochrome in a narrow wavelength band.
- Irradiation and collection geometry: we are testing a macroscope, a new Leica instrument, suitably designed for FRI measurements *in vivo* on small animals. The laser or lamp beam is fiber transported in the instrument and the FOV is continuously variable from few mm<sup>2</sup> to 20 cm<sup>2</sup> allowing for the whole animal imaging or zooming on a specific region.
- Fluorochrome: we have testing the FRI system with a fluorochrome of simple use like the HP compound, which allows for fluorescent labelling by a simple injection. Now we are ready to apply our FRI system on other type of fluorochrome. Also remaining in the porphyrin family, have been engineering a new generation of porphyrin encapsulated in nanostructures. In this manner the HP can behave as a specific fluorochrome. From the overview of the Chapter 2, it is clear that the possible biomedical applications are very numerous and interesting for the entire group of the molecular biology.
- Detector: new generation of CCD camera with an increased sensitivity in the red-NIR have been produced in the last years.
- External dark box: it can be added to the system in a form stable and of simple access to the sample and the other internal optical components.
- Methods to enhance signal/background ratio: methods able to reduce the negative incidence of the autofluorescence on signal/background ratio can be implemented by a digital subtraction procedure (249) as follows. First, two images are acquired, one with the background filter and one with the primary excitation filter. For both of these images, the same emission filter is used. The scale factor is a ratio of the autofluorescent signal measured using the background filter to the autofluorescent signal measured using the excitation filter. It accounts for different levels of tissue autofluorescence due to different excitation wavelengths and filter transmission characteristics. The scaled background image is subtracted from the primary excitation filter image resulting in a significant reduction in autofluorescence while leaving most of the fluorophore signal.  
Furthermore, free-chlorophyll diet for the mouse is to be adopted, to reduce the background fluorescence.

## 4.6 Conclusions

With the technological improvements carried out by ORCA CCD camera, we are handling with a modality imaging absolutely different with respect the previous. Indeed, we can reveal also the autofluorescence and fluorescence background of mice body: so we can obtain an immediate anatomical localization of the tumor region also in the fluorescence imaging, but we have also a lower optical contrast, since the not perfectly uniform irradiation doesn't allows for the digital subtraction operation we performed in our previous FRI measurements.

Nevertheless, we interrogate the HP-FRI system about the ability to detect tumor in an early stage obtaining positive response. The system, conjugating the HP selective tumor uptake and the high sensitivity, resolution spatial and photometric range of CCD camera, allows to detect tumor non visible at naked eye only three days after cells inoculation. However, this detection capability is limited to a temporal window of 48 h and to an optical contrast not very high ( $<2$ ); furthermore, this detection mode doesn't seem repeatable at brief temporal intervals. These features prevent this method to can be used to monitor the time evolution of a set tumor, but allows for an early detection tumor by a non toxic HP compound without photosensitization consequences.

# Conclusions

We have implemented a FRI system by using a non tumor-specific fluorochrome like a HP dichlorohydrate, a compound of porphyrins family, whose fluorescence emission has been excited by a laser source. The final scope of the work was the *in vivo* detection, possibly in an early stage, of subcutaneous solid tumor with high malignancy degree on small animals.

In the field of the FRI technique, HP-FRI is characterized from the use of a non specific fluorochrome. This type of compounds has been largely studied in the past years because of their tumor selective uptake, which has been exploited especially for photodynamic purposes. In the photodynamic therapy (PDT) the interest for porphyrin compounds is increased in the years producing a large number of new photosensitizers, the so called "second generation porphyrins", in the attempt of decreasing the photosensitization effects and allowing for a better therapeutic effect. Although the PDT is the main application of the porphyrin compounds, they have been applied also in the photodiagnosis (6).

As a first step in this research field, we implemented a FRI system as simple as possible from both instrumental and biological point of view. So we used a laser VIS light source, guaranteeing the high monochromaticity and power of the excitation light; a CCD camera with intermediate sensitivity; a non tumor-specific fluorochrome as a HP compound that doesn't require complicated fluorescence labeling procedures, but only its simple systemic injection as a water solution. It was shown that simple HP-FRI technique we developed is a useful tool for diagnostic purposes: it's able to image the fluorescence intensity increase in the region where tumor cells were inoculated and the tumor grows. The non-specific uptake of HP by tumor cells/tissue, while doesn't allow for monitoring of molecular or genetic pathways of the diseases for a biomolecular study, allows for the detection of different tumors with the same labeling procedure for diagnostic purposes.

Furthermore, we investigated the detectability of two different types of tumor, having different malignancy degree, with a bimodal system composed by our HP-FRI and a radionuclide imaging based on a semiconductor pixel detector of the Medipix family at high spatial resolution. So we were able to discriminate the different uptake of the gamma/fluorescent marker in the tumor.

Successively we improved the system detection by adopting a high sensitivity CCD camera, allowing for a more advanced imaging modality, where the detection of skin autofluorescence and background fluorescence has the advantage of providing the localization of the hyperfluorescent region on the mouse body and, however, doesn't prevent the detection of the tumor areas by an increased fluorescent contrast of the tumor area with respect to the healthy tissue. On the other hand, the resolution of the structures appearing both in tumors and organs fluorescence images is strongly affected by the high value of the scattering coefficient of the mouse skin, as it results also from our spatial resolution measurements. In addition, the HP compound was shown to be a suitable fluorochrome for the early tumor detection. Indeed, the cell injection region can be imaged by its fluorescence contrast already on the third day after the tumor cells inoculation, when the tumor is not distinguishable at naked eye, neither palpable. The tumor/background optical contrast is maximum between 6 h and 24 h after a first HP

injection. Then it decreases with the time so that the third day after HP injection it vanishes; again, it increases 6-24 h after a second HP injection, but with values lower than those reached after the first injection and, finally, vanishes once again. It can be hypothesized that the timing of HP uptake and washout is different for the tumor tissue with respect to the healthy one: the HP accumulates in the tumor tissue preferentially with respect to the healthy, but with a washout time lower, so that some quantity of the HP exogenous remains in the healthy tissue also when it have been expelled from the tumor and it add itself to the HP administrated with the second injection. Consequently, the background/tumor optical contrast is lower after the second HP injection than after the first.

The tumor early detection is a clinical requirement of primary importance. Many FRI techniques aim to this scope with different strategies for florescent labeling. In general, the specific or “smart” targeting can obtain information on molecular or genetic pathways of the oncological diseases, while the targeting with fluorescent protein can supply a high optical contrast also for diseased internal organs. In the first case (244, 245), it is required a large amount of work before the FRI measurements in order to obtain the fluorescent labeling through a biomolecular study that allows for the identification of the best combination between the fluorochrome and the specific ligands of the tumor cells. In the second case (246-248) the fluorescence labeling of tumor cells is genetically performed before their injection, so that the tumor cells only are fluorescent. This approach does not allow to detect tumors that have unknown localization and nature. The non specific HP targeting is simple to perform requiring only a systemic injection; the HP is non toxic and, in the doses we used, doesn't show photosensitization effects in mice; the HP is photobleaching resistant and chemically stable. The preferential accumulation in tumor after a systemic injection indicates that the HP compound is suitable in particular to the tumor early detection. Nevertheless, the optical fluorescence contrast remains low (<2) and the detection limited to a temporal window of about 48 h after the HP injection, that prevents from the monitoring the tumor time progression for long intervals.

The system is susceptible of a series of improvements concerning the compactness of the irradiation source, the control of the irradiation geometry, the sensibility of the CCD camera. It is suitable to other biomedical applications, as the detection of tumor progression, of metastases formation and dissemination, the efficacy test on anticancer drug, etc., changing the fluorochrome type, i. e. the targeting strategies. The FRI system is also suitable for the integration with radionuclide system imaging (250) since the optical and radionuclide modality supply complementary information on the fluorescently and radionuclide labeled biomedical targets, as our preliminary tests seem indicate.

## References

1. S. R. Cherry, In vivo molecular and genomic imaging: new challenges for imaging physics, *Physics in medicine and biology*, **49**, 13-43 (2004).
2. V. Ntziachristos *et al.*, "Fluorescence imaging with near-infrared light: new technological advantages that enable in vivo molecular imaging", *Eur. Radiol.*, **13** (1), 195-208 (2003).
3. C. Bremer *et al.*, Optical-based molecular imaging: contrast agents and potential medical applications, *Eur Radiol*, **13**, 231-243 (2003).
4. Ntziachristos V, Weissleder R Shedding light onto live molecular target, *Nature Medicine*, **9**, 1 (2003).
5. S. L. Jacques, Scott A. Prahl <http://omlc.ogi.edu/classroom/ece532/class3/index.html> Oregon Graduate Institute.
6. K. Berg *et al.*, Porphyrin-related photosensitizers for cancer imaging and therapeutic applications, *J of Microscopy*, **218**, 133-147 (2005).
7. S. Svanberg, *Atomic and molecular spectroscopy - Basic aspects and practical applications*, (Springer Verlag, Heidelberg, 2004).
8. D. Gust *et al.*, "The Photochemistry of Carotenoids - Some Photosynthetic and Photomedical Aspects," *Ann. N. Y. Acad. Sci.* **691**, 32-47 (1993).
9. K. Svanberg *et al.*, "Photodynamic therapy of nonmelanoma malignant tumours of the skin using topical delta-amino levulinic acid sensitization and laser irradiation," *British Journal of Dermatology* **130** (6), 743- 751 (1994).
10. W. Cheong *et al.*, A Review of the optical properties of Biological Tissues, *IEEE J. Quant. Elec.*, **26**, 2166- 2185 (1990).
11. T. Johansson, Applications of laser spectroscopy to analytical chemistry, environmental monitoring and medicine, Dissertation thesis, Lund Institute of Technology, Lund, Sweden, (2002).
12. C. E. Cooper *et al.*, The Noninvasive Measurement of Absolute Cerebral Deoxyhaemoglobin Concentration and Mean Optical Path Length in the Neonatal Brain by Second Derivative Near Infrared Spectroscopy, *Pediat. Res.*, **39**, 32-38 (1996).
13. J. M. Conway *et al.*, A new approach for the estimation of body composition: infrared interactance, *Am. J. Clin. Nutri.*, **40**, 1123-1130 (1984).
14. M. Cope, The development of a near infrared spectroscopy system and its application for non invasive monitoring of cerebral blood and tissue oxygenation in the newborn infant, Ph.D. thesis, University of London (1991).
15. A. J. Welch *et al.*, "Definitions and overview of tissue optics," in *Optical-thermal response of laser-irradiated tissue*, A. J. Welch, M. J. C. van Gemert, Eds., pp. 15-46, Plenum Press, New York (1995).
16. A. M. K. Enejder, "Light scattering and absorption in tissue - models and measurements," *PhD thesis*, Department of Physics, Lund Institute of Technology, Lund University, Lund (1997).
17. A. C. Guyton, *Textbook of medical physiology*, W. B. Saunders Company, Philadelphia, London, Toronto, Montreal, Sydney, Tokyo (1991).
18. R. M. P. Doornbos *et al.*, "The determination of *in vivo* human tissue optical properties and absolute chromophore concentrations using spatially resolved steady-state diffuse reflectance spectroscopy," *Phys. Med. Biol.* **44**, 967-981 (1999).
19. W. Verkrusse *et al.*, "Modelling of light distributions of homogenous versus discrete absorbers in light irradiated turbid media," *Phys. Med. Biol.* **42**, 51-65 (1997).
20. F. P. Bolin *et al.*, *Refractive index of some mammalian tissues using a fiber optic cladding method*, *Appl. Opt.*, **28**, 2297-2303 (1989)
21. A. H. Bennett *et al.*, *Phase microscopy*, Wiley, New York (1951).
22. E. Hecht, *Optics*, Addison-Wesley Publishing Company, Reading, Massachusetts (1987).
23. R. Graaff, *et al.*, "Optical properties of human dermis *in vitro* and *in vivo*," *Applied Optics* **32** (4), 435-447 (1993).
24. R. Graaff *et al.*, "Reduced light-scattering properties for mixtures of spherical particles: a simple approximation derived from Mie calculations," *Applied Optics* **31** (10), 1370-1376 (1992).
25. W.-F. Cheong, "Summary of optical properties," in *Optical-Thermal Response of Laser-Irradiated Tissue*, A. J. Welch, M. J. C. van Gemert Eds., 275-303, Plenum Press, New York (1995).
26. H. C. van de Hulst, *Multiple light scattering: tables, formulas and applications*, Academic Press, New York (1980).
27. G. Mie, Beiträge zur Optik trüber Medien speziell kolloidale Metallösungen, *Ann. Phys.*, **25**, 377- 45 (1908).

28. Lord Rayleigh, On the light from the sky, its polarization and colour, *Philos. Mag.*, **41**, 107-120 (1871).
29. C. Lenter, Eds., Geigy Scientific tables, Ciba-Geigy, Basle (1984).
30. J. Beuthan *et al.*, "The spatial variation of the refractive index in biological cells," *Phys. Med. Biol.* **41**, 369-382 (1996).
31. A. Brunsting and P. F. Mullaney, "Differential light scattering from spherical mammalian cells," *Biophys. J.* **14**, 439-453 (1974).
32. J. R. Mourant *et al.*, "Predictions and measurements of scattering and absorption over broad wavelength ranges in tissue phantoms," *Applied Optics* **36** (4), 949-957 (1997).
33. S. Fujime *et al.*, "Dynamic light scattering from polydisperse suspensions of large spheres," *Biophys. J.* **54**, 1179-1184 (1988).
34. I. S. Saidi *et al.*, "Mie and Rayleigh modeling of visible light scattering in neonatal skin," *Applied Optics* **34** (31), 7410-7418 (1995).
35. B. Beauvoit *et al.*, "Correlation between the light scattering and the mitochondrial content of normal tissues and transplantable rodent tumors," **226**, 167-174 (1995).
36. G. G. Stokes, "On the Change of Refrangibility of Light," *Phil. Trans. R. Soc.* **107**, 463-562 (1852).
37. H. Stübel, "Die Fluoreszenz tierischer Gewebe in ultraviolettem Licht," *Pflügers Archiv für die gesamte Physiologie des Menschen und der Tiere* **142**, 1-14 (1911).
38. A. Policard, "Etude sur les aspects affects par des tumeurs expérimentales examinées à la lumière de Wood," *Compt. Rend. Seances Soc. Biol. Fil.* **91**, 1423- 1424 (1924).
39. J. E. Aubin, "Autofluorescence of viable cultured mammalian cells," *J. Histochem. Cytochem.* **27**, 36-43 (1979).
40. R. C. Benson *et al.*, "Cellular autofluorescence - is it due to flavins?," *J. Histochem. Cytochem.* **27**, 44-48 (1979).
41. D. H. Blankenhorn and H. Braunstein, "Carotenoids in man III. The microscopic pattern of fluorescence in atheromas and its relation to their growth," *J. Clin. Invest.* **37**, 160-165 (1958).
42. B. Chance *et al.*, "Intracellular oxidation-reduction states *in vivo*," *Science* **147**, 499-508 (1962).
43. W. Lohmann and F. Hugo, "The effect of NADH on different human and mouse cell lines," *Naturwissenschaften* **76**, 72-74 (1989).
44. M. R. Hubmann *et al.*, "Ultraviolet fluorescence of human sera: I. Sources of characteristic differences in the ultraviolet fluorescence spectra of sera from normal and cancer-bearing humans," *Clin. Chem.* **36**, 1880-1883 (1990).
45. L. Laifer *et al.*, "Biochemical basis for the difference between normal and atherosclerotic arterial fluorescence," *Circulation* **80**, 1893-1901 (1988).
46. R. P. Rava *et al.*, "Early detection of dysplasia in colon and bladder using laser induced fluorescence," *Proceedings of SPIE* **1426**, 68-78 (1991).
47. W. Lohmann *et al.*, "Native fluorescence of the cervix uteri as a marker for dysplasia and invasive carcinoma," *Eur. J. Obstet. Gynecol. Biol.* **31**, 249-253 (1989).
48. A. J. W. G. Visser *et al.*, "Spectroscopic and dynamic characterization of FMN in reversed micelles entrapped water pools," *Photochem. Photobiol.* **39**, 11-16 (1984).
49. S. Andersson-Engels and B. C. Wilson, "In vivo fluorescence in clinical oncology: fundamental and practical issues," **3**, 48-61 (1992).
50. S. Andersson-Engels *et al.*, "Investigation of Possible Fluorophores in Human Atherosclerotic Plaque," *Lasers Life Sci.* **5** (1-2), 1-11 (1992).
51. I. J. Bigio and J. R. Mourant, "Ultraviolet and visible spectroscopies for tissue diagnostics: fluorescence spectroscopy and elastic-scattering spectroscopy," *Phys. Med. Biol.* **42**, 803-814 (1997).
52. S. Andersson-Engels *et al.*, "In vivo fluorescence imaging for tissue diagnostics," *Phys. Med. Biol.* **42**, 815-824 (1997).
53. S. Andersson-Engels *et al.*, "Tumour marking properties of different haematoporphyrins and tetrasulfonated phthalocyanine - a comparison," *Lasers in Medical Science* **4**, 115-123 (1989).
54. S. Andersson-Engels *et al.*, "Laser-induced fluorescence in malignant and normal tissue of rats injected with benzoporphyrin derivative," *Photochem. Photobiol.* **57**, 978-983 (1993).
55. S. Andersson-Engels *et al.*, "Identification of brain tumours in rats using laser-induced fluorescence and haematoporphyrin derivative," *Lasers in Medical Science* **4**, 241-249 (1989).
56. S. Andersson-Engels *et al.*, "Clinical recording of laser-induced fluorescence spectra for evaluation of tumour demarcation feasibility in selected clinical specialities," *Lasers in Medical Science* **6**, 415-424 (1991).

57. J. Ankerst *et al.*, "Laser-induced fluorescence studies of hematoporphyrin derivative (HpD) in normal and tumour tissue of rat," *Appl. Spectrosc.* **38**, 890-896 (1984).
58. L. Baert *et al.*, "Clinical fluorescence diagnosis of human bladder carcinoma following low dose Photofrin injection," *Urology* **41**, 322-330 (1992).
59. J. Johansson, "Fluorescence Spectroscopy for Medical and Environmental Diagnostics," *PhD thesis*, Department of Physics, Lund Institute of Technology, Lund (1993)
60. P. W. Atkins, *Physical Chemistry*, Oxford University Press, Oxford (1998).
61. D. Voet and J. G. Voet, *Biochemistry*, John Wiley & Sons, New York (1990).
62. A. Crofts, <http://www.life.uiuc.edu/crofts/bioph354/fluores.html>, "Fluorescence in photosynthesis" (1996).
63. A. J. Welch *et al.*, "Propagation of fluorescent light," *Lasers Surg. Med.* **21**, 166-178 (1997).
64. J. Hung *et al.*, "Autofluorescence of normal and malignant bronchial tissue," *Lasers Surg. Med.* **11**, 99-105 (1991).
65. Wagnieres GA *et al.*, In vivo fluorescence spectroscopy and imaging for oncological applications. *Photochem Photobiol* **68**, 603-632 (1998)
66. Bornhop DJ *et al.*, Advance in contrast agents, reporters, and detection. *J Biomed Opt* **6**:106-110 (2001)
67. Anidjar M *et al.*, The role of laser-induced autofluorescence spectroscopy in bladder tumor detection: dependence on the excitation wavelength. *Ann NY Acad Sci* **838**, 130-141 (1998)
68. Messmann H *et al.*, Endoscopic fluorescence detection of dysplasia in patients with Barrett's esophagus, ulcerative colitis, or adenomatous polyps after 5- aminolevulinic acid-induced protoporphyrin IX sensitization. *Gastrointest Endosc* **49**, 97- 101 (1999)
69. I Georgakoudi *et al.*, Intrinsic fluorescence spectroscopy of biological tissue in *Fluorescence in Biomedicine* (Marcel Dekker, New York, 2002).
70. B Chance Optical method. *Annu Rev Biophys Biophys Chem* **20**, 1-28 (1991)
71. R Weissleder A clearer vision for in vivo imaging. *Nat Biotechnol* **19**, 316-317 (2001)
72. V Ntziachristos and B Chance Probing physiology and molecular function using optical imaging: applications to breast cancer. *Breast Cancer Res* **3**, 41-46 (2001)
73. J Korlach *et al.*, Characterization of lipid bilayer phases by confocal microscopy and fluorescence correlation spectroscopy. *Proc Natl Acad Sci* **96**, 8461-8466 (1999)
74. M Rajadhyaksha *et al.*, In vivo confocal scanning laser microscopy of human skin: melanin provides strong contrast. *J Invest Dermatol* **104**, 946-952 (1995)
75. S Gonzalez *et al.*, Characterization of psoriasis in vivo by reflectance confocal microscopy. *J Med* **30**:337-536 (1999)
76. K Konig Multiphoton microscopy in life sciences. *J Microsc* **200**, 83-104 (2000)
77. C Buehler *et al.*, Innovations in two-photon deep tissue microscopy. *IEEE Eng Med Biol Mag* **18**, 23-30 (1999)
78. PT So *et al.*, Two-photon excitation fluorescence microscopy. *Annu Rev Biomed Eng* **2**, 399-429 (2000)
79. BR Masters, *et al.*, Multiphoton excitation fluorescence microscopy and spectroscopy of in vivo human skin. *Biophys J* **72**, 2405-2412 (1997)
80. M Dellian *et al.*, Vascular permeability in a human tumour xenograft: molecular charge dependence. *Br J Cancer* **82**, 1513-1518 (2000)
81. WL Monsky *et al.*, Augmentation of transvascular transport of macromolecules and nanoparticles in tumors using vascular endothelial growth factor. *Cancer Res* **59**, 4129-4135 (1999)
82. D Toomre and DJ Manstein Lighting up the cell surface with evanescent wave microscopy. *Trends Cell Biol* **11**, 298-303 (2001)
83. U Mahmood *et al.*, Near infrared optical imaging system to detect tumor protease activity. *Radiology* **213**, 866-870 (1999)
84. A Becker *et al.*, Receptor-targeted optical imaging of tumors with near-infrared fluorescent ligands. *Nat Biotechnol* **19**, 327-331 (2001)
85. M Yang *et al.*, Whole-body optical imaging of green fluorescent protein-expressing tumors and metastases. *Proc Natl Acad Sci USA* **97**, 1206-1211 (2000)
86. A Zaheer *et al.*, In vivo near-infrared fluorescence imaging of osteoblastic activity. *Nat Biotechnol* **19**, 1148-1154 (2001)
87. JS Reynolds *et al.*, Imaging of spontaneous canine mammary tumors using fluorescent contrast agents. *Photochem Photobiol* **70**, 87-94 (1999)
88. V Ntziachristos *et al.*, Concurrent MRI and diffuse optical tomography of breast after indocyanine green enhancement. *Proc Natl Acad Sci USA* **97**, 2767-2772 (2000)

89. V Ntziachristos *et al.*, Fluorescence-mediated tomography resolves protease activity in vivo. *Nat Med* **8**, 757–760 (2002)
90. B Chance *et al.*, Highly sensitive object location in tissue models with linear in-phase and anti-phase multi-element optical arrays in one and two dimensions. *Proc Natl Acad Sci USA* **90**, 3423–3427 (1993)
91. CH Contag *et al.*, Use of reporter genes for optical measurements of neoplastic disease in vivo. *Neoplasia* **2**, 41–52 (2000)
92. N Ramanujam *et al.*, Fast and noninvasive fluorescence imaging of biological tissues in vivo using a flying-spot scanner. *IEEE Trans Biomed Eng* **48**, 1034–1041 (2001)
93. R Weissleder, Mahmood U Molecular imaging. *Radiology* **219**, 316–333 (2001)
94. R Weissleder Molecular imaging: exploring the next frontier. *Radiology* **212**, 609–614 (1999)
95. B Beauvoit and B Chance Timeresolved spectroscopy of mitochondria, cells and tissues under normal and pathological conditions. *Mol Cell Biochem* **184**, 445–455 (1998)
96. B Beauvoit *et al.*, Contribution of the mitochondrial compartment to the optical properties of the rat liver: a theoretical and practical approach. *Biophys J* **67**, 2501–2510 (1994)
97. N Bundred *et al.*, Preliminary results using computerized telediaphanography for investigating breast disease. *Br J Hosp Med* **37**, 70–71 (1987)
98. RJ Bartrum Jr, Crow HC Transillumination lightscanning to diagnose breast cancer: a feasibility study. *Am J Roentgenol* **142**, 409–414 (1984)
99. H Wallberg *et al.*, Diaphanography in breast carcinoma. Correlation with clinical examination, mammography, cytology and histology. *Acta Radiol Diagn* **26**, 33–44 (1985)
100. A Alveryd *et al.*, Lightscanning versus mammography for the detection of breast cancer in screening and clinical practice. A Swedish multicenter study. *Cancer* **65**, 1671–1677 (1990)
101. B Drexler *et al.*, Diaphanography in the diagnosis of breast cancer. *Radiology* **157**, 41–44 (1985)
102. B Monsees *et al.*, Light scanning of nonpalpable breast lesions: reevaluation. *Radiology* **167**, 352 (1988)
103. V Ntziachristos and B Chance Probing physiology and molecular function using optical imaging: applications to breast cancer. *Breast Cancer Res* **3**, 41–46 (2001).
104. C Bremer *et al.*, Optical-based molecular imaging: contrast agents and potential medical applications *Eur Radiol* **13**, 231–243 (2003).
105. H Schad *et al.*, Studies on the suitability of a cyanine dye (Viher-Test) for indicator dilution technique and its application to the measurement of pulmonary artery and aortic flow. *Pflugers Arch* **370**, 139–144 (1977)
106. CM Leevy *et al.*, Indocyanine green clearance as a test for hepatic function. Evaluation by dichromatic ear densitometry. *J Am Med Assoc* **200**, 236–240 (1967)
107. RW Flower and BF Hochheimer Indocyanine green dye fluorescence and infrared absorption choroidal angiography performed simultaneously with fluorescein angiography. *Johns Hopkins Med J* **138**, 33–42 (1976)
108. K Licha *et al.*, Hydrophilic cyanine dyes as contrast agents for near-infrared tumor imaging: synthesis, photophysical properties and spectroscopic in vivo characterization. *Photochem Photobiol* **72**, 392–398 (2000)
109. M Gurfinkel *et al.*, Pharmacokinetics of ICG and HPPH-car for the detection of normal and tumor tissue using fluorescence, near-infrared reflectance imaging: a case study. *Photochem Photobiol* **72**, 94–102 (2000)
110. JS Reynolds *et al.*, Imaging of spontaneous canine mammary tumors using fluorescent contrast agents. *Photochem Photobiol* **70**, 87–94 (1999)
111. D. A. Cortese *et al.*, "Clinical application of a new endoscopic technique for detection of *in situ* bronchial carcinoma," *Mayo Clin. Proc.* **54**, 635–642 (1979).
112. D. R. Doiron, A. E. Profio, R. G. Vincent and T. J. Dougherty, "Fluorescence bronchoscopy for detection of lung cancer," *Chest* **76**, 27–32 (1979).
113. N. Razum *et al.*, "Skin photosensitivity: duration and intensity following intravenous HpD and DHE," *Photochem. Photobiol.* **46**, 925–928 (1987).
114. J. D. Spikes, "Phthalocyanines as photosensitizers in biological systems and for the photodynamic therapy of tumors," *Photochem. Photobiol.* **43**, 691–699 (1986).
115. J. S. Nelson *et al.*, "In vivo studies on the utilization of mono-L-aspartyl chlorin (NPe6) for photodynamic therapy," *Cancer Res.* **47**, 4681–4685 (1987).
116. W. Alian *et al.*, "Laser-induced fluorescence studies of meso-tetra(hydroxyphenyl)chlorin in malignant and normal tissue in rats," *Br. J. Cancer* **70**, 880–885 (1994).

- 117.K. Svanberg *et al.*, "Photodynamic therapy of nonmelanoma malignant tumours of the skin using topical delta-amino levulinic acid sensitization and laser irradiation," *British Journal of Dermatology* **130** (6), 743-751 (1994).
- 118.E. Reddi *et al.*, "Carotenoporphyrins as selective photodiagnostic agents for tumours," *Br. J. Cancer* **69**, 40-45 (1994).
- 119.T. Takemura *et al.*, "Tumor-localizing fluorescent diagnostic agents without phototoxicity," *Photochem. Photobiol.* **59** (3), 366-370(1994).
- 120.J. F. Evensen *et al.*, "Tissue distribution of 3Hhematoporphyrin derivative and its main components, 67Ga and 131I-albumin in mice bearing Lewis lung carcinoma," in *Porphyrin Localization and Treatment of Tumors*, D. R. Doiron, C. J. Gomer, Eds., 541-562, Alan R. Liss, N.Y. (1984).
- 121.G. Jori *et al.*, "Evidence for a major role of plasma lipoproteins as hematoporphyrin carriers *in vivo*," *Cancer Lett.* **24**, 291-297 (1984).
- 122.D. A. Musser *et al.*, "The interaction of tumor localizing porphyrins with collagen and elastin," *Res. Commun. Chem. Pathol. Pharmacol.* **36**, 251-259 (1982).
- 123.D. A. Musser *et al.*, "The binding of tumor localizing porphyrins to a fibrin matrix and their effects following photoirradiation," *Res. Commun. Chem. Pathol. Pharmacol.* **28**, 505-526 (1980).
- 124.J. F. Evensen *et al.*, "Tumor-localizing and photosensitizing properties of the main components of hematoporphyrin derivative," *Cancer Res.* **44**, 482-486 (1984).
- 125.D. Kessel, "Components of hematoporphyrin derivatives and their tumor localizing capacity," *Cancer Res.* **42**, 1703-1706 (1982).
- 126.J. Moan and T. Christensen, "Cellular uptake and photodynamic effect of hematoporphyrin," *Photobiochem. Photobiophys.* **2**, 291-299 (1981).
- 127.D. Kessel, "Porphyrin-lipoprotein association as a factor in porphyrin localization," *Cancer Lett.* **33**, 183-188 (1986).
- 128.J. Darnell *et al.*, *Molecular Cell Biology*, Scientific American Books, New York (1990).
- 129.M. Korbelik, J. Hung, S. Lam and B. Palcic, "The effects of low density lipoproteins on uptake of Photofrin II," *Photochem. Photobiol.* **51** (2), 191-196 (1990).
- 130.C. Chang and T. J. Dougherty, "Photoradiation therapy: kinetics and thermodynamics of porphyrin uptake and loss in normal and malignant cells in culture," *Radiat. Res.* **74**, 498-506 (1978).
- 131.D Neri *et al.*, Targeting by affinity matured recombinant antibody fragments of an angiogenesis associated fibronectin isoform. *Nat Biotechnol* **15**:1271-1275 (1997)
- 132.JA Reddy, Low PS Folate-mediated targeting of therapeutic and imaging agents to cancers. *Crit Rev Ther Drug Carrier Syst* **15**, 587-627 (1998)
- 133.A Becker *et al.*, Receptor-targeted optical imaging of tumors with near-infrared fluorescent ligands. *Nat Biotechnol* **19**, 327-331 (2001)
- 134.K Licha *et al.*, Synthesis, characterization, and biological properties of cyanine-labeled somatostatin analogues as receptor targeted fluorescent probes. *Bioconjug Chem* **12**, 44-50 (2001)
- 135.S Achilefu *et al.*, Novel receptor-targeted fluorescent contrast agents for *in vivo* tumor imaging [in process citation]. *Invest Radiol* **35**, 479-485 (2000)
- 136.JE Bugaj *et al.*, Novel fluorescent contrast agents for optical imaging of *in vivo* tumors based on a receptor-targeted dye-peptide conjugate platform. *J Biomed Opt* **6**, 122-133 (2001)
- 137.A Zaheer *et al.*, *In vivo* near-infrared fluorescence imaging of osteoblastic activity. *Nat Biotechnol* **19**, 1148-1154(2001)
- 138.J. V. Frangioni *In vivo* near-infrared fluorescence imaging. *Curr. Opin. Chem. Biol.* **7**, 626-634 (2003).
- 139.A. M Smith, *et al.*, Quantum-dot nanocrystals for *in-vivo* molecular and cellular imaging. *Photochem. Photobiol.* **80**, 377-385 (2004).
- 140.W. C. Chan and S Nie. Quantum dot bioconjugates for ultrasensitive nonisotopic detection. *Science* **281**, 2016-2018 (1998).
- 141.X Michalet *et al.* Quantum dots for live cells, *in vivo* imaging, and diagnostics. *Science* **307**, 538-544 (2005).
- 142.R Duncan The dawning era of polymer therapeutics. *Nat. Rev. Drug Discov.* **2**, 347-360 (2003).
- 143.R.K Jain Transport of molecules, particles, and cells in solid tumors. *Ann. Rev. Biomed. Eng.* **1**, 241-263 (1999).
- 144.R.K. Jain Delivery of molecular medicine to solid tumors: lessons from *in vivo* imaging of gene expression and function. *J. Control. Release* **74**, 7-25 (2001).
- 145.S.S Chang *et al.*, Metastatic renal cell carcinoma neovasculature expresses prostate-specific membrane antigen. *Urology* **57**, 801-805 (2001).

146. N Schulke *et al.* The homodimer of prostate-specific membrane antigen is a functional target for cancer therapy. *Proc. Natl. Acad. Sci. USA* **100**, 12590–12595 (2003).
147. X. Gao, *et al.*, *In vivo* cancer targeting and imaging with semiconductor quantum dots *Nat Biotechnol* **22**(8) (2004).
148. R Weissleder *et al.*, *In vivo* imaging of tumors with protease-activated nearinfrared fluorescent probes. *Nat Biotechnol* **17**, 375–378 (1999)
149. DR Edwards and G Murphy Cancer. Proteases: invasion and more. *Nature* **394**, 527–528 (1998)
150. CH Tung *et al.*, *In vivo* imaging of proteolytic enzyme activity using a novel molecular reporter. *Cancer Res* **60**, 4953–4958 (2000)
151. CH Tung *et al.*, Preparation of a cathepsin D sensitive near-infrared fluorescence probe for imaging. *Bioconjug Chem* **10**, 892–896(1999)
152. CH Tung *et al.*, A novel nearinfrared fluorescence sensor for detection of thrombin activation in blood. *Chembiochem* **3**, 207–211 (2002)
153. C Bremer *et al.*, Optical imaging of matrix metalloproteinase-2 activity in tumors: feasibility study in a mouse model. *Radiology* **221**, 523–529 (2001)
154. C Bremer *et al.*, *In vivo* molecular target assessment of matrix metalloproteinase inhibition. *Nat Med* **7**, 743–748 (2001)
155. K Moin *et al.*, Observing proteases in living cells. *Adv. Exp. Med. Biol.*, **477**, 391–401 (2000).
156. Reinheckel *et al.*, Towards specific functions of lysosomal cysteine peptidases: phenotypes of mice deficient for cathepsin B or cathepsin L. *Biol. Chem.* **382**, 735–741 (2001).
157. S. M Redwood *et al.*, Abrogation of the invasion of human bladder tumor cells by using protease inhibitor(s). *Cancer (Phila.)*, **69**, 1212–1219 (1992).
158. R Navab *et al.*, Inhibition of carcinoma cell invasion and liver metastases formation by the cysteine proteinase inhibitor E-64. *Clin. Exp. Metastasis*, **15**, 121–129 (1997).
159. S Coulibaly *et al.*, Modulation of invasive properties of murine squamous carcinoma cells by heterologous expression of cathepsin B and cystatin C. *Int. J. Cancer*, **83**, 526–531 (1999).
160. T. M Maguire *et al.*, High levels of cathepsin B predict poor outcome in patients with breast cancer. *Int. J. Biol. Markers*, **13**, 139–144 (1998).
161. Benitez-Bribiesca *et al.*, Proteinase activity in invasive cancer of the breast. Correlation with tumor progression. *Arch. Med. Res.*, **26**, S163–S168 (1995).
162. A. R Poole *et al.*, A. Differences in secretion of the proteinase cathepsin B at the edges of human breast carcinomas and fibroadenomas. *Nature (Lond.)*, **273**, 545–547 (1978).
163. C Bremer *et al.*, Imaging of differential protease expression in breast cancers for detection of aggressive tumor phenotypes. *Radiology*, **222**, 814–818 (2002).
164. E Campo *et al.*, Cathepsin B expression in colorectal carcinomas correlates with tumor progression and shortened patient survival. *Am. J. Pathol.*, **145**, 301–309 (1994).
165. W Ebert *et al.*, Prognostic value of increased lung tumor tissue cathepsin B. *Anticancer Res.*, **14**, 895–899 (1994).
166. N Sukoh *et al.*, Immunohistochemical study of cathepsin B. Prognostic significance in human lung cancer. *Cancer (Phila.)*, **74**, 46–51 (1994).
167. J. A Foekens *et al.*, Prognostic significance of cathepsins B and L in primary human breast cancer. *J. Clin. Oncol.*, **16**, 1013–1021 (1998).
168. R Weissleder *et al.*, *In vivo* imaging of tumors with protease-activated near-infrared fluorescent probes. *Nat. Biotechnol.*, **17**, 375–378 (1999).
169. U Mahmood *et al.*, Near-infrared optical imaging of protease activity for tumor detection, *Radiology*, **213**, 866–870 (1999).
170. C Bremer *et al.*, *In vivo* molecular target assessment of matrix metalloproteinase inhibition. *Nat. Med.*, **7**, 743–748 (2001).
171. J. Chen *et al.*, *In vivo* imaging of proteolytic activity in atherosclerosis. *Circulation*, **105**, 2766–2771 (2002).
172. H Ji *et al.*, Arthritis critically dependent on innate immune system players. *Immunity*, **16**, 157–168 (2002).
173. C Escot *et al.*, Cellular localization by *in situ* hybridisation of cathepsin D, stromelysin 3, and urokinase plasminogen activator RNAs in breast cancer. *Breast Cancer Res. Treat.*, **38**, 217–226 (1996).
174. P Roger *et al.*, Cathepsin D immunostaining in paraffin- embedded breast cancer cells and macrophages: correlation with cytosolic assay. *Hum. Pathol.*, **25**, 863–871 (1994).

175. M Garcia *et al.*, Overexpression of transfected cathepsin D in transformed cells increases their malignant phenotype and metastatic potency. *Oncogene*, **5**, 1809–1814 (1990).
176. A. F Chambers and L. M Matrisian Changing views of the role of matrix metalloproteinases in metastasis. *J. Natl. Cancer Inst. (Bethesda)*, **89**, 1260–1270 (1997).
177. M. E Stearns and M Wang Type IV collagenase (Mr 72,000) expression in human prostate: benign and malignant tissue. *Cancer Res.*, **53**, 878–883 (1993).
178. M. A Moses *et al.*, Increased incidence of matrix metalloproteinases in urine of cancer patients. *Cancer Res.*, **58**, 1395–1399, (1998).
179. M Sakakibara *et al.*, Membrane-type matrix metalloproteinase-1 expression and activation of gelatinase A as prognostic markers in advanced pediatric neuroblastoma. *Cancer (Phila.)*, **85**, 231–239 (1999).
180. Kanayama *et al.*, Prognostic values of matrix metalloproteinase-2 and tissue inhibitor of metalloproteinase-2 expression in bladder cancer. *Cancer (Phila.)*, **82**, 1359–1366 (1998).
181. B Davidson *et al.*, MMP-2 and TIMP-2 expression correlates with poor prognosis in cervical carcinoma: a clinicopathologic study using immunohistochemistry and mRNA *in situ* hybridization. *Gynecol. Oncol.*, **73**, 372–382 (1999).
182. G Murphy *et al.*, Evaluation of some newer matrix metalloproteinases. *Ann. N. Y. Acad. Sci.*, **878**, 25–39 (1999).
183. D. R Shalinsky *et al.*, Marked antiangiogenic and antitumor efficacy of AG3340 in chemoresistant human non-small cell lung cancer tumors: single agent and combination chemotherapy studies. *Clin. Cancer Res.*, **5**, 1905–1917 (1999).
184. D. R Shalinsky *et al.*, Broad antitumor and antiangiogenic activities of AG3340, a potent and selective MMP inhibitor undergoing advanced oncology clinical trials. *Ann. N. Y. Acad. Sci.*, **878**, 236–270 (1999).
185. H. K Rooprai and D McCormick Proteases and their inhibitors in human brain tumours: a review. *Anticancer Res.*, **17**, 4151–4162 (1997).
186. Whitaker, M. Fluorescent tags of protein function in living cells. *Bioessays* **22**, 180–187 (2000).
187. D.C Prasher *et al.*, Primary structure of the *Aequorea victoria* green-fluorescent protein. *Gene* **111**, 229–233 (1992).
188. T.J Sweeney *et al.*, Visualizing the kinetics of tumor-cell clearance in living animals. *Proc Natl Acad Sci* **96**, 12044–12049 (1999)
189. M.V Matz *et al.* Fluorescent proteins from nonbioluminescent *Anthozoa* species. *Nat. Biotechnol.* **17**, 969–973 (1999).
190. N.G Gurskaya *et al.* GFP-like chromoproteins as a source of far-red fluorescent proteins. *FEBS Lett.* **507**, 16–20 (2001).
191. Y.A Labas *et al.* Diversity and evolution of the green fluorescent protein family. *Proc. Natl. Acad. Sci. USA* **99**, 4256–4261 (2002).
192. R.M Hoffman Visualization of GFP-expressing tumors and metastasis *in vivo*. *Biotechniques* **30**, 1016–1022, 1024–1026 (2001).
193. M Yang *et al.* Whole-body optical imaging of green fluorescent protein-expressing tumors and metastases. *Proc. Natl. Acad. Sci. USA* **97**, 1206–1211 (2000).
194. A Moore *et al.*, A model system to quantitate tumor burden in locoregional lymph nodes during cancer spread. *Invasion Metastasis* **18**, 192–197 (1998).
195. P Wunderbaldinger *et al.*, Detection of lymph node metastases by contrast-enhanced MRI in an experimental model. *Magn. Reson. Med.* **47**, 292–297 (2002).
196. M Yang *et al.*, Visualizing gene expression by whole-body fluorescence imaging. *Proc. Natl. Acad. Sci. USA* **97**, 12278–12282 (2000).
197. D Fukumura *et al.* Tumor induction of VEGF promoter activity in stromal cells. *Cell* **94**, 715–725 (1998).
198. A Moore *et al.*, Novel gliosarcoma cell line expressing green fluorescent protein: a model for quantitative assessment of angiogenesis. *Microvasc. Res.* **56**, 145–153 (1998).
199. C.H Contag *et al.*, Use of reporter genes for optical measurements of neoplastic disease *in vivo*. *Neoplasia* **2**, 41–52 (2000).
200. C.H Contag, *et al.* Visualizing gene expression in living mammals using a bioluminescent reporter. *Photochem. Photobiol.* **66**, 523–531 (1997).
201. C.H Contag and D.K Stevenson *In vivo* patterns of heme oxygenase-1 transcription. *J. Perinatol.* **21** (Suppl. 1), S119–124; discussion S125–127 (2001).

202. P Contag *et al.*, Bioluminescent indicators in living mammals. *Nat. Med.* **4**, 245–247 (1998).
203. S Bhaumik and S.S Gambhir Optical imaging of *Renilla* luciferase reporter gene expression in living mice. *Proc. Natl. Acad. Sci. USA* **99**, 377–382 (2002).
204. A Wetterwald *et al.* Optical imaging of cancer metastasis to bone marrow: a mouse model of minimal residual disease. *Am. J. Pathol.* **160**, 1143–1153 (2002).
205. G.L Costa *et al.* Adoptive immunotherapy of experimental autoimmune encephalomyelitis via T-cell delivery of the IL-12 p40 subunit. *J. Immunol.* **167**, 2379–2387 (2001).
206. S.M Burns *et al.* Revealing the spatiotemporal patterns of bacterial infectious diseases using bioluminescent pathogens and whole body imaging. *Contrib. Microbiol.* **9**, 71–88 (2001).
207. Y.H Weng *et al.*, HO-1 expression in type II pneumocytes after transpulmonary gene delivery. *Am. J. Physiol. Lung Cell Mol. Physiol.* **278**, L1273–1279 (2000).
208. J.C Wu *et al.*, Noninvasive optical imaging of firefly luciferase reporter gene expression in skeletal muscles of living mice. *Mol. Ther.* **4**, 297–306 (2001).
209. A Honigman *et al.* Imaging transgene expression in live animals. *Mol. Ther.* **4**, 239–249 (2001).
210. W Zhang *et al.* Rapid *in vivo* functional analysis of transgenes in mice using whole body imaging of luciferase expression. *Transgenic Res.* **10**, 423–434 (2001).
211. M Vooijs *et al.*, Noninvasive imaging of spontaneous retinoblastoma pathway-dependent tumors in mice. *Cancer Res.* **62**, 1862–1867 (2002).
212. P Ray *et al.* Noninvasive quantitative imaging of protein–protein interactions in living subjects. *Proc. Natl. Acad. Sci. USA* **99**, 3105–3110 (2002).
213. H Carlsen *et al.*, *In vivo* imaging of NF- $\kappa$ B activity. *J. Immunol.* **168**, 1441–1446 (2002).
214. X. Llopart *et al.*, “Medipix2, a 64 k readout chip with 55  $\mu$ m square elements working in single photon counting mode,” *IEEE Trans. Nucl. Sci.*, **49**(5), 2279–2283, Oct. 2002.
215. D. San Segundo Bello *et al.*, “Design of an interface board for the control and DAQ of the Medipix2 chip,” *Nucl. Instr. Meth. A*, **509**, 164–170 (2003).
216. M. Conti *et al.*, “Preliminary test of Medisoft 4: A control software for the Medipix2 readout chip,” *IEEE Trans. Nucl. Sci.*, **50**(4), 869–877 (Aug. 2003).
217. M. Chmeissani *et al.*, “First experimental tests with a CdTe photon counting pixel detector hybridized with a Medipix2 readout chip,” *IEEE Trans. Nucl. Sci.*, **51**(5), 2379–2385 (Oct. 2004).
218. E. Reddi and G. Jori, “Steady-state and time resolved spectroscopic studies of photodynamic photosensitizers: Porphyrins and Phtalocianines,” *Rev. Chem. Interm.*, **10**, 241–268 (1988).
219. A. E. Profio *et al.*, “Digital background subtraction for fluorescence imaging,” *Med. Phys.*, **13**, 717–721 (1986).
220. S. Prahl. Optical properties measurements using the inverse adding-doubling program. [Online] <http://omlc.ogi.edu/software/iad/manual/manual.html>
221. Y. Du *et al.*, “Optical properties of porcine skin dermis between 900 and 1500 nm,” *Phys. Med. Biol.*, **46**, 167–181 (2001).
222. N. Ramanujam *et al.*, “Low temperature fluorescence imaging of freeze-trapped human cervical tissues,” *J. Opt. Soc. Amer. A*, **8**, 335–343 (2001).
223. S. Gupta *et al.*, “Cellular uptake, localization and photodynamic effect of haematoporphyrin derivative in human glioma and squamous carcinoma cell lines”, *J. Photochem. Photobiol. B: Biology*, **69**, 107–120 (2003).
224. Chwilkowska *et al.*, “Uptake of Photofrin II, a photosensitizer used in photodynamic therapy, by tumor cells *in vitro*”, *Acta Biochimica Polonica*, **50** (2), 509–513 (2003).
225. J. S. Hill *et al.*, “Selective uptake of hematoporphyrin derivative into human cerebral glioma”, *Neurosurgery*, **26** (2), 248–254 (1990).
226. D. L. Prout *et al.*, “Detector concept for OPET, a combined PET and optical imaging system,” presented at the *Nuclear Science Symposium and Medical Imaging Conf.*, Portland, OR, Oct. 20–24, 2003.
227. A. A. Rosenkranz *et al.*, “Targeted intracellular delivery of photosensitizers to enhance photodynamic efficiency,” *Immunol. Cell Biol.*, **78**, 452–464 (2000).
228. M. L. Chiu *et al.*, “Effect of mitochondrial and plasma membrane potentials on accumulation of Hexakis (2-methoxyisobutylisonitrile) technetium in cultured mouse fibroblasts,” *J. Nucl. Med.*, **31**, 1646–1653 (1990).
229. S. D. Vecchio *et al.*, “Fractional retention of Tc-99m-Sestamibi as an index of P-glycoprotein expression in untreated breast cancer patients,” *J. Nuc. Med.*, **38**, 1348–1351 (1997).
230. L. Kostakoglu *et al.*, “Clinical validation of the influence of P-glycoprotein on Tc-99m-sestamibi uptake in malignant tumors,” *J Nucl. Med.*, **38**, 1003–1008 (1997).

- 231.Z. Burak *et al.*, "mTc-MIBI imaging as a predictor of therapy response in osteosarcoma compared with multidrug resistance-associated protein and p-glycoprotein expression," *J. Nucl. Med.*, **44**, 1394-1401 (2003).
- 232.I. Foldes *et al.*, "Comparative scanning of thyroid nodules with technetium- 99m pertechnetate and technetium-99m methoxyisobutylisonitrile," *Eur. J. Nucl. Med.*, **20**, 330-333 (1993).
- 233.G. Mettivier *et al.*, "Design of a compact gamma camera with semiconductor hybrid pixel detectors: imaging tests with a pinhole collimator," *Nucl. Instr. Meth. A*, **509**, 321-327 (2003).
- 234.E. Bertolucci *et al.*, "Preliminary test of an imaging probe for nuclear medicine using hybrid pixel detectors. Presented at 3rd international workshop on radiation imaging detectors," *Nucl. Instr. Meth. A*, **487**, 193-201 (2002).
- 235.J. M. Park and S. S. Gambhir, Multimodality Radionuclide, Fluorescence, and Bioluminescence Small-Animal Imaging, Proceedings of IEEE, **93** (4), 771-783 (2005).
- 236.A.A. Rosenkranz, D.A. Jans and A. Sobolev, "Targeted intracellular delivery of photosensitizers to enhance photodynamic efficiency", *Immunol. Cell Biol.*, **78**, 452-464 (2000).
- 237.W.G. Robert and M.W. Berns, "In vitro photosensitization I. Cellular uptake and subcellular localization of mono-L-aspartyl chlorin e6, chloroaluminium sulfonated phth, and phthalocyanine, and Photofrin II", *Laser Surg. Med.*, **9**, 90-101 (1989).
- 238.P.A. Scourides, R.M. Bohmer, A.H. Kaye and G. Morstyn, "Nature of the tumor-localising components of haematoporphyrin derivatives", *Cancer Res.*, **47**, 3439-45 (1987).
- 239.[http://www.andor.com/pdfs/Digital\\_Camera\\_Fundamentals.pdf](http://www.andor.com/pdfs/Digital_Camera_Fundamentals.pdf)
- 240.C. A. Spibey, P. Jackson, K. Herick, A unique charge-coupled device/xenon arc lamp based imaging system for the accurate detection and quantitation of multicolour fluorescence, *Electrophoresis*, **22**, 829-836 (2001).
- 241.K. Svanberg *et al.*, "Clinical multi-colour fluorescence imaging of malignant tumours-initial experience", *Acta Radiol.*, vol. 39, no. 1, pp. 2-9, 1998.
- 242.M. G. Lagorio *et al.*, "Photophysics on surfaces: Absorption and luminescence properties of Pheophorbide-a on cellulose", *Phys. Chem. Chem. Phys.*, vol. 3, pp. 1524-1529, 2001.
- 243.U. Mahmood, "Near Infrared Optical Applications in Molecular Imaging", *IEEE Eng. Med. Biol. Mag.*, vol. 23, no. 4, pp. 58-66, 2004.
- 244.A. T. Shaw *et al.*, Future of Early Detection of Lung Cancer: The Role of Mouse Models, *Clin Canc Res*, **11**, 4999-5003 (2005).
- 245.C. Bremer *et al.*, Imaging of Differential Protease Expression in Breast Cancers for Detection of Aggressive Tumor Phenotypes, *Radiology*, **222**, 814, 818 (2002).
- 246.O. R Mook *et al.* Visualization of early events in tumor formation of eGFP-transfected rat colon cancer cells in liver. *Hepatology* **38**, 295-304 (2003).
- 247.J. W. Sturm *et al.* Enhanced green fluorescent protein-transfection of murine colon carcinoma cells: key for early tumor detection and quantification. *Clin. Exp. Metastasis* **20**, 395-405 (2003).
- 248.O Peyruchaud *et al.* Early detection of bone metastases in a murine model using fluorescent human breast cancer cells: application to the use of the bisphosphonate zoledronic acid in the treatment of osteolytic lesions. *J. Bone Miner. Res.* **16**, 2027-2034 (2001).
- 249.T. Troy *et al.*, "Quantitative comparison of the sensitivity of detection of fluorescent and bioluminescent reporters in animal models", *Mol. Imaging*, vol. 3, pp. 9-23, 2004.
- 250.J. M. Park and S. S. Gambhir, Multimodality Radionuclide, Fluorescence, and Bioluminescence Small-Animal Imaging, Proceedings of IEEE, **93** (4), 771-783 (2005).